Effect of Atmospheric Drag Estimation on Orbit Determination

by

Madeline Nichols McDougal

A thesis submitted to the Graduate Faculty of
Auburn University
in partial fulfillment of the
requirements for the Degree of
Master of Science

Auburn, Alabama
December 9, 2023

Keywords: Orbit Determination, Ballistic Coefficient, GNSS, GPS, Estimation

Approved by

Scott Martin, Ph.D., Chair, Assistant Professor in Mechanical Engineering
David Bevly, Ph.D., Bill and Lana McNair Distinguished Professor
Davide Guzzetti, Ph.D., Assistant Professor in Aerospace Engineering

Abstract

Determining the location of Low Earth Orbit (LEO) satellites in orbit is an important aspect when using them for navigation and performing reentry analysis. A large perturbation in LEO satellite orbits is atmospheric drag due to its orbiting altitude. This variable, unlike gravity, can be difficult to model accurately due to the variations in density and the ballistic coefficient. While in orbit, a satellite equipped with an on-board GPS receiver can malfunction and no longer receive measurements. In this case, the satellite would have to use a dynamic model to propagate its position forward in time to relay to a ground user.

Out of the two deterministic terms in the drag equation, the ballistic coefficient is the larger variable and has many terms that are difficult to determine explicitly. Due to this, it would be advantageous to estimate the ballistic coefficient while in orbit in the case that the satellite loses GPS measurements. From the estimation, the satellite could use that term when calculating atmospheric drag during propagation. This would allow the positioning solution of the satellite to increase in accuracy. With a more accurate satellite position, the ground user's navigation solution would also improve.

This thesis determines the effect the atmospheric drag has on the satellite's orbit by inducing error on the ballistic coefficient. Atmospheric drag is the second-largest perturbation affecting LEO satellites. It is important to understand how LEO satellites behave in the absence of correcting measurements to know the error when using LEO satellite signals for positioning. Throughout this research it was found that while the atmospheric drag is the second-largest perturbation, the gravitational forces are magnitudes larger causing meters of error on the propagation solution. This error in the satellite's orbit translates into meter level error at the ground receiver.

Once the error on the ballistic coefficient was studied, it was decided to attempt to estimate using the GPS measurements. Estimation of the ballistic coefficient has been performed on two-line element data, but has not been performed on GPS measurements.

Through this estimation process, it was determined that noise of the GPS measurements greatly outweighed the impact of the ballistic coefficient on the overall position accuracy. With the amount of noise reduced and accurate pole placement, it was indeed found to be possible to estimate the ballistic coefficient to an accuracy of 10% of the true coefficient.

Acknowledgments

I would like to thank my professors in the GAVLAB, Dr. Martin and Dr. Bevly, for helping me develop my professional and research skills in these last two years. I would also like to thank Kip Underwood for being my mentor throughout this whole process. T This thesis would not have come to fruition without his help and support. I would also like to thank Sam McDougal, my husband, for being my physical and emotional support through undergraduate and graduate school. Thank you to the 2020 cohort for accepting me as one of you and for breaking up school with fun activities (long live The Dead Reckoners). Lastly, I would like to acknowledge my dog Chip for being a happy face every time I got home from a long day of work.

Table of Contents

List of Figures

List of Tables

Chapter 1

Introduction

1.1 Motivation

Low Earth orbit (LEO) satellites have been around since the beginning of the space race starting with the first artificial satellite, Sputnik 1. Since then, LEO satellites have only increased in number because of their use in communication, Earth observation, and signal monitoring [1]–[5]. A large benefit of LEO satellites is their proximity to Earth compared to satellites in medium Earth orbit (MEO), such as Global Navigation Satellite System (GNSS) systems, and satellites in geostationary Earth orbit [1], [6].

Other benefits of LEO satellites include decreasing the size and therefore power requirement of the satellite, decreasing launch costs by launching multiple satellites from the same space vehicle, increasing throughput, and having low latency [1]–[4], [7]. Because LEO satellites are closer to Earth, their signals are sometimes used as signals of opportunity (SOP) by augmenting GNSS signals to improve positioning performance for end users. SOPs are alternate forms of navigation that do not require the user to use GNSS signals for navigation purposes. A special case of an SOP is called a cooperative signal of opportunity. In the case of a cooperative SOP, the satellite is used to *improve* the performance of GNSS navigation solutions. LEO satellites signals are very attractive for their use as SOPS because of their stronger signals [1], diverse signal direction [6], orbital rate, and greater number of satellites to use as SOPs [4].

Recently, LEO satellites have been launched as megaconstellations which is defined as hundreds of satellites launched in a single satellite constellation allowing for better global

coverage for the primary purpose of communication and internet needs [2]. Some examples of megaconstellations and their number of satellites are: Samsung (4200+), SpaceX (4000+), Boeing (1300+), OneWeb (720+), and LeoSat (100+) [1]–[4]. The need for megaconstellations points back to LEO satellite's orbit proximity to Earth. Because LEO satellites orbit within a range of 100 to 2000 km [2], they only cover a small percentage of the Earth at any given instant [1]. To improve coverage, there needs to be more satellites in a single constellation. While improving coverage, the growth in the number of LEO satellites causes an inability to reliably predict a satellite's future states by increasing the risk of collision [2]. This, along with using LEO satellites for navigation, calls for the need to accurately predict a LEO satellite's orbit. In addition to decreasing the collision risk and unpredictability factor, there are other benefits of predicting a satellite's orbit such as aiding mission planning, improving communication, and analyzing scientific data [8].

Some LEO satellites use a on-board GNSS receiver to obtain a navigation solution. These satellites are able to determine their location from 4+ Global Positioning System (GPS) signals, the United States' GNSS system, and then transmit the navigation solution in a signal down to a ground user. On-board orbit determination can know a satellite's position to centimeter level accuracy [9], but an issue arises when the satellite's GPS receiver is unable to track at least 4 satellites. This has been observed due to effects such as solar storms in the atmosphere [9]. Once this happens, the satellite must use a dynamic model to integrate its position until GPS signal is received again. A satellite propagates its position by integrating an acceleration model to determine its position and velocity.

The major challenge to predicting a satellite's orbit is the inability to model the LEO satellite's environment accurately. Much of the uncertainty of a LEO satellite orbit comes from measurement errors, imperfectly known physical quantities, internal dissipated forces, and the unpredictable space environment [8]. Errors caused by the space environment consist mainly of perturbations (disturbances of motion). Besides the gravitational pull of the Earth, air drag is the largest perturbation effecting LEO satellite's orbits that are under 500 km [2], [5], [10]–[16].

Air drag, defined in Equation (1.1), is an encounter of a LEO satellite with the upper atmosphere of Earth that alters the satellite's orbit and attitude [8].

$$\vec{a}_D = -\frac{1}{2} B \rho |\vec{v}_{rel}|^2 \frac{\vec{v}_{rel}}{|\vec{v}_{rel}|} \tag{1.1}$$

It acts in the opposite direction of the satellite's motion. Because of this, the prediction error is applied mostly to the "in-track" direction of motion [8], [17]. This allows the satellite's orbit to be well known, but the satellite's position along the orbit to be uncertain [2], [17]. Not including the atmospheric drag in the prediction model will cause an underestimation of the satellite's position in the orbit [8]. Within the atmospheric drag, there are two terms that are not known to any accuracy, density of the atmosphere (Eq. (1.2)) and the ballistic coefficient (Eq. (1.3)).

$$\rho = \rho_0 \text{exp} \left[-\frac{h - h_0}{H} \right] \tag{1.2}$$

$$B = \frac{A c_d}{m} \tag{1.3}$$

The atmospheric models are difficult to estimate because the parameters used are difficult to measure directly [13], [18], [19]. While the velocity is four times larger than the next largest variable in the drag equation, it is highly dependent on the results from any orbit determination process such as through an EKF [18].

In some fields, the ballistic coefficient is often seen as the reciprocal of Equation (1.3). To stay congruent with former satellite literature, in this paper, it will be referred to as shown. The ballistic coefficient is comprised of stochastic terms.

- **coefficient of drag** (c_d): The non-dimensional drag coefficient is related to the shape of the satellite but is better defined as a complex interaction of the atmosphere [18]. In reality, it can only be known by experimentation in a wind tunnel environment which can lead to other errors due to lack of atmospheric replication [2]. Research

states that the drag coefficient will vary while in orbit [2]. Over time, the value will change minimally allowing for the assumption that it is a constant [18].

- **cross-sectional area normal to velocity** (A): The cross-sectional area can change due to the changing nature of the satellite's attitude. Depending on the specific shape of the satellite, the cross-sectional area can change by a factor of 10 or more [18]. Depending in the attitude relative to the direction of motion, the area will vary. For example, when a satellite is turned to point towards a ground receiver, the velocity vector will be exposed to more or less surface area [8].

- **mass** (m): Satellite mass is either a known, constant, or unknown value [18]. The mass, to an extent, is known by the operator but can fluctuate during orbit from events like fuel consumption [8]. This value is the most well known value out of the three terms that compose the ballistic coefficient.

These quantities are all physical quantities and thus are effected by how the air flows over the surface of the satellite. Therefore, the ballistic coefficient is defined as a sensitivity factor that "gauges the level of responsivity of the space object to a change in density and/or relative velocity [2]." Because of the nature of the variables that compose the ballistic coefficient, it will vary with time [18], [20]; however, for the duration of time used in this research, the ballistic coefficient is not expected to change drastically. Therefore, it is assumed the ballistic coefficient will remain constant for the duration of all studies discussed in this thesis.

The original operator of the satellite would know many of these terms, but a third party operator would have little to none of this information making the ballistic coefficient an unknown and often times assumed value. This makes modeling and determining the effect of the ballistic coefficient a vital asset in possibly improving the atmospheric drag model and thereby improving the satellite's orbit prediction.

1.2 Related Work

1.2.1 Prediction of Satellite Orbit and Ballistic Coefficient using TLE data

A two line element (TLE) can be used to make predictions about satellite's orbit. The files contain data of Keplerian orbital elements written on two lines of ASCII text formatted in 80 columns [1], [21]. These must be used with certain algorithms containing the simplified general perturbation (SGP) model, most commonly which is the SGP4 algorithm [1], [21]. A TLE is most beneficial when there is a memory constraint on the satellite. This is because the ground station propagates the LEO's TLE through the SGP model and is able to determine a satellite's location and pointing angles without any a priori knowledge [1]. While TLEs can be used to propagate an orbit using a SGP model, these simplified models are known to have initial epoch errors around three kilometers [6], [11], [22]–[24], up to ten kilometers after 24 hours of the TLE being produced [25], and 100 kilometers using a one-week-old TLE [23].

While there is a large initial error, TLEs are still a standard for describing the orbital elements of a LEO satellite. This is largely because the US government still provides regular updates of satellite TLEs [23] which can be found at [26] and [27]. TLEs can be used to estimate the ballistic coefficient using a term called "B*", seen in Equation (1.4), which is included in the TLE data.

$$B* = \frac{\rho_0 B}{2} \tag{1.4}$$

B* and the ballistic coefficient are not the same term because the B* is used as a fitting parameter when producing a TLE [28]. Although it cannot be used as a replacement for the ballistic coefficient, it can be used to derive the coefficient as done in [28].

For more work done using TLE data to obtain the ballistic coefficient, see these sources: [29]–[31]. Besides using TLEs, another option is to use an on-board GNSS receiver for determining a satellite's position in space. It has been shown in [23] that using

an on-board GPS receiver can mitigate the errors associated with TLE use and reach precision up to tens of meters. The research in this thesis will use GPS receiver data for orbit propagation and ballistic coefficient estimation.

1.2.2 On-Board LEO GNSS Receivers

LEO satellites have the advantage of being a variety of sizes depending on the mission objectives. Recently LEO satellites have been able to decrease in size because of the technological advances in size of GNSS receivers. This allows for less of a power requirement during operation, less of an expense to build, and a decrease in launch costs [1].

An example of this is that GNSS receivers are now being manufactured small enough to function on LEO satellites. One such example is the piNAV system used in [23] that was implemented on a 1U class CubeSat. From this study, it was shown that the position error magnitude between the GPS and TLE data was between 0-4 km and the radius error as a function of time varied within 500 m [23]. The availability of new low-cost GPS receivers that can be applied to small satellite missions creates a need for better on-board orbit determination [32]–[34].

The benefit of on-board GNSS receivers for real-time navigation is that it is cost-effective [35]. It reduces the need for costly ground stations for the calculation of TLEs. The success of on-board GNSS receivers is seen in the GRACE, CHAMP, SWARM, and TOPEX satellites among others [9], [35]–[38].

Through the use of an on-board GPS receiver, precise orbit determination (POD) would be able to define the exact motion of a satellite and then a Kalman filter would be used to estimate the position, allowing for centimeter level accuracy of a LEO's position [35], [39]. This completely removes the need for ground tracking stations.

1.3 Contributions

This research captures the effect that error in modeling the ballistic coefficient has on a LEO satellite's location. The satellite's error is then translated into a ground receiver's error to show the impact of modeling incorrectly. It is shown that the ballistic coefficient

error creates meter level error for the ground receiver. The largest effect for the end user is determined by the accuracy of the measurements being used.

A modeling technique to determine the ballistic coefficient was created. It was found that using this technique, the measurements being used to supply velocity must have a standard deviation less than 1e-4 meters and 1e-4 meters per second. Because of this, it is not feasible to try to capture the ballistic coefficient while in orbit. This work captures the affect that the ballistic coefficient has on a LEO satellite's and a ground users position.

1.4 Outline

Chapter 2 will cover technical background related to the procedure of the experiment as well as history on orbit determination. Chapter 3 covers a brief visibility analysis to determine the maximum amount of time the satellite will be in view of the receiver. Next, Chapter 4 will look at the acceleration model accuracy by propagating the satellite and measuring accuracy. Chapter 5 will model a loss of GPS signal on a satellite. Chapter 6 determines if the ballistic coefficient can be estimated from a GPS receiver. After, Chapter 7 will look at how the error of the ballistic coefficient effects the propagation error. Chapter 8 will then compare the ballistic coefficient error on the simulated GPS outage error. Chapter 9 showcases a GPS outage simulation where the gravity model is completely known. Finally, Chapter 10 will cover conclusions and future work.

Chapter 2

Technical Background

2.1 Introduction

A background on orbit determination and the different techniques used today is discussed. Orbit determination has been used since the space race and several techniques are still performed today. The way an orbit is determined is dependent on the orbital height of the satellite. Since the satellite simulated in this thesis is a LEO satellite, an on-board GPS receiver is studied as these are becoming more common on LEO satellite orbits.

The experimental set-up is discussed in detail as well as assumption made for the thesis. The testing for this thesis is performed by using hardware in the loop. A Novatel GPS receiver is simulated as being an on-board GPS by taking measurements from a simulated satellite. The satellite is simulated using a Spirent GSS9000.

The model using for integrate is also developed in this section. Spherical harmonics are used as the basis for the gravitational model while the atmospheric drag and the force due to the rotation of the Earth are added to the gravity to form the model. Several other forces are discussed but were not added to the equation to decrease the computation time.

2.2 Notation

Notation of this paper will be as follows. Scalar variables will be denoted by a lowercase letter such as m while vector values will be shown with a right facing arrow like $\vec{m}$. Matrices throughout this thesis will be portrayed as capital bold letters with Equation (2.1) being

a matrix made up of scalar values. A matrix or vector that is transposed will be represented by a superscript T.

$$\mathbf{M} = \begin{bmatrix} m_{11} & m_{12} \\ m_{21} & m_{22} \end{bmatrix} \tag{2.1}$$

The position will be referred to using r, the velocity v, and the acceleration a. The difference types of accelerations can be differentiated by the subscripts used such as $\vec{a}_D$ will represent atmospheric drag while $\vec{a}$ will represent total acceleration of the satellite.

2.3 Experimentation Setup

An Iridium satellite with the characteristic listed in Table 2.1 is studied in this thesis. This satellite was developed by Motorola Corporation [40] in the 1990's for use as a satellite phone communication network. As seen in Figure 2.1, it has the standard appearance of a satellite with a central body with solar panels extending outward. In this case the Iridium satellite has four solar panels total that rotate to the best capture the sunlight. The constellation consists of six planes with eleven satellites in each plane orbiting the Earth every 100 minutes which can be seen in Figure 2.2. These satellites have an altitude of approximately 780 kilometers in a polar orbit [40].

Figure 2.1: Iridium Satellite [41]

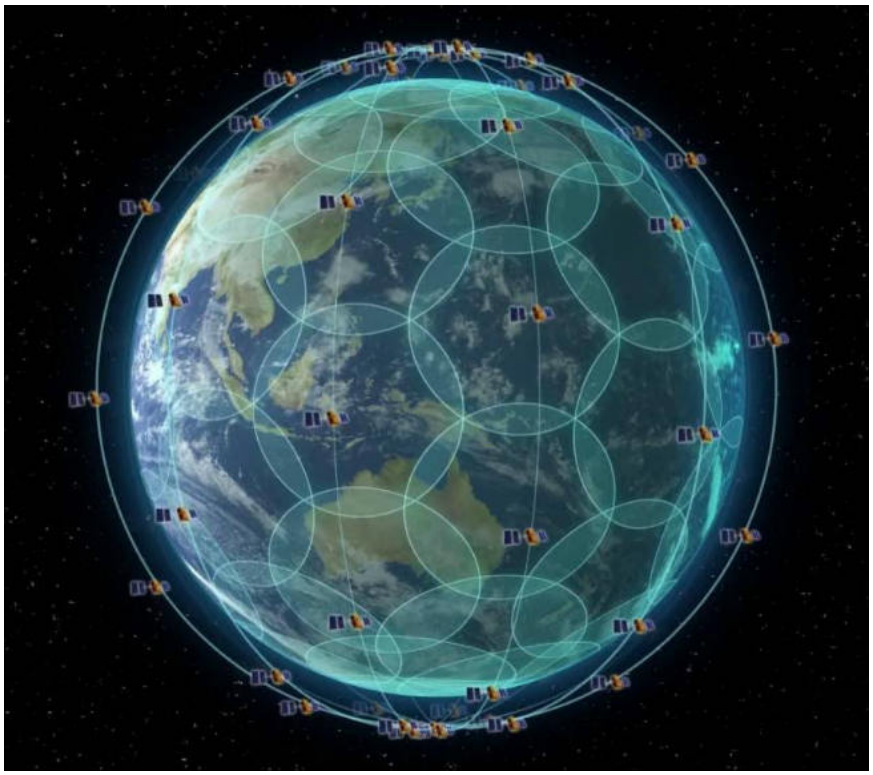

Figure 2.2: Iridium Satellite Constellation [41]

The satellite studied in this research, unlike the real Iridium satellite, will be studied using an altitude of around 400 kilometers and a near circular orbit. These changes cause a few expected consequences such as the satellite decreasing in orbit at a faster rate than at 780 kilometers and having a larger atmospheric drag force acting upon it. The simulation starts on 12 February 2023 at UTC time 00:00:00. When determining the ballistic coefficient, these values (Table 2.1) are used along with a coefficient of drag of 2.2 which is shown to be a standard used throughout satellite research [2].

	Iridium
mass [kg]	820
surface area [m^2]	18.48

Table 2.1: Satellite Characteristics

Satellite constants used throughout literature are defined in Table 2.2. These constants will be used in simulation of the Earth's gravity field, modeling the effects of the Earth's rotation, and determining the atmospheric density.

Variable	**Value**
Radius of the Earth (R_e)	6378.137 [km]
Gravitational Constant (μ)	3.9860e5 [km^3/s^2]
Rotation Rate of Earth (ω)	7.292115e-5 [rad/s]
Scale Height (H)	58.2 [km]
Reference Density (ρ_0)	0.0105 [kg/km]
Reference Height (h_0)	400 [km]

Table 2.2: Constants

A Spirent GSS9000 is used to simulate the satellite's orbit. It can simulate several types of GNSS satellite signals [35], but GPS is used for this research. The GPS measurements will be obtained using a Novatel GPS receiver. For more information about the abilities of the Spirent simulator or a more in-depth knowledge of how it works please view [37].

2.3.1 Assumptions

While analyzing the data, some assumptions were made. Firstly, it is assumed that the satellite has only gravity and air drag acting on it. It was decided to omit the effects of solar-radiation pressure (SRP) and third-body effects because these effects satellite would be negligible compared to air drag for a orbiting LEO satellite altitude. If the satellite increased in altitude above 1000 kilometers, the SRP effects would overpower the atmospheric drag effects and need to be included in the acceleration.

Secondly, the density model was set as constant value. The value was found by using an exponential density model (Eq. (1.2)) which the constants were obtained from [42] and displayed in Table 2.2. The standard deviation of the density was very small throughout

the orbit of the satellite. From this observation, it was chosen to leave the density as a constant value rather than to continuously calculate the exponential model to simplify the calculations and computation time. Which [8] states that while uncertainties in the density and ballistic coefficient are correlated, they can be estimated and considered separately because of work done by [43]. This statement allows for the freedom to separate the two variables for estimation thereby holding one constant while the other is estimated.

The third and final assumption made was that the receiver outputs positioning updates at a rate of 1 Hz which is a common value for GPS receiver sampling frequency [23]. This creates some difficulty with propagation as the time step is significantly large compared to the velocity rate of change. Because of their proximity to Earth, LEO satellites orbit at a faster period of around 1.5 hours compared to MEO and GEO satellites which could have a period between 12 and 24 hours. Because of this LEO satellites are only visible to a ground receiver from 10 to 30 minutes at a time depending on their orbiting altitude [1]. This leads to a larger change in velocity between each time step which creates uncertainties when predicting the satellites future states which causes errors to accumulate over time [2].

2.4 History of Orbit Determination

Orbit determination for many years was the process of determining the classical orbital elements (Keplerian elements) of a planet or comet [44]. The observations started as optical data, which had errors in the kilometer range. This progressed to photographic and Doppler techniques which improved the error to meter level accuracy. Next, laser ranging was introduced which bettered the observation of the Doppler techniques but only by a few meters. The last and largest improvement came with advances to the laser technology, radio tracking, and force modeling which improved the determination results to centimeter level accuracy [45]. With the introduction of the space race and satellites, this process needed to be expanded to determining the position and velocity of an orbiting object by means of a state vector or ephemeris [45]. The next three sections will discuss the differences in orbit determination tactics on satellites of different orbiting altitudes: GEO (above 36,000 km), MEO (2000 km - 36,000 km), and LEO (100 km - 2000 km).

There are many tactics for precise orbit determination (POD) : satellite laser ranging (SLR) , ground station tracking of satellite radio waves, and on-board GNSS receivers. According to [45] there are three requirements for orbit determination to work properly which include knowing the force model acting on the satellite, understanding observational data, and improving computational techniques. To determine where a satellite is located, an initial measurement is taken at some epoch which then can be used to estimate the satellite's state. To be able to support navigation, centimeter to meter level accuracy is a requirement [46]. Ways to improve the orbit determination solution are improved force model, correct GPS orbits and GPS satellite antenna offsets, and by fixing ambiguity parameters [47].

Orbit determination, as opposed to orbit propagation, processes observational data to help determine the orbit [18]. Orbit determination is the process of using observational data to predict the future states of the satellite while orbit propagation does not use measurements to update the states. Instead, this method requires numerical integration of precise equations of motion and force models to determine the satellite states at a future moment in time [45], [48]. The last way to determine an orbit is called orbit prediction which combines the two methods to predict the future states of the satellite beyond what is determined using POD.

2.4.1 The Two Methods of Orbit Determination

Two of the estimation techniques most often used for orbit determination are batched least squares and Kalman filter. Batched least squares is most often used when post-processing is required while the Kalman filter, most commonly an extended Kalman filter (EKF) , is used in real-time scenarios [6], [7], [11], [12], [37], [49], [50]. Batch least squares is the process of collecting and processing the data for a fixed period in a single step. As the batch size grows larger, the averaging of the observations reduces the amount of information that can be obtained from the solution [18]. This can cause errors to accumulate over a large batch size.

The Kalman filter uses process noise to update the state covariance matrix and produce a better estimate through a sequential update of the state vector [18], [49]. This

process is best used when the dynamic model of the satellite is not completely known. Figure 2.3 shows the process and equations of a linear Kalman filter. On the other hand, an EKF is implemented on a nonlinear system using a first order linearization of the nonlinear functions [39]. The act of using a linearized form of the equations can cause errors to accumulate in the covariance. To mitigate these errors sometimes an unscented Kalman filter (UKF) is used instead. The UKF, instead of linearizing the equations, uses a deterministic sampling approach [39], [50]. Instead of propagating the state vector through the nonlinear functions, sigma points are propagated to help capture the true covariance of the system [51]. Normally in orbit determination, there is very little need to use a UKF versus an EKF because the performance is very similar to both for small initial errors or short measurement sampling periods. Overall much of the orbit determination errors come from reference system maintenance, measurement modeling, and dynamic modeling [52].

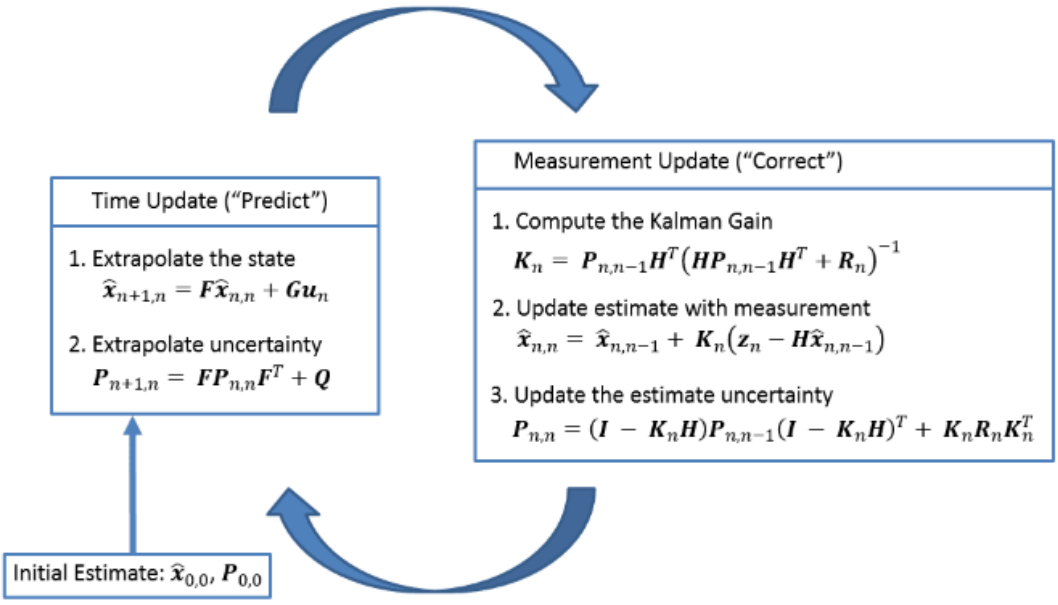

Figure 2.3: Linear Kalman Filter Algorithm [53]

2.4.2 Orbit Determination On Geostationary Orbit (GEO) Satellites

Because of a GEO satellite's orbital attitude, there is a limited amount of tactics to use in orbit determination. To determine the orbit on a GEO satellite, the most traditional method is to use ground-based ranging such as unified S-band ranging [54], [55]. Over

the years, more research has been done on the feasibility of other ranging tactics on GEO satellites which will be discussed in this section. Because of the poor performance of S-band ranging systems, a more accurate mode of POD for GEO satellites would need to be developed to use them for navigation purposes. Research in 2010 was presented by [46] on a new POD method. This method combines SLR with C-band transfer ranging for GEO satellites allowing for accuracies better than 5 meters. Unlike other satellite altitudes, GEO satellite orbits are difficult to determine to meter or centimeter level accuracy. This is due to the nature of the satellite being geostationary causing the tracking geometry determination difficulty. Another reason is that the errors may not be separated from the radial component errors [46]. Before [46], using previous methods of POD which involved united S-band ranging systems achieved only hundred meter level accuracy with a bias between three and five meters [46], [56].

Another alternate method is satellite laser ranging (SLR) which can be difficult to implement and expensive to own and operate. SLR has the potential to reach accuracies of millimeter to centimeter level accuracy [46]. This method has been tested on GPS satellites in MEO orbit, but is difficult to apply to GEO satellites. Since GEO satellites orbit at such a high altitude, it is difficult for the SLR telescopes and laser systems to reach the satellite, but it is proven that if a SLR measurement can be obtained then an accuracy of three centimeters can be achieved [46].

[54] proposes using a GNSS receiver on-board a GEO satellite could improve the determination result and also eliminate the need for ground tracking stations. Because of the orbiting altitude of GEO satellites in relation to GNSS satellites the GEO satellite is not able to acquire the entire GNSS transmit beam. The GNSS receiver antenna on-board the GEO satellite would need to point toward the Earth so that the GNSS and main lobes of the GNSS signal can be received [54], [57]. Figure 2.4 shows how the GEO satellite can only receive part of the GPS transmit beam. Several simulation studies have been done on the feasibility of a GNSS receiver on GEO satellites with results showing an orbit determination solution of better than 20 meters [58]. Simulation studies show the feasibility of the objective, but [57] implements this strategy on an orbiting satellite in GEO. Using

this procedure, the GNSS pseudorange data is collected on-board the satellite, an ephemeris is produced and then transmitted to a ground station for processing.

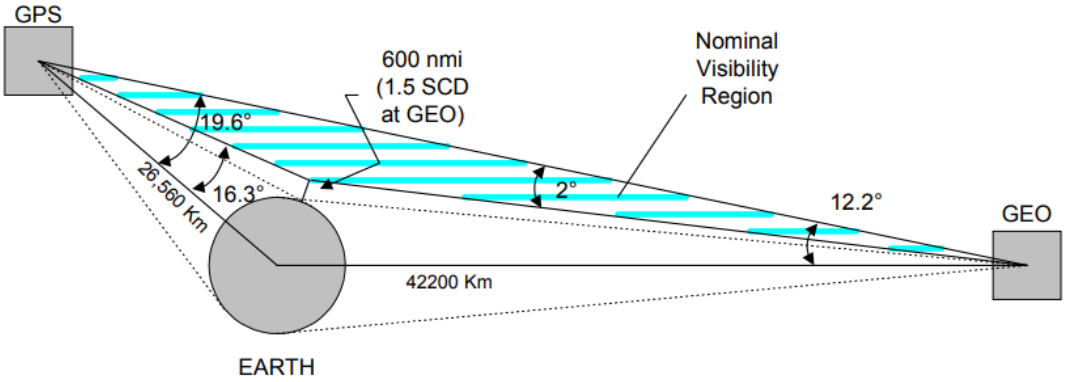

Figure 2.4: GPS Visibility from GEO Orbit [57]

2.4.3 Orbit Determination On Medium Earth Orbit (MEO) Satellites

The most common type of satellites orbiting in MEO are GNSS satellites which are primarily used for navigation. Each country has their own system with different orbital parameters. In the United States, the satellite system is called GPS, but there are several other satellite systems run by other countries. In Europe, the system is called Galileo, in China BeiDou Navigation Satellite System (BDS) , and Russia's system is called GLONASS. Each system is tailored for the best navigation over that region. GPS satellites determine their orbit through the use of ground tracking stations. The ground stations use radar, signal doppler, or laser reflectors to locate the satellite. From there, the classical orbital elements are determined and then transmitted to the satellite. Once the GPS satellite has obtained its precise location from the ground station, it transmits its position and current clock time to GPS receivers. The GPS receiver can then calculate the position of itself once it has received four GPS satellite's positions [59].

The rest of this section will focus on China's navigation system due to differences from the way that GPS determination is performed. [52] studies the orbit determination procedure for China's BDS system of satellites. This system is compiled of 3 GEO satellites, 3 Inclined GEO satellites, and 24 MEO satellites. For comparison, the GPS constellation

deployed by the United States is comprised of 24 MEO satellites on six orbital planes [52]. BeiDou, unlike GPS, relies on a regional tracking network that is limited to within China's border [60]. Because at the time of [60] the regional network was still in development, the orbit determination procedure is slightly different and a radial orbit accuracy of 3 meters can be achieved. The reason for this inaccuracy is the inability to accurately represent the clock error model due to no support of time synchronization due to the limited amount of ground tracking stations [52]. On the other hand, GPS determination of centimeter level accuracy can be obtained using international ground tracking stations such as the work done by International GNSS Services (IGS) [61].

The main reason for the accuracy difference of GPS and BDS is that BDS uses a single satellite orbit determination method while IGS uses multi-satellite orbit determination which allows for the elimination of the time synchronization issue. Figure 2.5 shows the difference before 2010 between the amount of ground tracking stations of IGS and BDS. Before 2010, China had not expanded outside of the regional tracking network and therefore had not tested a multi-tracking satellite system [52]. Since 2010, the amount of data BDS uses to determine their orbit has increased to include International GNSS Monitoring and Assessment System and the IGS Multi-GNSS Monitoring Experiment which has allowed precise BDS orbits and clock errors to be determined. While the increase in data has improved the positioning performance of BDS, it is still around 2 times worse than the GPS or Galileo systems [62].

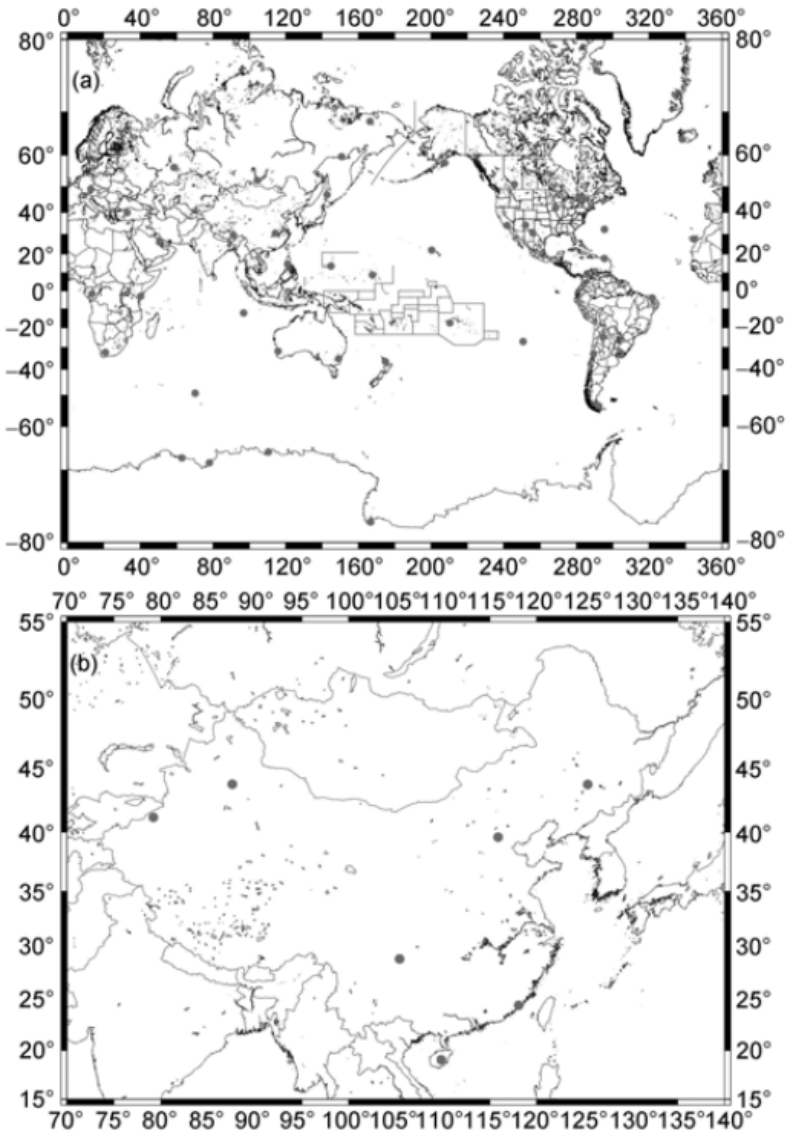

Figure 2.5: (Top) Global Network Distribution (Bottom) Regional Network Distribution [52]

Another way BDS satellites communicate is through an inter-satellite linkage. This is represented visually in Figure 2.6 where the red lines represent a continuous link and the blue dashed lines represents a discontinuous link. Used specifically on BDS-3, the system is called Concurrent Spatial Time Division which means that one satellite forms links with other satellites in the constellation at one instant in time [62]. This process was studied to improve the satellite system's positioning results to aid in navigation and precise orbit determination. Using this method, a single satellite can create links with up to 20 satellites

within one minute and the whole constellation in a short time period. This method can also be employed between MEO satellites and GEO satellites creating discontinuous links between each other which is important in the BDS system as it is not comprised solely of MEO satellites.

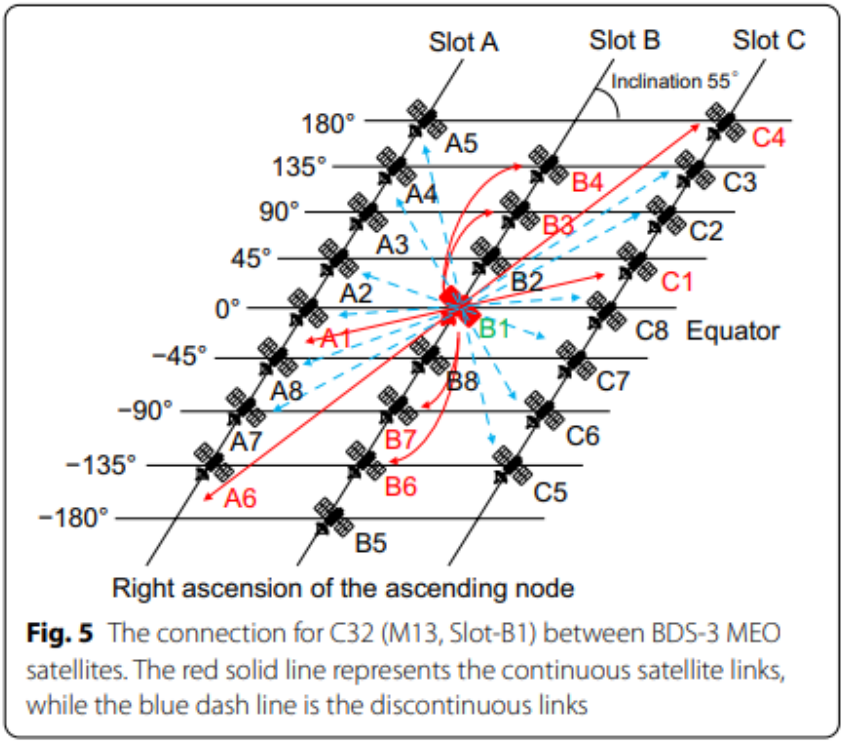

Fig. 5 The connection for C32 (M13, Slot-B1) between BDS-3 MEO satellites. The red solid line represents the continuous satellite links, while the blue dash line is the discontinuous links

Figure 2.6: Representation of Inter-Satellite Linkage [62]

2.4.4 Orbit Determination On Low Earth Orbit (LEO) Satellites

While GPS satellites in MEO orbit openly broadcast their ephemeris, LEO satellites typically do not share information about their position especially if their original purpose was not navigation [63]. The only publicly available data is the TLEs generated and published by North American Aerospace Defense Command (NORAD) daily which can be found at [27]. These TLEs can then be propagated forward but only by using special general perturbation models (commonly the SGP4 model [63], [64]). The TLE elements are mean values obtained by removing periodic variations which must be reconstructed in the same way they were removed. After TLE propagation, there can be large errors on the orders of

kilometers. To mitigate these errors, other ways of orbit determination have been studied, primarily by adding an on-board GNSS receiver.

On-board GNSS receivers can be single frequency GPS receivers, like on Quickbird and KOMP-SAT-1, or dual frequency, like on CHAMP and GRACE [65]. The same way a GPS receiver would work on Earth, the on-board receiver would need four satellites in view to be able to calculate the LEO satellite's position. Typically LEO satellites see four or more GPS satellites 99% of the time [38]. Once the observational data is obtained from the GPS, the LEO can transmit its position to a ground user. An issue arises when the LEO's location is required in near real time. The GPS data would need to be downloaded from the satellite, processed by the LEO, and distributed to a ground user in under an hour of original download [49]. The solution is precise orbit determination which is the act of accurately determining the position and velocity vectors of an orbiting satellite as well as orbit propagation that would allow the ground user or the satellite to predict the satellite's future location. POD on a LEO satellite consists of making estimates of the states based on observations usually made by integrating the equations of motion of the satellite. These results are the predicted observations that can be implemented into a least squares algorithm to minimize the observation residuals.

There are three methods for determining LEO satellite orbits. The first is the dynamic method which uses accurate force models and the adjustment of parameters to achieve an orbit solution [47]. The other method is called kinematic orbit determination. This method uses only the geometric information within the GPS measurements [47] and requires no acceleration model [66]. Unfortunately, this method relies significantly on the quality of the GPS data. Using an on-board GPS accumulates error due to receiver noise, inaccuracies of the broadcasting GPS orbit, and bias of the receiver clock [39]. The last method is called the reduced dynamic method. Combing the previous two results, this method uses both force models and geometric information [47]. In the reduced dynamic model, stochastic accelerations are estimated to reduce the errors in the force models [67]. This method is very effective with the availability of GPS data.

Two satellites, CHAMP and GRACE, are equipped with accelerometers and a dual frequency GPS receiver on-board [68]. With the use of the accelerometers on the satellite, the measured accelerations can replace the non-gravitational force models during precise orbit determination. Because of this, the orbit determination becomes a dynamic orbit determination problem instead of including pseudo-stochastic parameters in the estimation. The study done on the CHAMP and GRACE satellites determined a root-mean-square position error of less than 9 centimeters for the whole satellite period [68]. Using real data from a GRACE satellite with no accelerometer data [47] was able to achieve less than 3 centimeter level accuracy in the radial, along-track, and cross-track directions.

An example of an on-board GNSS receiver that is not GPS is the LING QIAO satellite which was launched in 2014. This was China's first LEO communication experimental satellite and had two GPS receivers for navigation and one BDS receiver on-board. The BDS receiver did not preform as well as expected because of a lower acquisition efficiency since it was only a single-frequency BDS receiver [62]. Another satellite was launched in 2013 that had a dual-frequency GPS/BDS receiver on board and calculated centimeter level accuracy using those signals [62]. The other methods previously mentioned can be used on LEO satellites for orbit determination, but with the accessibility recently of GNSS receivers, implementing one on-board a satellite has become a reliable location solution.

2.5 Coordinate Transformations

Results will be presented in the Earth-centered Earth-fixed (ECEF) coordinate frame. Deriving the acceleration from gravity in spherical coordinates is most convenient but doing so requires the coordinates to be transformed into ECEF data for comparison. One way to do this is to transform the acceleration from spherical coordinates to Earth-centered inertial (ECI) coordinates. Once the ECI coordinates are found, these can be transformed into ECEF coordinates as long as the epoch time is known.

It is important to note that these coordinate transforms go by many other names such as Tessestrial Reference Frame (TRF) or body-fixed for the ECEF frame and Celestial Reference Frame (CRF) or inertial for the ECI frame. Both of these reference frames have

the origin at the Earth's center of mass. The ECEF frame as seen in Figure 2.7 has the X-axis located at the Prime Meridian which is at 0° longitude, the Z axis extends through the North Pole at 90° latitude, and the Y axis completes a right hand coordinate frame by pointing at 90° longitude [69]. These axes rotate with the Earth. The ECI frame uses the same axis but is fixed and does not rotate [70].

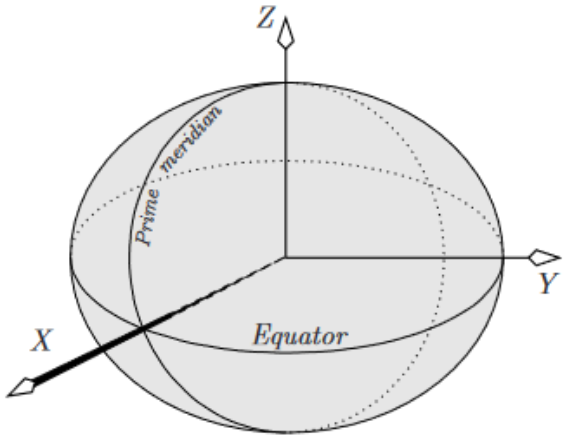

Figure 2.7: ECEF frame [69]

The first step to finding the gravity in Earth-fixed spherical coordinates at any given instant in time is to take the gradient of the gravity potential as seen in Equation (2.2) [71]. The formation of this potential will be discussed in Section 2.6.1, but the basis that needs to be known now is that the gravity is formed from spherical harmonics. Because of this, the output of the acceleration is in spherical coordinates which u_r, u_ϕ, and u_λ represent unit vectors in the spherical frame.

$$\vec{a}_g = \nabla V = \frac{\delta V}{\delta r}\vec{u}_r + \frac{1}{r}\frac{\delta V}{\delta \phi}\vec{u}_\phi + \frac{1}{r\cos(\phi)}\frac{\delta V}{\delta \lambda}\vec{u}_\lambda \tag{2.2}$$

Like discussed before, the acceleration cannot be left in the spherical frame for this research. The next step will be transforming the spherical coordinates (r, ϕ, λ) into the ECI frame (x, y, z) by way of Equation (2.3) where $a_r = \frac{\delta V}{\delta r}$, $a_\phi = \frac{1}{r}\frac{\delta V}{\delta \phi}$, $a_\lambda = \frac{1}{r\cos(\phi)}\frac{\delta V}{\delta \lambda}$ [71].

$$\begin{bmatrix} a_x \\ a_y \\ a_z \end{bmatrix} = \begin{bmatrix} \cos(\phi)\cos(\lambda) & -\sin(\phi)\cos(\lambda) & -\sin(\lambda) \\ \cos(\phi)\sin(\lambda) & -\sin(\phi)\sin(\lambda) & \cos(\lambda) \\ \sin(\phi) & \cos(\phi) & 0 \end{bmatrix} \begin{bmatrix} a_r \\ a_\phi \\ a_\lambda \end{bmatrix} \tag{2.3}$$

Lastly, the rotation from ECI to ECEF (X, Y, Z) will occur. The rotation in Equation (2.4) is the simplest form for the transformation only accounting for the Earth's rotation (ω) in which the value from Table 2.2 is used [71].

$$\begin{bmatrix} a_X \\ a_Y \\ a_Z \end{bmatrix} = \begin{bmatrix} \cos(\omega) & -\sin(\omega) & 0 \\ \sin(\omega) & \cos(\omega) & 0 \\ 0 & 0 & 1 \end{bmatrix} \begin{bmatrix} a_x \\ a_y \\ a_z \end{bmatrix} \tag{2.4}$$

Using this method can decrease accuracy by ignoring the precession, nutation, and polar motion, but if extreme precision is not necessary, this simple rotation will be sufficient. If additional accuracy is needed, the process of calculating the additional terms needed will be seen in the following paragraphs.

There are many ways to represent time: Julian Date, Universal Time Coordinated (UTC) , GPS Time, Greenwich Mean Time, etc. Therefore, to be clear with the transformation of the coordinate systems, the time system needs to be clear. With the coordinate transforms, the time used for calculations will be Julian Date although the start time (t_{start}) for this system will be UTC time of 12 February 2022 at 00:00:00 hours. This will need to be converted into a Julian Date of 2,459,622.5 days. The difference between the start time of the simulation and the J2000 epoch (t_{J2000}) is needed. The J2000 epoch is defined as starting at noon on 1 January 2000 which when converted into Julian date is $t_{J2000} = 2,451,545$ days. The difference between simulation start time and J2000 epcoh (t_0) can be seen in Equation (2.5). This equation also shows the conversion of Julian days to Julian centuries (t) which will be used in later calculations.

$$\begin{aligned} t_0 &= t_{start} - t_{J2000} \\ t &= t_0/36,525 \end{aligned} \tag{2.5}$$

For the coordinate transformations, several rotation matrices are used for calculations as seen in Equations (2.6) - (2.8).

$$\mathbf{R_1}(\alpha) = \begin{bmatrix} 1 & 0 & 0 \\ 0 & \cos(\alpha) & \sin(\alpha) \\ 0 & -\sin(\alpha) & \cos(\alpha) \end{bmatrix} \tag{2.6}$$

$$\mathbf{R_2}(\alpha) = \begin{bmatrix} \cos(\alpha) & 0 & -\sin(\alpha) \\ 0 & 1 & 0 \\ \sin(\alpha) & 0 & \cos(\alpha) \end{bmatrix} \tag{2.7}$$

$$\mathbf{R_3}(\alpha) = \begin{bmatrix} \cos(\alpha) & \sin(\alpha) & 0 \\ -\sin(\alpha) & \cos(\alpha) & 0 \\ 0 & 0 & 1 \end{bmatrix} \tag{2.8}$$

These rotation matrices are based on the rotation around one axis. For example, Equation (2.6) displays what the rotation matrix would appear like if there was rotation around the x axis for α degrees. Therefore, Equation (2.6) is rotation around the x axis, Equation (2.7) is around the y axis, and Equation (2.8) is around the z axis. A visual representation of this can be seen in Figure 2.8.

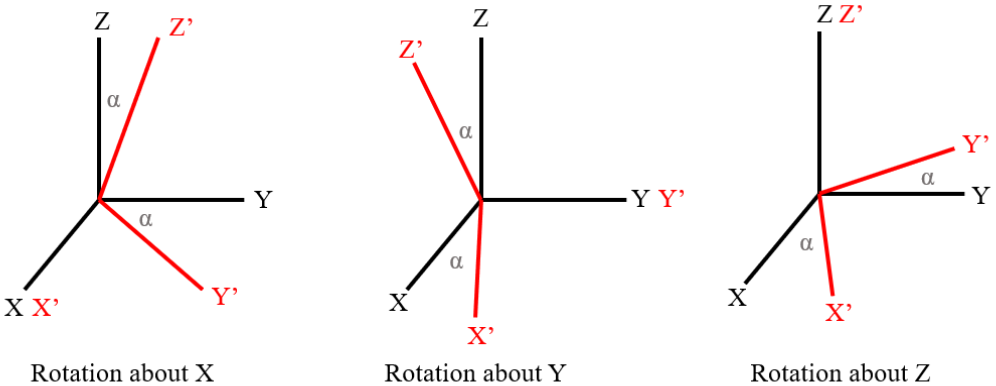

Figure 2.8: Rotation Around Each Axis

The coordinate transformation process can be seen visually in Figure 2.9. Each box represents a matrix that is formed through the processes described below. Therefore, to

convert from ECI to ECEF the ECI position vector is multiplied by each of the different boxes such as $\vec{r}_{ECEF} = \mathbf{PNR_SR_M}\vec{r}_{ECI}$. To convert from ECEF to ECI the reverse process is performed.

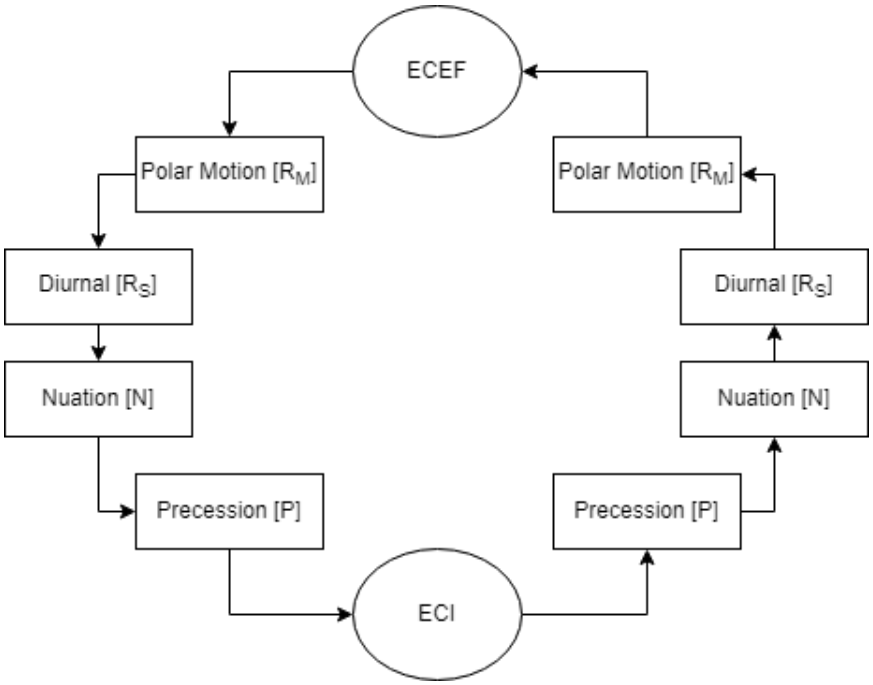

Figure 2.9: Coordinate Transformation Process

Precession [**P**]

The first matrix is the Precession Matrix which is formed in Equation (2.9).

$$\mathbf{P} = \mathbf{R_3}(-z)\mathbf{R_2}(\theta)\mathbf{R_3}(-\zeta) \tag{2.9}$$

The precession "converts a vector in the [ECEF] system, having a mean equinox at J2000, to a vector having the mean equinox of date (MOD) [42]." This is the rotation to align the equator at the epoch time with the equator at J_{2000}. The angles (displayed in decimal degrees) in Equation (2.10) represent the effects of this precession and are calculated using the Julian century. The formation of the precession matrix (Eq. (2.9)) is created using the rotation matrices and these angles.

$$\begin{aligned}\zeta &= 0.640616t + 0.00008839t^2 + (5e-6)t^3 \\ \theta &= 0.556753t - 0.000118t^2 - (1.16e-5)t^3 \\ z &= 0.640616t + 0.000304t^2 + (5.1e-6)t^3\end{aligned} \tag{2.10}$$

Nutation [**N**]

The nutation matrix takes into account the periodic effects of the Moon and transforms the true equator of date (TOD) to the MOD [42]. The angles in Equation (2.12) like the ones for the Precession define the transformation.

$$\mathbf{N} = \mathbf{R_1}(-(\bar{e} + \delta e))\mathbf{R_3}(\delta\psi)\mathbf{R_1}(\bar{e}) \tag{2.11}$$

Note that the first term in $\bar{e}$ of Equation (2.12) represents the obliquity of the ecliptic at J2000. These equations are also in decimal degree and the formation of the nutation matrix can be seen by the rotations in Equation (2.11).

$$\begin{aligned}\delta e &= 0.0026\cos(125 - 0.05295t_0) + 0.0002\cos(200.9 + 1.97129t_0) \\ \delta\psi &= -0.0048\sin(125 - 0.05295t_0) - 0.0004\sin(200.9 + 1.97129t_0) \\ \bar{e} &= 23.439291 - 0.0130042T - (1.64e-7)t^2 + (5.04e-7)t^3\end{aligned} \tag{2.12}$$

Diurnal [$\mathbf{R_S}$]

The diurnal matrix is also referred to as the sidereal time. This transformation is responsible for the time dependency of the vector components. This transformation transforms the non-rotating frame to a rotating frame [42]. This is the matrix that is used when only the simplest form of the rotation needs to be used (Eq. (2.13)).

$$\mathbf{R_S} = \mathbf{R_3}(\Theta_{GAST}) \tag{2.13}$$

The variables used when performing this rotation are the Greenwich apparent sidereal time (GAST) (Θ_{GAST}), the Greenwich mean sidereal time (GMST) (θ_{GMST}), and the equation of equinoxes (α) which can be approximated using two variables from the nutation matrix seen in 2.14. There is a key difference between GAST and GMST is which equinox is being used to measure the true equinox. GAST uses the true equinox while GMST uses the mean equinox [42]. The difference between them is how the equation of equinoxes is formed. Once GAST is found, the diurnal matrix can be calculated using Equation (2.13).

$$\begin{aligned} \theta_{GMST} &= 280.46061837 + 360.98564726629t_0 + 0.0003875T^2 - (2.6e-8)t^3 \\ \alpha &= \arctan(N(1,2)/N(1,1)) \\ \Theta_{GAST} &= \theta_{GMST} + \alpha \end{aligned} \tag{2.14}$$

Polar [$\mathbf{R_M}$]

The polar motion is how the Earth's rotational axis (Z) moves along its crust. These values are normally small in nature, but two observations have been made. The first is that the values which are normally small change a significant amount over a week to need updating. The second is that polar motion is not fully understand. This does not allow for high accuracy over very long periods of time. Because of these observations, x_p and y_p are set to zero creating an identity matrix for this research. The x_p and the y_p is how much the motion has caused a shift in the rotational axis and are measured in radians. The final rotation then is displayed in Equation (2.15).

$$\mathbf{R_M} = \mathbf{R_2}(-x_p)\mathbf{R_1}(-y_p) \tag{2.15}$$

Coordinate Transformation

The final task is to combine all the above matrices and equations to complete the transformation. The rotation rate of the Earth is needed for the velocity and acceleration terms which can be found in Table 2.2. The rotation rate is expressed in vector form as $\omega_e =$

$\begin{bmatrix} 0 & 0 & \dot{\omega} \end{bmatrix}^T$ because the Earth rotates about the z axis. The transformation from ECI to ECEF can be found in Equation (2.16) while the opposite transformation from ECEF to ECI are in Equation (2.17).

$$\begin{aligned} \vec{r}_{ECEF} &= \mathbf{R_M R_S NP} \vec{r}_{ECI} \\ \vec{v}_{ECEF} &= \mathbf{R_M}(\mathbf{R_S NP}\vec{v}_{ECI} - \omega_e \times \mathbf{R_S NP}\vec{r}_{ECI}) \\ \vec{a}_{ECEF} &= \mathbf{R_M}(\mathbf{R_S NP}\vec{a}_{ECI} - 2(\omega_e \times \mathbf{R_S NP}\vec{v}_{ECI}) + \omega_e \times \omega_e \times \mathbf{R_S NP}\vec{r}_{ECI}) \end{aligned} \tag{2.16}$$

$$\begin{aligned} \vec{r}_{ECI} &= \mathbf{P^T N^T R_S^T R_M^T} \vec{r}_{ECEF} \\ \vec{v}_{ECI} &= \mathbf{P^T N^T R_S^T}(\mathbf{R_M^T}\vec{v}_{ECEF} + \omega_e \times \mathbf{R_M^T}\vec{r}_{ECEF}) \\ \vec{a}_{ECI} &= \mathbf{P^T N^T R_S^T}(\mathbf{R_M^T}\vec{a}_{ECEF} + 2(\omega_e \times \mathbf{R_M^T}\vec{v}_{ECEF}) + \omega_e \times \omega_e \times \mathbf{R_M^T}\vec{r}_{ECEF}) \end{aligned} \tag{2.17}$$

2.6 Perturbations

Perturbations, as Vallado writes in [42], "are deviations from a normal, idealized, or undisturbed motion." One of Newton's fundamental laws is the Law of Gravitational Force. This can be simplified to the two-body problem with the Earth and the satellite being the two bodies. This two body problem is the "idealized motion" while perturbations such as Earth's mass distribution, atmospheric drag, third body effects, solar radiation pressure, thrust, magnetic fields, and ocean tides disturb this motion in the form of perturbations [42]. These perturbations can be categorized as conservative and non-conservative. This section will focus on the differences of each and which affect LEO satellites most.

In order to propagate the satellite's perturbations, a choice of propagation method (analytical or numerical) must be chosen. Analytical propagators have the added benefit of being faster computationally, but because they reduce model fidelity, they also can be less accurate [4], [8]. Numerical propagators can model physical phenomena through the use of large integrations which increases the accuracy of the model but slows down the

computation speed [4], [8]. As higher order terms are integrated, this effect is seen. The model used in this research has sufficient accuracy using lower order terms and therefore allows for faster computation time when the numerical method is used.

The following sections will describe the differences in the types of perturbations. The types of perturbations include gravity, third body, atmospheric drag, solar radiation pressure, and various others. The total acceleration on the body of a satellite can be seen in Equation (2.18).

$$\vec{a} = \vec{a}_g + \vec{a}_{3B} + \vec{a}_D + \vec{a}_{SRP} + \vec{a}_{other} \tag{2.18}$$

Overall, effect of each perturbation relies on various factors such as orbital height, atmospheric effects, and sun visibility. Therefore, depending on the needed accuracy of the orbit, many of these perturbations can be ignored. For this research, the perturbations for gravity and atmospheric drag will be included in propagation.

2.6.1 Conservative

A conservative force is when the total energy is constant, no energy is gained or lost during the movement of a particle. The conservative forces with satellites are the mass distribution in the form of spherical harmonics and third-body forces.

Mass Distribution (Spherical Harmonics)

The largest of the perturbations effecting the satellite in LEO is gravity [72]. The gravity perturbation is caused primarily by Earth's oblateness [71]. The Spirent simulator (the simulator used for analysis in this thesis) uses a spherical harmonic representation of gravity which is found widely in literature [71]. This gravity potential, seen in Equation (2.19), is the basis for the estimation method for the ballistic coefficient which will be discussed later.

$$V = \frac{\mu}{r} \sum_{l=0}^{\infty} \left(\frac{a_e}{r}\right)^l \sum_{m=0}^{l} P_{l,m}(\sin(\phi))[C_{l,m}\cos(m\lambda) + S_{l,m}\sin(m\lambda)] \tag{2.19}$$

Because of this, it is crucial that the gravity model be replicated with extreme accuracy.

Spherical harmonics are used to describe how a quantity varies across the surface of a sphere which all planets in the solar system are assumed to be [73]. This is the most accurate way to represent the gravity field of the Earth. As more research is done on the gravity field, more spherical harmonic coefficients are added creating more accurate gravity models. It is shown in [6], when comparing three different propagation models using a higher order model increases accuracy without trading off computation time. The gravity model used in the Spirent is set to a degree of 4 which allows for accurate replication of the gravity field when propagating.

In Equation (2.19), the spherical coordinates are r, ϕ, and λ. ϕ represents the geocentric latitude and λ is the longitude angle [74]. Within Equation (2.19), there are Legrendre coefficients ($C_{l,m}$ and $S_{l,m}$) that correspond to the mathematical modeling of the Earth's oblateness [42]. As the order (m) and degree (l) increases, the harmonic terms represent finer variations in the potential [71]. Therefore, the largest gravitational effects are felt when the degree and order are lowest. The gravitational zones are:

- zonal ($m = 0$): Corresponds to degrees of latitude with the largest being at the equator ($l = 2$) [6], [42], [71], [73], [74]. This Legrendre coefficient is commonly represented with the J notation such that $J_l = -C_{l,0}$ [74].

- tesseral ($l \neq m \neq 0$): These harmonics include both the latitude and longitude variations of the Earth's oblateness. These divide the Earth up into a checkerboard type pattern [42], [73].

- sectoral ($l = m$): These harmonics focus only on longitudinal variations which at the poles equals zero [42], [74].

Each of these harmonic terms can be seen visually in Figure 2.10. The zonal harmonics are the largest coefficients acting in the spherical harmonic model. If a high degree of accuracy is not required, the zonal harmonics are sometimes the only values calculated thereby simplifying the calculations [6], [71].

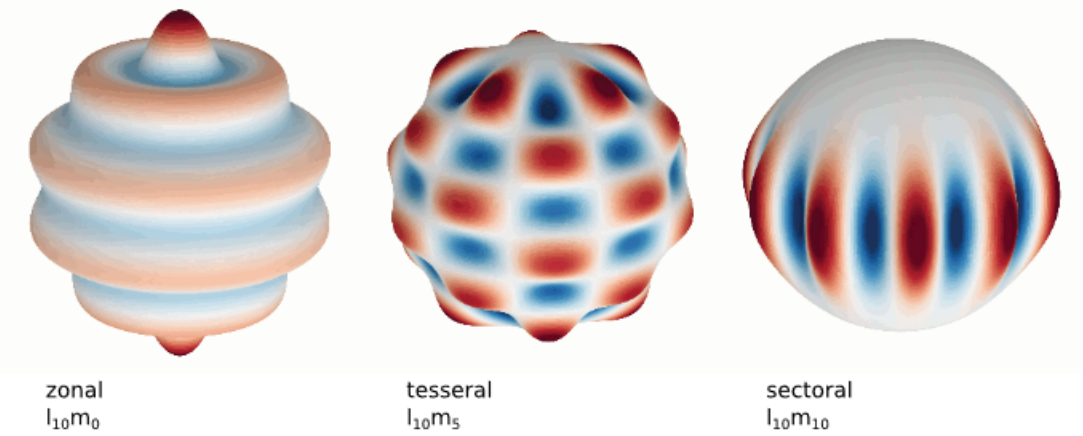

Figure 2.10: Spherical Harmonic Types [73]

The gravity potential can be broken down to represent each of the harmonic terms as well. In Equation (2.21), the first term is the potential from representing the Earth as a point mass [71].

$$V = \frac{\mu}{r}\left[1 - \sum_{l=2}^{\infty} J_l \left(\frac{R_E}{r}\right)^l P_l[\sin(\phi)] + \sum_{l=2}^{\infty}\sum_{m=1}^{l}\left(\frac{R_E}{r}\right)^l P_{l,m}\left[\sin(\phi)\right]\left\{C_{l,m}\cos(m\lambda) + S_{l,m}\sin(m\lambda)\right\}\right] \quad (2.20)$$

The second term in equation is the zonal terms which shows the substitution of $J_l = -C_{l,0}$. Lastly, the third term is the tesseral harmonics. This term represents both the tesseral and the sectoral terms because it is commonly regarded that the sectoral terms are only a special case of the tesseral harmonics [42]. If only the zonal terms are used in analysis, the longitudinal component of acceleration will be zero [71].

$$V = \frac{\mu}{r}\left[1 - \sum_{l=2}^{\infty} J_l \left(\frac{R_E}{r}\right)^l P_l[\sin(\phi)] + \sum_{l=2}^{\infty}\sum_{m=1}^{l}\left(\frac{R_E}{r}\right)^l P_{l,m}\left[\sin(\phi)\right]\left\{C_{l,m}\cos(m\lambda) + S_{l,m}\sin(m\lambda)\right\}\right] \quad (2.21)$$

The equation for the psuedo-potential function (Eq. (2.21)) includes the conventional Legendre polynomial (Eq. (2.22)) and associated Legendre polynomials (Eq. (2.23)) and coefficients of spherical harmonics (Eq. (2.24)).

$$P_l[\gamma] = \frac{1}{2^l l!}\frac{d^l(\gamma^2-1)^l}{d\gamma^l} \quad (2.22)$$

$$P_{l,m}[\gamma] = \frac{1}{2^l l!}(1-\gamma^2)^{m/2}\frac{d^{l+m}}{d\gamma^{l+m}}(\gamma^2-1)^l \quad (2.23)$$

$$\begin{aligned} C'_{l,m} &= \int_{body} r^l \frac{(l-m)!}{(l+m)!} P_{l,m}[\sin(\phi)]\cos(m\lambda)\, dm_E \\ S'_{l,m} &= \int_{body} r^l \frac{(l-m)!}{(l+m)!} P_{l,m}[\sin(\phi)]\sin(m\lambda)\, dm_E \end{aligned} \quad (2.24)$$

The associated Legendre polynomial can be used for all cases, but the conventional Legendre polynomial is a simplified version to be used with zonal terms only [42]. A list of coefficients for the JGM-3 gravity model can be found in Appendix D of [74].

To find the gravity in Earth-fixed spherical coordinates at any given time, the gradient of the potential (Eq. (2.19)) must be taken as seen in Equation (2.25) where u_r, u_ϕ, and u_λ are unit vectors in the spherical frame [71].

$$\vec{a}_g = \nabla V = \frac{\delta V}{\delta r}\vec{u}_r + \frac{1}{r}\frac{\delta V}{\delta \phi}\vec{u}_\phi + \frac{1}{r\cos(\phi)}\frac{\delta V}{\delta \lambda}\vec{u}_\lambda \quad (2.25)$$

Third-Body

Depending on how accurate the solution must be and the orbiting altitude of the satellite, a useful term to include is the third body effects of the Sun, Moon, and any other bodies thought to perturb the satellite seen in Equation (2.26).

$$\vec{a}_{3B} = \mu_3 \left(\frac{\vec{r}_{S3}}{r_{S3}^3} - \frac{\vec{r}_{E3}}{r_{E3}^3} \right) \tag{2.26}$$

These effects are greater as the effects of the atmospheric drag decreases [42]. Therefore, this term will be omitted during propagation based on the orbiting altitude of the satellites being studied.

The subscript 3 refers to the third body that is doing the perturbing. If the Sun is the perturbing third body the gravitational constant (μ_3) is 1.32712440018e20 m^3/s^2. If the Moon is the third body, then μ_3 is 4.9048695e12 m^3/s^2. $\vec{r}_{S3}$ refers to the vector from the satellite to the perturbing body with r_{S3}^3 being the Euclidean norm of that vector. $\vec{r}_{E3}$ is the vector from the Earth to the perturbing body with r_{E3} being the norm of the vector. The first term in Equation (2.26) is known as the direct effect and the second term as the indirect effect showing that this is independent of the satellite's location [74].

2.6.2 Non-conservative

A non-conservative perturbation is defined as a force that may lose or gain energy such as through friction or thrust. While gravity is the largest force effecting the satellite, the non-conservative forces must be included or the propagated position solution will be incorrect over time.

Atmospheric Drag

The atmospheric drag is the largest non-gravitational force acting on the satellite and after gravity, it is the second-largest force acting on satellites below 500 km [2], [42], [67]. This is an issue because with satellites at that altitude, the amount of atmospheric drag can greatly influence the orbital decay of the satellite by reducing the orbital energy of the

satellite [2]. The atmospheric drag reiterated from earlier in Equation (2.27) is comprised of physical attributes of the satellite (area (A), mass (m), and drag coefficient (c_d) and environmental attributes (relative velocity and density).

$$\vec{a}_D = -\frac{1}{2}\frac{Ac_d}{m}\rho|\vec{v}_{rel}|^2\frac{\vec{v}_{rel}}{|\vec{v}_{rel}|} \tag{2.27}$$

Within the atmospheric drag, certain quantities can be difficult to determine alone and are combined to form the term 'ballistic coefficient.' This comprises the satellite's mass, coefficient of drag, and cross-sectional area. The ballistic coefficient is deterministically unknown quantity especially when the satellite is in orbit.

Solar Radiation Pressure (SRP)

This perturbation is influenced by the Sun and is the result of a "transfer of momentum through impact, reflection, absorption, and re-emission of photons" [74]. This perturbation seen in Equation (2.28) increases as the orbiting altitude of the satellite increases.

$$\vec{a}_{SRP} = -P\frac{\nu A}{m}C_R\vec{u} \tag{2.28}$$

One aspect of this perturbation is the difficulty of modeling the solar cycles and variations [42]. When there is a large solar storm, the effect of SRP is can be very pronounced compared to the other perturbations and the opposite is true for a period of low solar storm activity.

The value for the eclipse factor (ν) is either 0 or 1 depending on the expose of the satellite to the Sun. The variable C_R is the reflectivity coefficient which is approximated at 1 but can fluctuate between 0 and 2. This variable shows how the satellite reflects the incoming radiation with 0 being no radiation reflection, 1 is all the radiation being absorbed, and a value of 2 represents all radiation as reflected. $\vec{u}$ is the unit vector pointing from the satellite to the Sun. P is the momentum flux from the Sun at the satellite's location. For Earth orbiting satellites, this value is set at a constant 4.56e-6 N/m^2 [74]. One variable difficult to determine in Equation (2.28) is the cross-sectional area (A) exposed to the sun.

The area is vital piece in determining how much force the Sun's radiation is exerting on the satellite and cannot be known with extreme certainty and therefore an average is used [42].

Other

Perturbations that are included in the category "other" are ones that influence a satellite's orbit but are so small that they are often times neglected unless the most extreme accuracy is required [42]. The list below will briefly explain what types of perturbations would be included in this category and a more complex definition can be found in [42], [74].

- Tides

  Tides are being included in the gravitational models as computational resources grow. Most often times when tides are mentioned the primary tide being discussed is the ocean tides, but the term tides can also refer to solid Earth tides, pole tides, and atmospheric tides [42]. Overall, the definition for a tide is the gravitational distortion caused by an external body.

- Magnetic Field Effects

  Magnetic field effects are calculated to determine the effects of charged particles on the satellite [42]. A spherical harmonic representation is chosen to denote the magnetic-potential field.

- Thrust

  It might seem counter-intuitive to include thrust because it can be a large perturbation. The difference is that thrust is often planned and the perturbation effect of it can be known [42]. Being a function of mass-flow rate and specific impulse of fuel, the thrust can be modeled easily. A numerical propagation method can be used to predict the change in velocity from the thrust maneuver [42]. This change in velocity can be added to the original velocity vector and propagation of the satellite can continue as normal.

Chapter 3

Visibility Analysis

3.1 Background

A visibility analysis was conducted to determine the length of time the satellite would be in view of a ground receiver. The theory is that if the LEO satellite had a loss of GPS signal during the time of view, the satellite would need to propagate its trajectory forward in order to relay to the ground user an accurate position.

The analysis was done for a mask angle of 0 degrees, which is achieved only in open water, 10 degrees, which is the average mask angle for a LEO satellite, and 20 degrees, which for optimal visibility should be the largest mask angle set. The difference in what each mask angle looks like can be seen in Figure 3.1 with 0° level with the horizon.

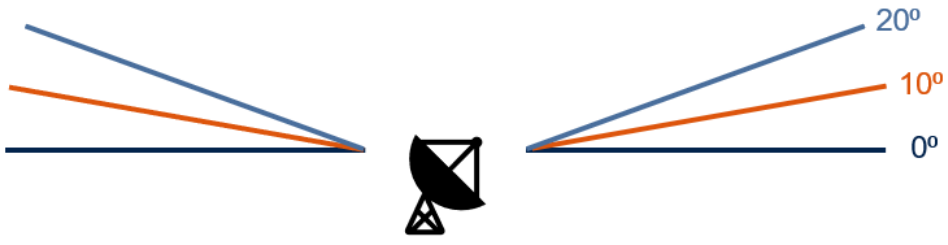

Figure 3.1: Visual Mask Angle

The satellite orbit was simulated on Spirent for 72 hours at an increment of one second. The orbiting altitude of the satellite was approximately 400 kilometers and almost

completely circular. A base station was placed arbitrarily at latitude of 28.689524° and longitude of 47.840452°. The simulated orbit (red) and base station location (yellow star) can be seen in Figure 3.2.

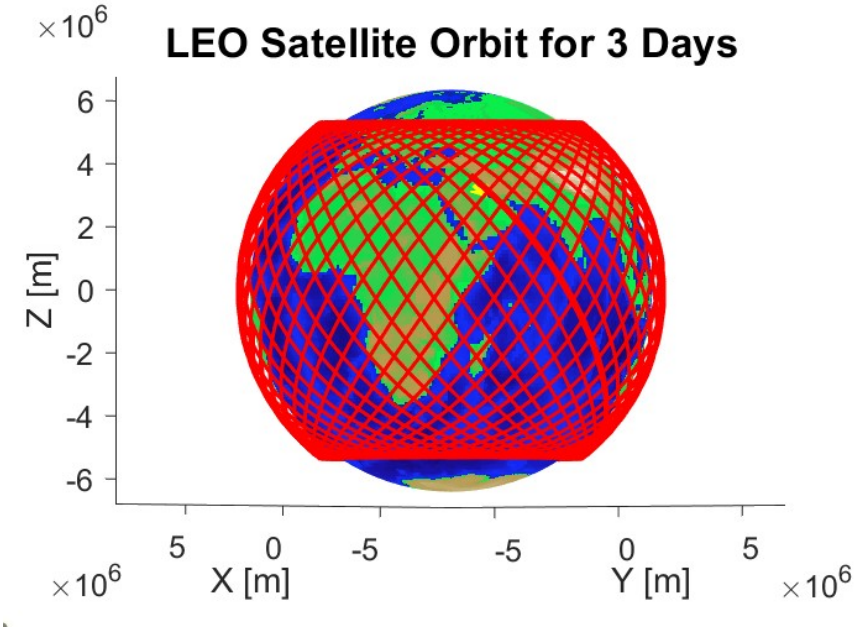

Figure 3.2: Simulated Satellite Orbit for 72 Hour Duration

3.2 Comparison of Mask Angles

The satellite visibility was observed over a 72-hour period and the visibility duration was compared for the different mask angles. This was done by determining the azimuth and elevation angles of the satellite, and if the satellite was below the mask angle value, the satellite was set to "not visible." Using this method, it is relatively easy as long as the receiver's position and the satellite's azimuth and elevation are available to determine if a satellite is currently visible. The differences for each mask angle can be seen in Figures 3.3-3.5 as well as in Table 3.1.

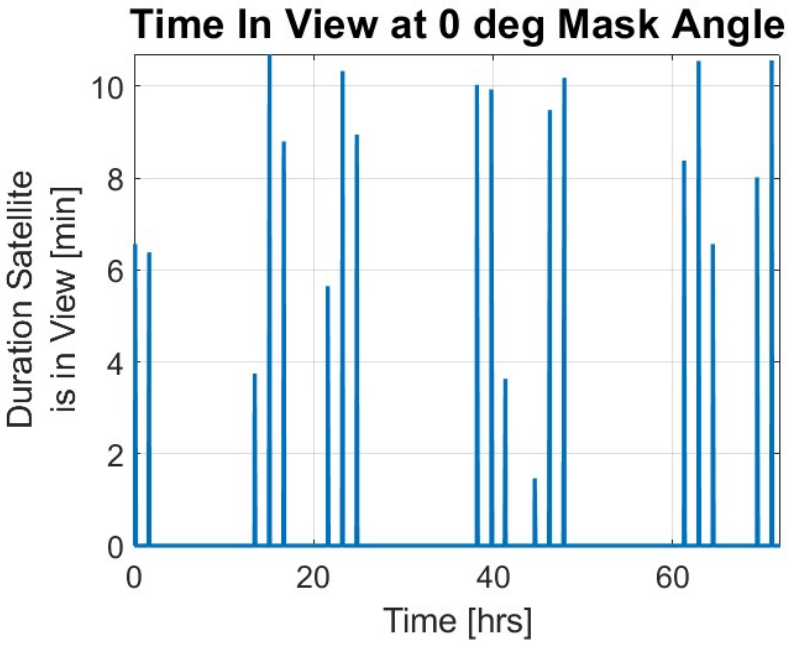

Figure 3.3: 0° Mask Angle

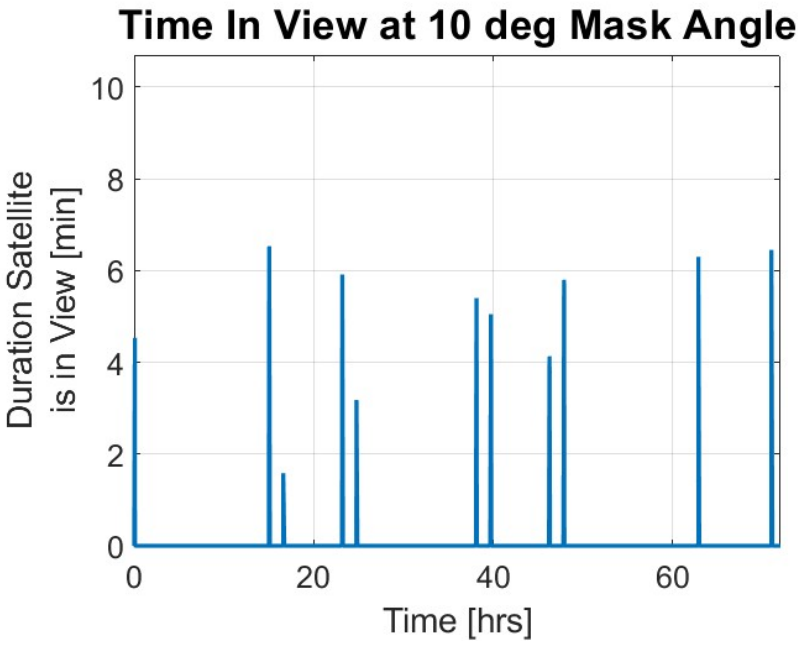

Figure 3.4: 10° Mask Angle

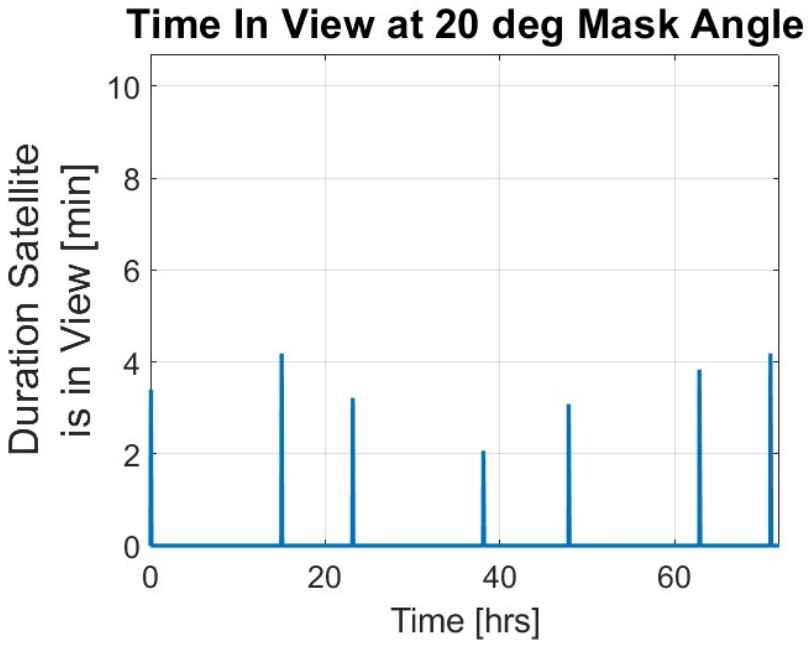

Figure 3.5: 20° Mask Angle

	0°	10°	20°
Total Time in View	145.0 min	54.9 min	24.0 min
Maximum Time in View	10.7 min	6.5 min	4.2 min
Times Visible	19	11	7

Table 3.1: Results of Different Mask Angles

As expected, the longest maximum time in view was found at the 0° mask angle and the shortest amount of time was at the 20° mask angle. From this analysis, it was found that the maximum amount of time that a satellite orbiting at 400 kilometers would be in view would be at around 10 minutes, with the commonly used mask angle of 10° having a maximum time in view of only 6.5 minutes. Since the satellite is in view for 10 minutes or less, propagation would only need to occur for a maximum of 10 minutes to obtain an estimate of the amount of error accumulated.

Chapter 4

Propagation Analysis

4.1 Background

When propagating the satellite in orbit, it is important to have the correct gravity model. One way to do this is through the use of numerically propagating the satellite. For the Spirent orbit, the final acceleration model included the combined effects of gravity, atmospheric drag, and the effect of Earth's rotation which can be seen in Equation (4.1). Therefore, the final acceleration model becomes $\vec{a} = \vec{a}_g + \vec{a}_e - \vec{a}_D$.

$$\vec{a_e} = \begin{bmatrix} 2\omega v_y + \omega^2 r_x \\ -2\omega v_x + \omega^2 r_y \\ 0 \end{bmatrix} \tag{4.1}$$

Using the developed acceleration model, the satellite's position and velocity is fed through a Runge-Kutta integration scheme. For this research, ode45 in Matlab was used with tolerances of relative error at 1e-9 and absolute error as 1e-10. With the derivative of position being the velocity value and the derivative of velocity being the acceleration model, which can be seen in Equation (4.2). This model was found to be the best fit for the Spirent data as the Spirent gravity model is not freely published.

$$\begin{aligned} \dot{\vec{r}} &= \vec{v} \\ \dot{\vec{v}} &= \vec{a}_g + \vec{a}_e - \vec{a}_D \end{aligned} \tag{4.2}$$

4.2 Propagation Error Over One Orbit

A Monte Carlo simulation was performed for the Iridium satellite which will be presented here. The following figures will show the effect of the propagation duration on final position error of the satellite. The simulation covered a total of 720 iterations which represented one orbit and approximately 90 minutes. Using the Runge-Kutta method mentioned in 4.1, the position and velocity values were integrated for a set amount of time. At the end of this time span, the position error was obtained and this is what is seen in Figure 4.1. This figure shows the position error at the end of the propagation time while Figure 4.2 shows the velocity error at the end of propagation.

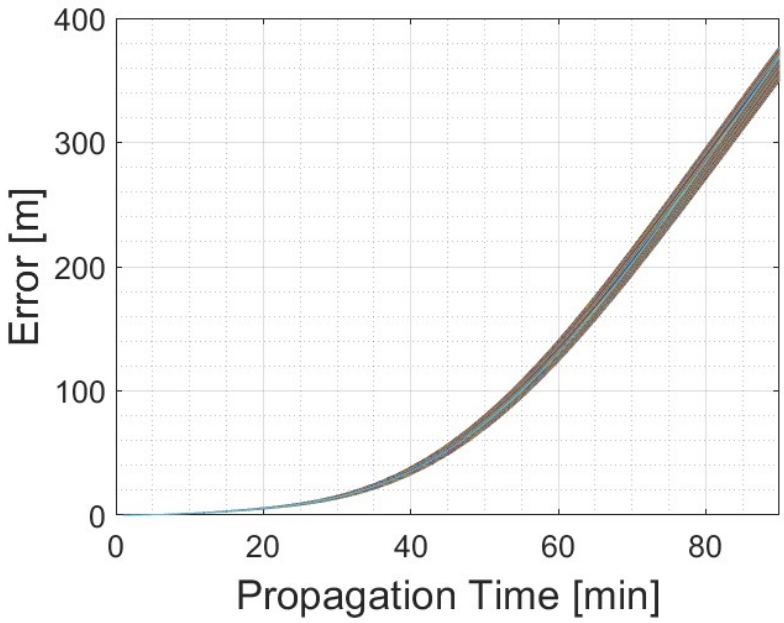

Figure 4.1: Position Propagation Error Over One Orbit

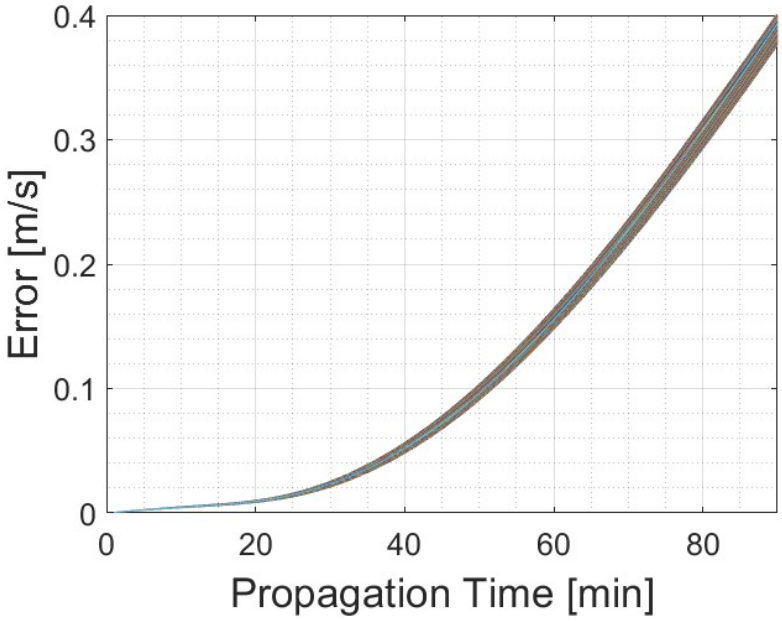

Figure 4.2: Velocity Propagation Error After One Orbit

Figure 4.3 shows the cumulative distribution function (CDF) for the entire 90-minute orbit propagation. The bars represent 10 meters of propagation error. For 50% of the orbit duration, the final propagation was below 60 meters of error. During the entire orbit, all the error was less than 380 meters of error which can also be seen in Figure 4.1. The velocity CDF in Figure 4.4 shows that the total velocity error for each iteration stays below 0.4 meters per second for one orbit.

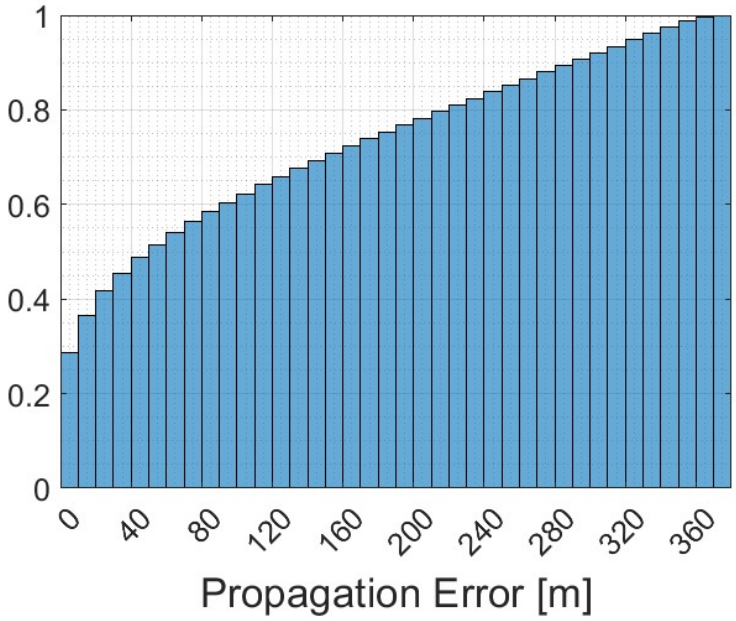

Figure 4.3: CDF Distribution of Position Propagation Error After One Orbit

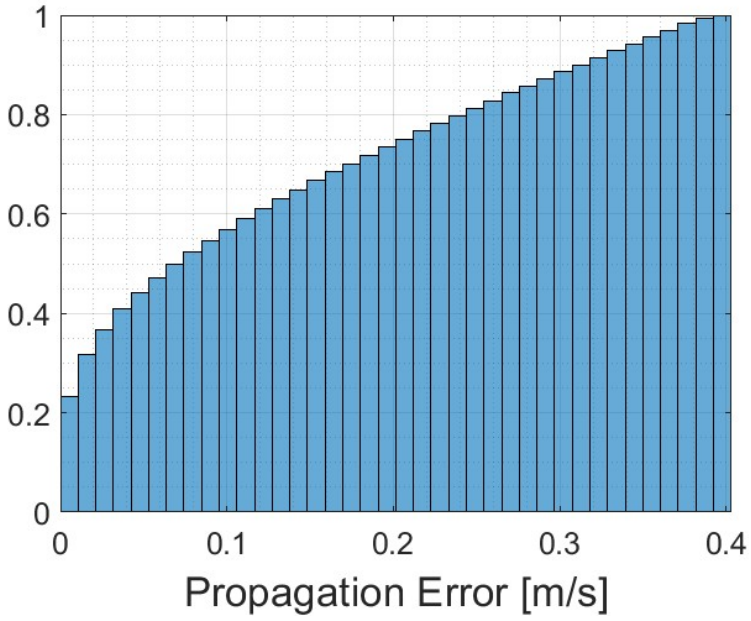

Figure 4.4: CDF Distribution of Velocity Propagation Error After One Orbit

4.3 Propagation Error After 10 Minutes

Next, the error was determined after 10 minutes of propagation. As stated in Section 3.2, having a propagation time of 10 minutes would be sufficient if the satellite were to lose GPS signal right before being in view or during time in view. Figures 4.5 and 4.6 display

the CDF distribution for all 720 Monte Carlo runs after 10 minutes of propagating. All runs at 10 minutes stayed below 1.595 meters of error which would be sufficient for navigation purposes. The velocity error at 10 minutes is even smaller at less than 6e-3 meters per second.

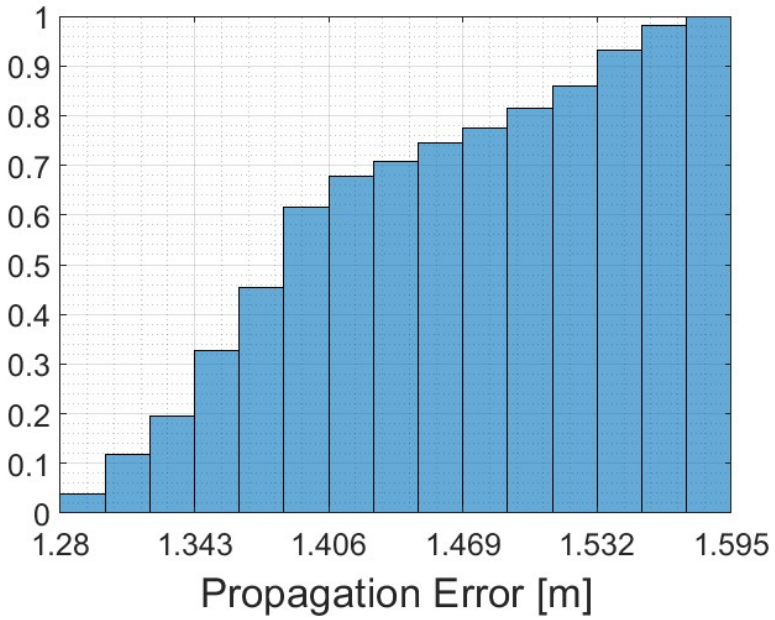

Figure 4.5: CDF Distribution of Position Propagation Error After 10 Minutes

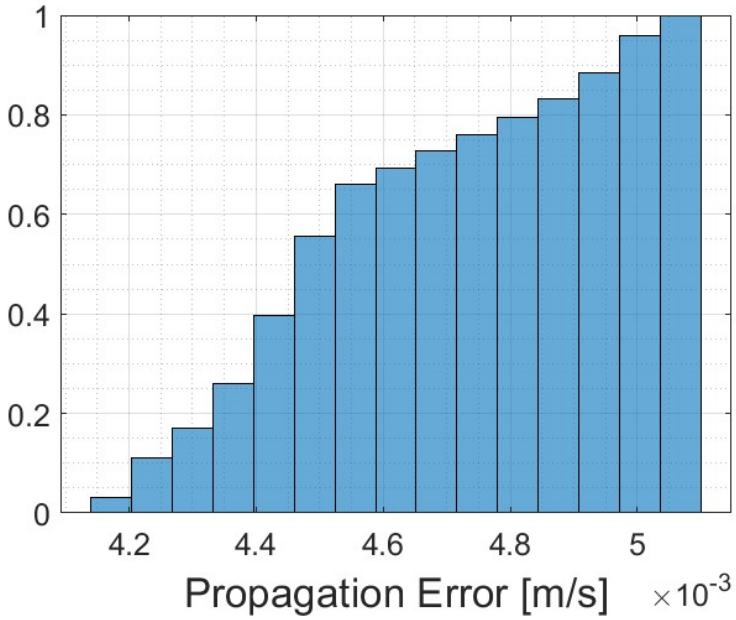

Figure 4.6: CDF Distribution of Velocity Propagation Error After 10 minutes

Chapter 5

Modeling GPS Loss Over Time

5.1 Background

Modeling the GPS outages helps the end user understand how accurate the propagation solution over time will be at different points in the orbit. The results from this section will be compared to the results in 4 to show the impact the ballistic coefficient has on position and velocity error.

5.2 Procedure

First, to understand how the GPS outage is simulated, the procedure of orbit determination and propagation must be understood. To simulate an on-board real time orbit determination, an extended Kalman filter was used while measurements were active. During this process the state vector, $\vec{x} = [\vec{r} \quad \vec{v}]^T$, was fed through time update where the state transition matrix was formed using Equation (5.1).

$$\mathbf{A} = \begin{bmatrix} \mathbf{0}_{3x3} & \mathbf{I}_{3x3} \\ \delta\mathbf{a}/\delta\mathbf{r} & \delta\mathbf{a}/\delta\mathbf{v} \end{bmatrix} \tag{5.1}$$

The partial derivative matrices in Equation (5.2) and (5.3) were formed using the equation developed for acceleration, $\vec{a} = \vec{a}_g + \vec{a}_e - \vec{a}_D$ where the gravity component ($\vec{a}_g$) was only a function of position, drag ($\vec{a}_D$) was only a function of velocity, but the acceleration due to Earth's rotation ($\vec{a}_e$) is a function of both position and velocity.

$$\frac{\delta \mathbf{a}}{\delta \mathbf{r}} = \begin{bmatrix} \delta a_x/\delta r_x & \delta a_x/\delta r_y & \delta a_x/\delta r_z \\ \delta a_y/\delta r_x & \delta a_y/\delta r_y & \delta a_y/\delta r_z \\ \delta a_z/\delta r_x & \delta a_z/\delta r_y & \delta a_z/\delta r_z \end{bmatrix} \tag{5.2}$$

$$\frac{\delta \mathbf{a}}{\delta \mathbf{v}} = \begin{bmatrix} \delta a_x/\delta v_x & \delta a_x/\delta v_y & \delta a_x/\delta v_z \\ \delta a_y/\delta v_x & \delta a_y/\delta v_y & \delta a_y/\delta v_z \\ \delta a_z/\delta v_x & \delta a_z/\delta v_y & \delta a_z/\delta v_z \end{bmatrix} \tag{5.3}$$

Once the state transition matrix was formed, time update was performed. This was performed by integrating the state vector to the next time step. To do this, the time derivative was formed by $\dot{\vec{x}} = [\vec{r} \quad \vec{a}_g + \vec{a}_e - \vec{a}_D]^T$. The covariance was then integrated by first performing the time derivative as well using this equation: $\dot{\mathbf{P}} = \mathbf{AP} + \mathbf{PA}^T + \mathbf{Q}$. $\mathbf{Q}$ was tuned arbitrarily to produce the best results. $\mathbf{P}$ was integrated using the same procedure as $\vec{x}$.

Next, the measurement update was performed. First, the observation matrix was formed. Since this is an extended Kalman filter, the partial derivatives of the observation equations were taken to create the observation matrix. In this case, the measurement vector, $\vec{z} = [\vec{r} \quad \vec{v}]^T$, is the same as the state vector. This, therefore, produces the measurement matrix seen in Equation (5.4).

$$\mathbf{H} = \begin{bmatrix} \mathbf{I}_{3x3} & \mathbf{0}_{3x3} \\ \mathbf{0}_{3x3} & \mathbf{I}_{3x3} \end{bmatrix} \tag{5.4}$$

Once the observation matrix is formed, the Kalman Filter gain is found through $\mathbf{K} = \mathbf{PH^T}(\mathbf{HPH^T} + \mathbf{R}^{-1})$. $\mathbf{R}$ was tuned using the variance values produced from the Novatel. After this, the correction equations were performed through the use of Equation (5.5) where $\hat{\vec{z}}$ was formed from the position and velocity estimates from $\vec{x}_{k+1}$.

$$\begin{aligned} \vec{x} &= \vec{x}_{k+1} + \mathbf{K}(\vec{z} - \hat{\vec{z}}) \\ \mathbf{P} &= (\mathbf{I} - \mathbf{KH})\mathbf{P}_{k+1} \end{aligned} \tag{5.5}$$

After the orbit determination (EKF) section was run, a GPS outage was simulated by completely stopping the measurements. From there, the last known position and velocity were input into a Runge-Kutta scheme to propagate the solution forward in time. A Runge-Kutta scheme was chosen because it had the ability to increase accuracy of the propagated solution as well as control the tolerances better than if the measurement update section of the Kalman filter was avoided. To understand more about the equations used in the Runge-Kutta scheme please refer to Section 4.1.

5.3 GPS Outage Simulation Results

A GPS outage was simulated at different parts in the orbit for different amounts of time. In Figure 5.1 and 5.2 each line represents a different GPS outage occurrence at a different section of the orbit. This was repeated for 720 iterations which would be 12 hours of an orbiting satellite. The black dotted line in each figure represents one sigma bounds.

Figure 5.1 has a maximum error of less than 35 kilometers over 8 orbits of a satellite. 35 kilometers of error would not be sufficient to be used as navigation, but if the amount of error was known, it could then be corrected. For the first 200 iterations, the satellite stays below 5 kilometers of error and has a relatively low error point. This is believed to be because once the satellite starts accumulating error, the error starts to grow quickly.

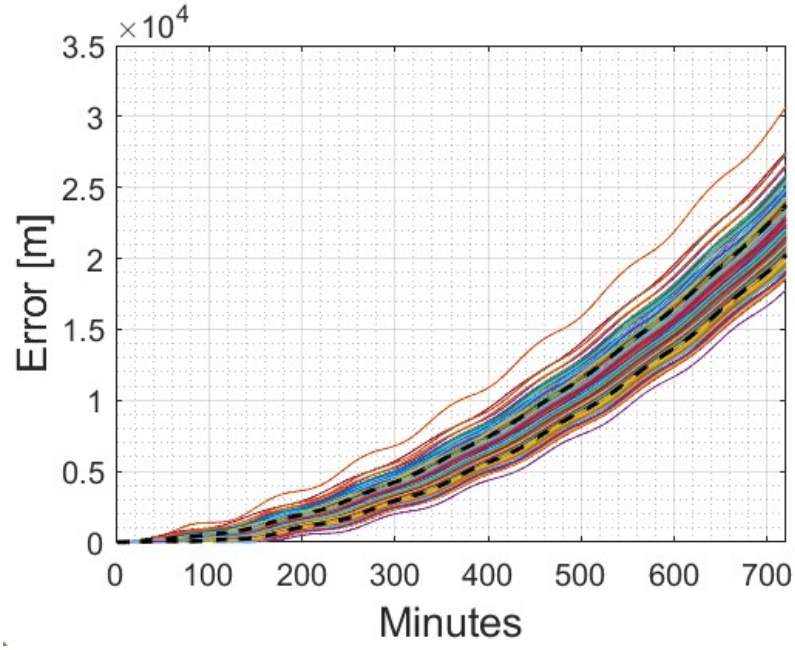

Figure 5.1: Position Error of GPS Loss

This phenomenon can also be seen in the velocity errors in Figure 5.2. As the velocity error starts to grow significantly large, it is translated into error on the position.

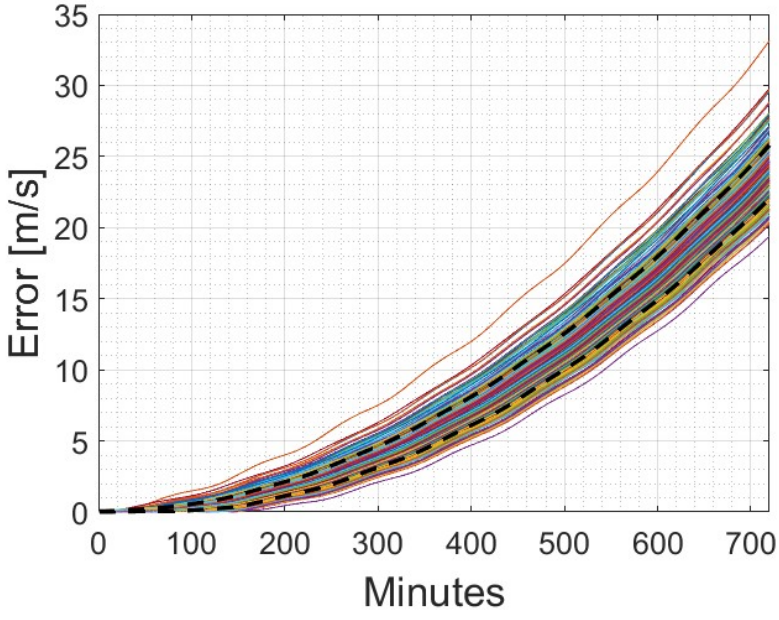

Figure 5.2: Velocity Error of GPS Loss

5.4 Statistical Distribution of Error

The next few graphs will show the statistics for the propagation error. Figure 5.3 shows the position error over the entire GPS loss events. 50% of the time the orbit is below 5000 meters of error. Referring back to Figure 5.1, the position error stays below 5000 meters of error for 300 iterations which is approximately equivalent to three orbits.

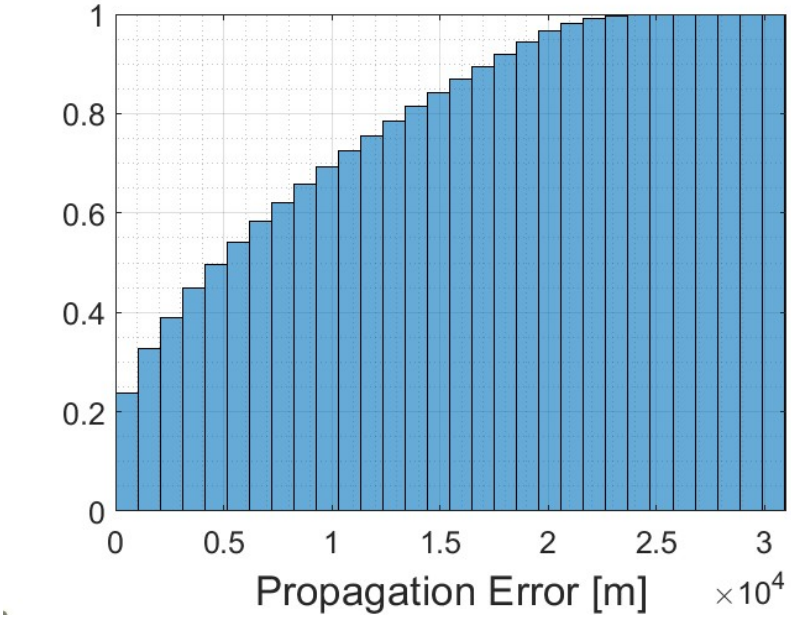

Figure 5.3: CDF of Position Propagation Error

Figure 5.4 shows the velocity error where 50% of the time, the error is below five meters per second of error at the end of the propagation period. This, like the position error, is also equivalent to three orbits. Therefore, the expected accuracy after three orbits is around three kilometers and five meters per second.

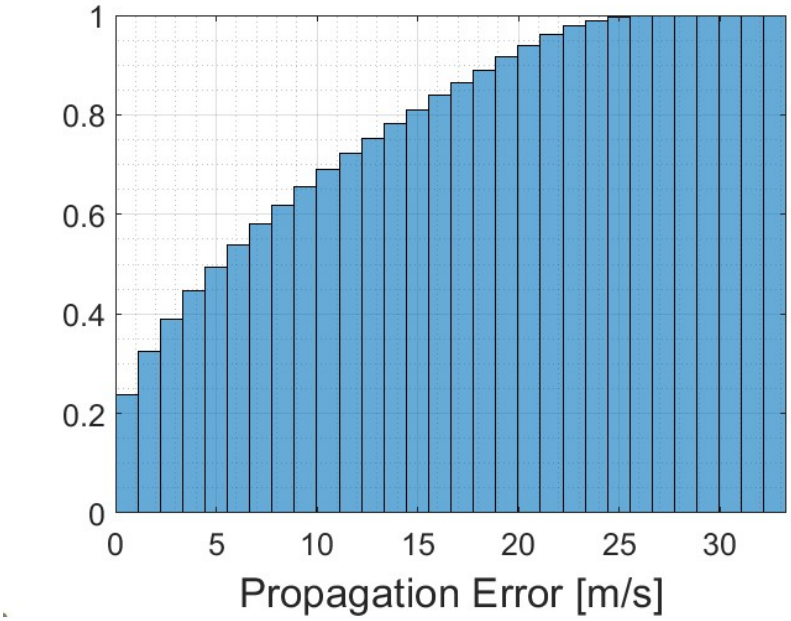

Figure 5.4: CDF of Velocity Propagation Error

Chapter 6

Ballistic Coefficient Estimation

6.1 Background

One variable in the drag equation that would be beneficial to estimate and model would be the ballistic coefficient. To estimate the ballistic coefficient, the drag equation must be rearranged to solve for the coefficient, seen in Equation (6.1).

$$B = \frac{2\vec{a}_D}{\rho|\vec{v}|\vec{v}} \tag{6.1}$$

An issue arises because both the velocity and the drag are 3x1 vectors. Normally, the components could be separated and each solved individually to obtain the same ballistic coefficient by choosing any of the equations in Equation (6.2).

$$\begin{aligned} B &= \frac{2a_{Dx}}{\rho|\vec{v}|v_x} \\ B &= \frac{2a_{Dy}}{\rho|\vec{v}|v_y} \\ B &= \frac{2a_{Dz}}{\rho|\vec{v}|v_z} \end{aligned} \tag{6.2}$$

This would work until the individual velocity components approaches zero as it changes from a positive to negative value or vice versa. One solution is to create a weighted average of all the individual components, but the other more effective route is to perform the pseudo-inverse on the velocity vector.

The pseudo-inverse which is also called the Moore-Penrose inverse (Eq. (6.3)).

$$B = (\vec{v}^T\vec{v})^{-1}\vec{v}\frac{2\vec{a}_D}{\rho|\vec{v}|} \tag{6.3}$$

The pseudo-inverse is a useful tool when trying to find the solution of a scalar variable from two vectors. For the case here, the velocity and acceleration are both vectors while the ballistic coefficient is a scalar quantity. The oscillation the occurs is due to the velocity and acceleration vectors having both positive and negative values. As one value approaches zero, the other values in the inverse will compensate by becoming larger causing oscillation to be seen. While this oscillation repeats, it does eventually converge to a common solution.

6.2 Estimation Procedure

The process for estimating the ballistic coefficient can be seen in the block diagram in Figure 6.1.

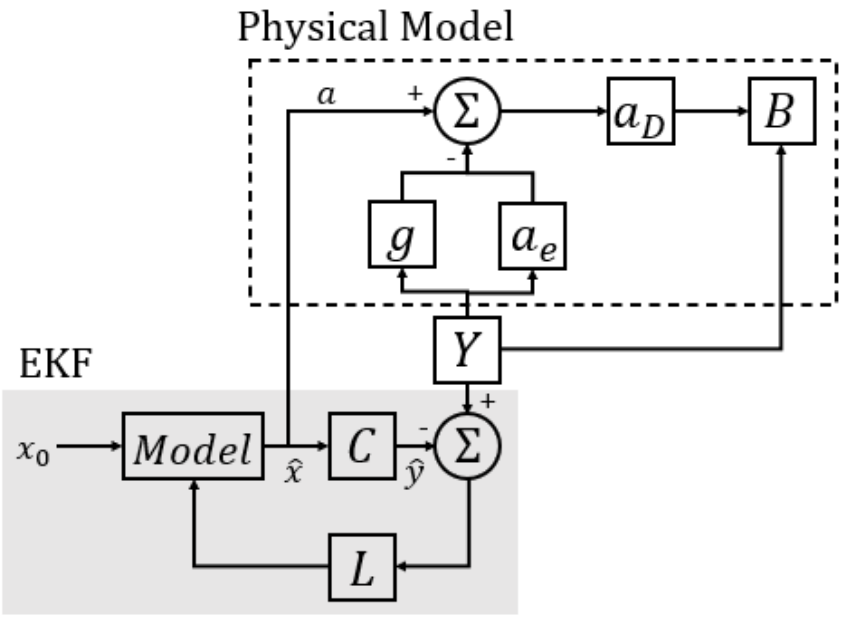

Figure 6.1: Ballistic Coefficient Estimation Block Diagram

The first step is to determine the total acceleration acting on the satellite (a). To do this, the Luenberger estimator in the shaded gray area is performed. The initial conditions are set to the initial states of the satellite with the state vector being $\vec{x} = [\vec{r} \quad \vec{v} \quad \vec{a} \quad \vec{j}]^T$. This is fed through the model which is of type $\dot{\vec{x}} = \mathbf{A}\vec{x}$ with $\mathbf{A}$ being shown in Equation

(6.4) as a 12 x 12 matrix where $\mathbf{I}_{3x3}$ represents an identity matrix that has the dimensions 3x3.

$$\mathbf{A} = \begin{bmatrix} \mathbf{I}_{3x3} & T\mathbf{I}_{3x3} & \frac{1}{2}T^2\mathbf{I}_{3x3} & \frac{1}{6}T^6\mathbf{I}_{3x3} \\ \mathbf{0}_{3x3} & \mathbf{I}_{3x3} & T\mathbf{I}_{3x3} & \frac{1}{2}T^2\mathbf{I}_{3x3} \\ \mathbf{0}_{3x3} & \mathbf{0}_{3x3} & \mathbf{I}_{3x3} & T\mathbf{I}_{3x3} \\ \mathbf{0}_{3x3} & \mathbf{0}_{3x3} & \mathbf{0}_{3x3} & \mathbf{I}_{3x3} \end{bmatrix} \tag{6.4}$$

$\mathbf{0}_{3x3}$ represents a matrix of zeros with the dimensions of 3x3. The timestep, T, for this research is 1 second due to the GPS receiver having a 1 Hz update rate. Once going through the model, the estimates are multiplied by the $\mathbf{C}$ matrix (Eq. (6.5)) to develop the measurement estimates ($\hat{\vec{y}}$).

$$\mathbf{C} = \begin{bmatrix} \mathbf{I}_{3x3} & \mathbf{0}_{3x3} & \mathbf{0}_{3x3} & \mathbf{0}_{3x3} \\ \mathbf{0}_{3x3} & \mathbf{I}_{3x3} & \mathbf{0}_{3x3} & \mathbf{0}_{3x3} \end{bmatrix} \tag{6.5}$$

This estimate is then subtracted from the true measurements which are $\vec{y} = [\vec{r} \quad \vec{v}]^T$ from the receiver. The error between the measurements and the estimations is found by using this equation: $\vec{e} = \vec{y} - \hat{\vec{y}} = \vec{y} - \mathbf{C}\hat{\vec{x}}$. These are then multiplied by the gain matrix $\mathbf{L}$ which is developed using the poles in Figure 6.2. This can be seen here: $\dot{\hat{\vec{x}}} = \mathbf{A}\hat{\vec{x}} + \mathbf{L}(\vec{y} - \mathbf{C}\hat{\vec{x}})$.

Once the estimation of the total acceleration, the next stage was to estimate the ballistic coefficient which can be seen in the dotted line area of the Figure 6.1. The gravity and acceleration of the earth were calculated using the position and velocity vectors from the measurement vector ($\vec{y}$). These were then subtracted from the total estimated acceleration to obtain an estimate of the drag. Using the drag estimate, measurements of position and velocity, and Equation (6.3), a coefficient within 10% error was found using the truth data as measurements.

6.2.1 Tuning Gain Matrix

As a discrete system, these poles needed to be inside the unit circle to be asymptotically stable. As seen in Figure 6.2, two of the poles were chosen to be real numbers while the other two were complex conjugates. The poles chosen gave results within 10% of the true value when truth data was used in place of measurements. They were 0.8±0.5i, 0.3, and 0.85.

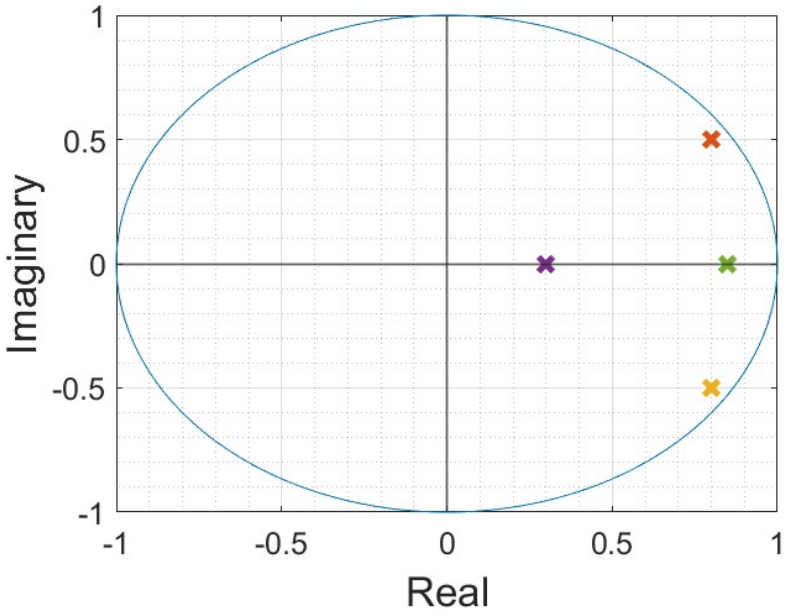

Figure 6.2: Pole Locations of L Matrix

Only four poles were chosen even though there were 12 states total. This is because it was assumed that each component was independent of each other as seen in Equation (6.4). Therefore, to choose the poles and develop the gain matrix, the one dimensional poles were found using the **A** and **C** matrix in Equations (6.6) and (6.7).

$$\mathbf{A_{1D}} = \begin{bmatrix} 1 & T & \frac{1}{2}T^2 & \frac{1}{6}T^3 \\ 0 & 1 & T & \frac{1}{2}T^2 \\ 0 & 0 & 1 & T \\ 0 & 0 & 0 & 1 \end{bmatrix} \tag{6.6}$$

$$\mathbf{C_{1D}} = \begin{bmatrix} 1 & 0 & 0 & 0 \\ 0 & 1 & 0 & 0 \end{bmatrix} \tag{6.7}$$

A four by two-dimensional $\vec{L}_{1D}$ matrix was found with gains seen in Equation (6.8) by using the poles from Figure 6.2. This was then duplicated into a three-dimensional $\mathbf{L}$ matrix with dimensions of 12 by 6 in Equation (6.9). Using this method allowed for easier tuning of the poles.

$$\mathbf{L_{1D}} = \begin{bmatrix} l_{11} & l_{12} \\ l_{21} & l_{22} \\ l_{31} & l_{32} \\ l_{41} & l_{42} \end{bmatrix} \tag{6.8}$$

$$\mathbf{L} = \begin{bmatrix} l_{11} & 0 & 0 & l_{12} & 0 & 0 \\ 0 & l_{11} & 0 & 0 & l_{12} & 0 \\ 0 & 0 & l_{11} & 0 & 0 & l_{12} \\ l_{21} & 0 & 0 & l_{22} & 0 & 0 \\ 0 & l_{21} & 0 & 0 & l_{22} & 0 \\ 0 & 0 & l_{21} & 0 & 0 & l_{22} \\ l_{31} & 0 & 0 & l_{32} & 0 & 0 \\ 0 & l_{31} & 0 & 0 & l_{32} & 0 \\ 0 & 0 & l_{31} & 0 & 0 & l_{32} \\ l_{41} & 0 & 0 & l_{42} & 0 & 0 \\ 0 & l_{41} & 0 & 0 & l_{42} & 0 \\ 0 & 0 & l_{41} & 0 & 0 & l_{42} \end{bmatrix} \tag{6.9}$$

6.3 Estimation Results

In simulation, the true ballistic coefficient for the Iridium data set was 0.050 m^2/kg which will be shown as a thick black line on all figures in this section. To exceed prior literature

work done on TLE data estimation, the ballistic coefficient estimation should have an error better than 14%. A comparison between the truth and Novatel measurements will be examined in this section. This data was taken over 24 hours to give enough time to develop a good estimate of the ballistic coefficient and to determine if any outliers were present.

The first results in Figure 6.3 shows the results of the estimation procedure when inputting the true position and velocity. There is obvious oscillation and this is thought to be due to the way the velocity is calculated in the Moore-Penrose inverse as one or two components approach zero. With the pole locations chosen, it can be observed that over the 24-hour period, the ballistic coefficient estimate is approaching a stable solution, if rather slowly. The mean of this estimation set seen by the thick red line was 0.0546 m^2/kg which falls within the 10% error bound requirement as the true coefficient is 0.0496 m^2/kg. It is assumed over time, that the ballistic coefficient would approach the mean value of the estimation meaning there is an estimation bias.

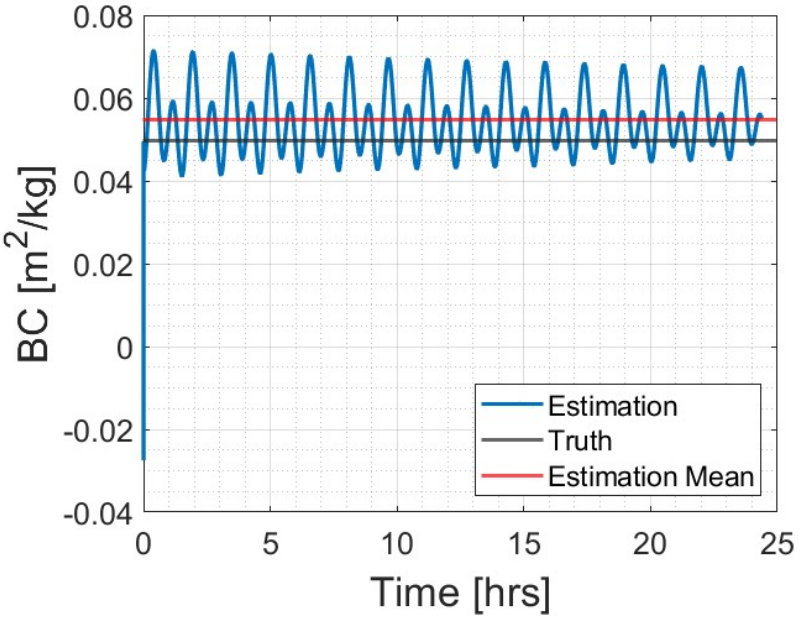

Figure 6.3: Estimation of the Ballistic Coefficient with Truth Data

The above test was run to ensure proper tuning of the gain matrix as well as to insure viability that the coefficient could be estimated in the absence of noise. Next, using the same poles as the truth data, the receiver measurements replaced the true data in the measurement vector. These measurements were discovered to have noise that was too large to

estimate the drag and subsequently the ballistic coefficient to a reasonable tolerance. Figure 6.4a shows the ballistic coefficient estimation from the furthest data point. The estimation at the beginning overshoots the truth by a large amount. The overshoot can be decreased using different pole amounts but often at the expense of the mean value meaning that in most cases with this data set, as the overshoot decreased, the mean (bias) increased. Upon closer examination of Figure 6.4b, it can be seen how noisy the estimation is. The mean across the whole data set is 14.328 m^2/kg which falls well outside the 10% error range. Through this analysis, it is determined that the measurement noise is too large to be able to estimate the ballistic coefficient accurately.

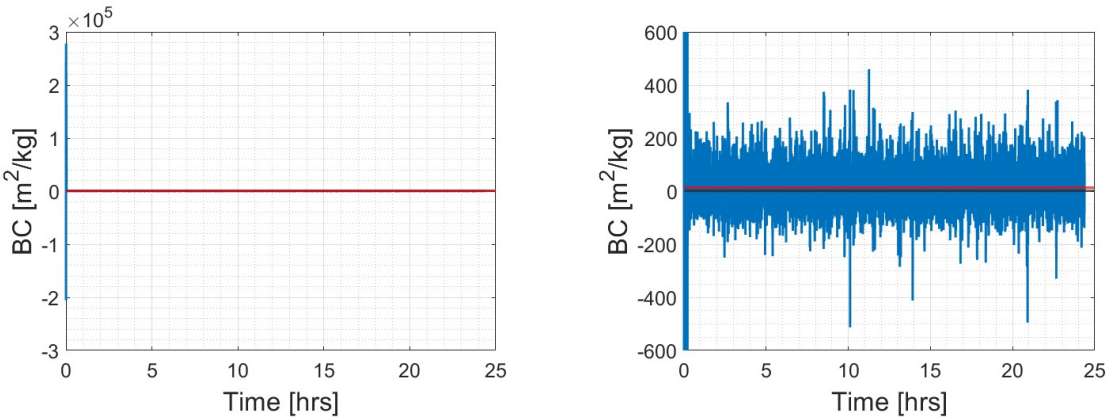

(a) Zoomed Out (b) Zoomed In

Figure 6.4: Estimation of Ballistic Coefficient with Receiver Data

6.4 Atmospheric Drag Noise

Because acceleration is not a measurement, the atmospheric drag must be estimated. The process to estimate this is explained above in Figure 6.1. A study on the estimation of the drag was performed because of the amount of noise observed on the ballistic coefficient estimation. The true atmospheric drag using the constant density value and the true ballistic coefficient was determined using the drag equation (Eq. (1.1)). This was then compared to the estimated drag during the ballistic coefficient estimation process. When estimating the ballistic coefficient, it is important to determine the amount of noise that is on the atmospheric drag estimation. This noise will translate onto the noise of the coefficient estimation as seen from the results in Section 6.3.

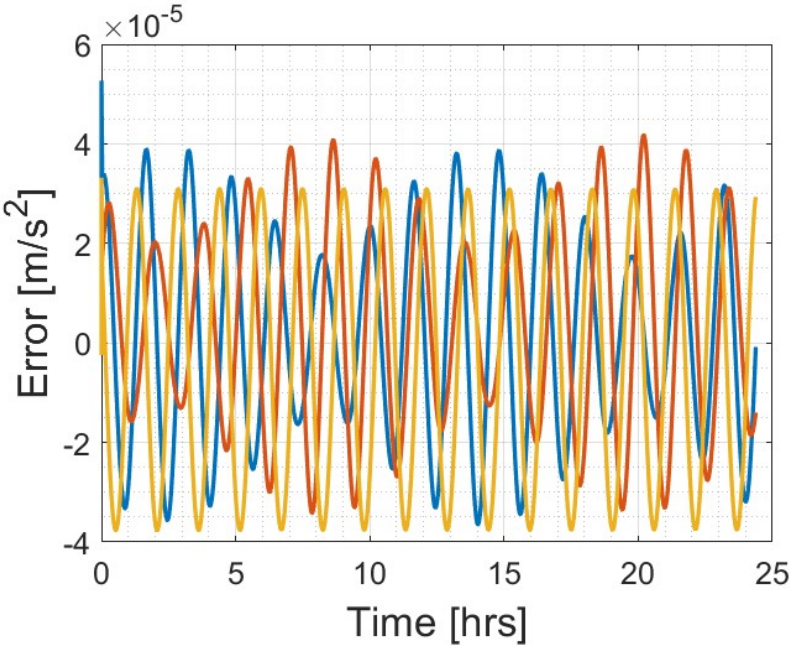

Figure 6.5: Atmospheric Drag Estimation Error of Truth

Figure 6.5 shows the error from the calculated true atmospheric drag and the estimated atmospheric drag with the true measurements. This figure shows that the error in the difference is relatively small. This is what leads to the estimation within 10% of the true ballistic coefficient. While the error is small, there is still some error that could be effecting the drag estimation. The z component of the acceleration error is largely uniform in appearance with the x and y components oscillating in a repeating pattern. This is most likely due to some unmodeled force in the Earth's rotation or a small error in one of the variables.

Figure 6.6 now shows the error when using the noisy measurements. Both the position and velocity measurements are used when estimating the atmospheric drag. This causes an error magnitude forty times larger than the error when using the true measurements. The difference in this drag error is what likely leads to the large difference in estimating the ballistic coefficient. While this error might seem small when comparing to the total acceleration values, this size error on the atmospheric drag (which is around the range of 1e-5) can cause significant error in positioning propagation.

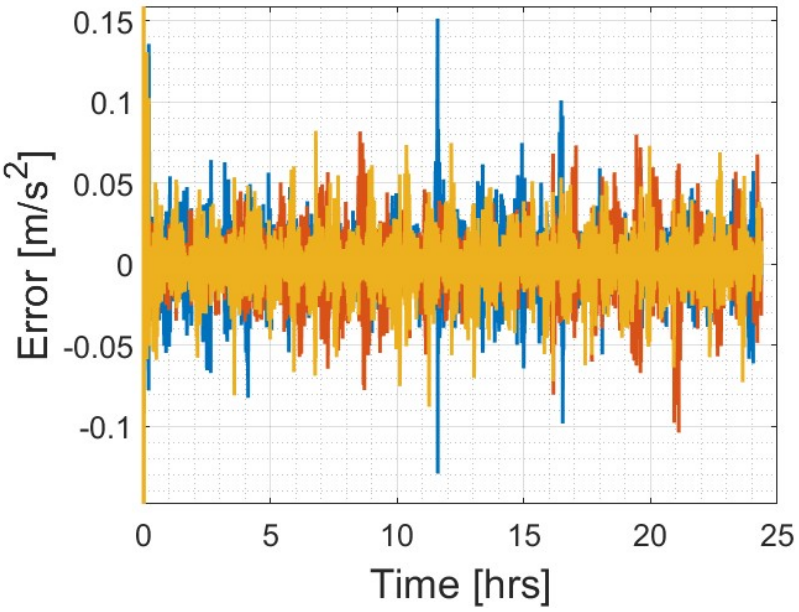

Figure 6.6: Atmospheric Drag Estimation Error of Novatel Data

Figure 6.7 - 6.8b will highlight the error norm of the ballistic coefficient to showcase the overall difference in the error between the truth estimation and using the measurements. Figure 6.7 shows the error norm of the truth measurements. While not completely zero, the error oscillates around the 3.5e-5 amount. The small oscillation around the 15-hour mark most likely shows when the error for each component is similar to the error in the other components.

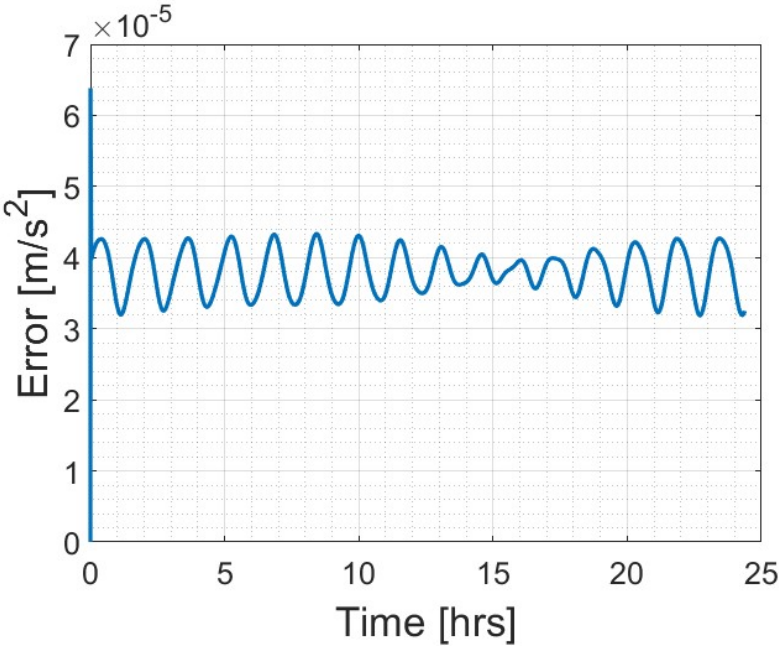

Figure 6.7: Atmospheric Drag Estimation Error Norm of Truth

The error for the Novatel data is shown in Figure 6.8a and Figure 6.8b. Figure 6.8a is zoomed out to show the magnitude of that initial error caused by the Novatel not obtaining a good positioning solution. Figure 6.8b is zoomed in to highlight the magnitude of error across the entire estimation process. There are large peaks in the data and overall the data does not follow a consistent pattern.

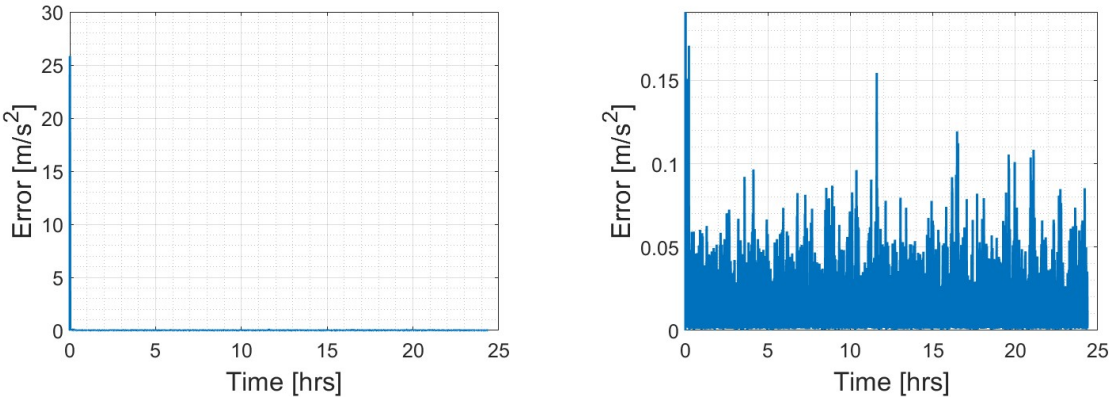

(a) Zoomed Out

(b) Zoomed In

Figure 6.8: Atmospheric Drag Estimation Error Norm of Receiver Data

In conclusion, to display how the noise on the atmospheric drag influences the ballistic coefficient estimation the error is show side by side in Figure 6.9. From this comparison,

the pattern in the error of the atmospheric drag and the ballistic coefficient are very similar. This leads to the overall conclusion that if there is too much noise on the measurements, then it is not possible to estimate the ballistic coefficient accurately.

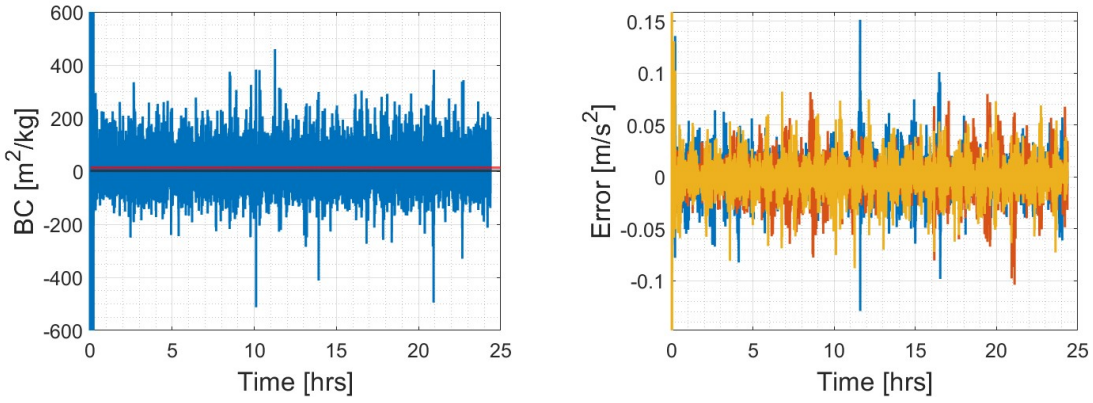

(a) Ballistic Coefficient

(b) Atmospheric Drag

Figure 6.9: Estimation Comparison of Novatel Data

Chapter 7

Error Influence of Ballistic Coefficient on Orbit Determination

7.1 Background

The effect of the ballistic coefficient error on the propagation of position and velocity was studied. Over 12-hours of simulated data was used. Much like the process in Chapter 5 the orbit determination portion was run using an EKF to simulate how on-board orbit determination is performed. Next, a GPS measurement outage was simulated and the satellite's position was propagated forward in time for 10 minutes. After 10 minutes, the resulting propagation error was calculated and then compared against each ballistic coefficient.

This section will show that the ballistic coefficient has a small affect on the overall error of the orbit. A normal ballistic coefficient is on the order of magnitude of 1e-2 which is below the noise floor of the GPS measurements. Using truth data, the ballistic coefficient can be measured to within 10% of the true value. As more noise is added to the data, as seen in Section 6.3 it becomes increasingly more difficult to determine the actual coefficient. This section will show that because the ballistic coefficient error is magnitudes lower than other forces, it does not have a significant effect on the end propagation result. Once the noise of the ballistic coefficient increases to allow for the drag to have a significant impact on the propagation, then the error increases significantly.

The results are derived following the technique specified in Section 6.2. For each run, the ballistic coefficient had error added to the value during the propagation. The final position error was compared between runs to determine the affect of the ballistic coefficient.

The same was also repeated with velocity to determine how the ballistic coefficient affects the integration error.

7.2 Propagation Error Results

Figure 7.1 shows the position error norm and Figure 7.2 shows the velocity error norm at the end of the 10-minute propagation for the Monte Carlo simulations. As the error was added to the ballistic coefficient to the same orbit, the pattern for each end position and velocity follows roughly the same path with slightly different values. As it will be shown later in this section, the variation of the error is very small and cannot be seen in these figures.

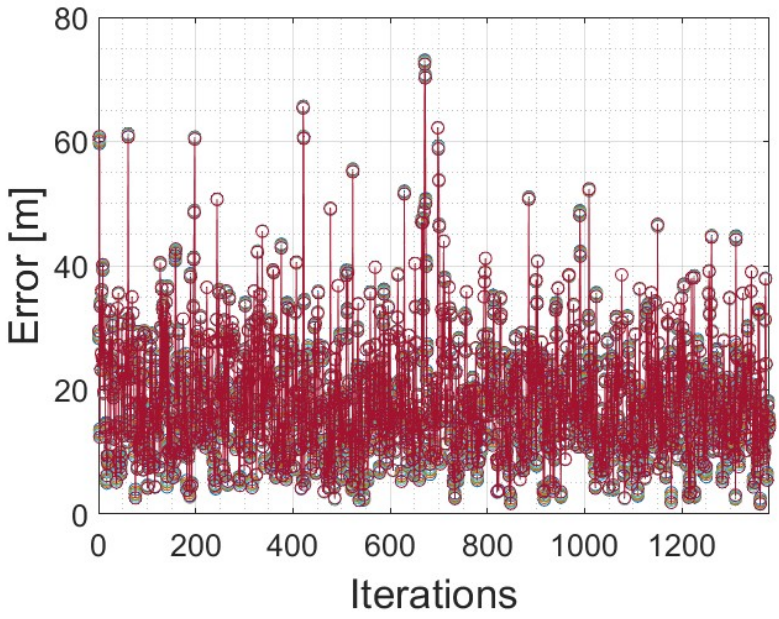

Figure 7.1: Position Error Norm for $\pm 100\%$ Ballistic Coefficient Error

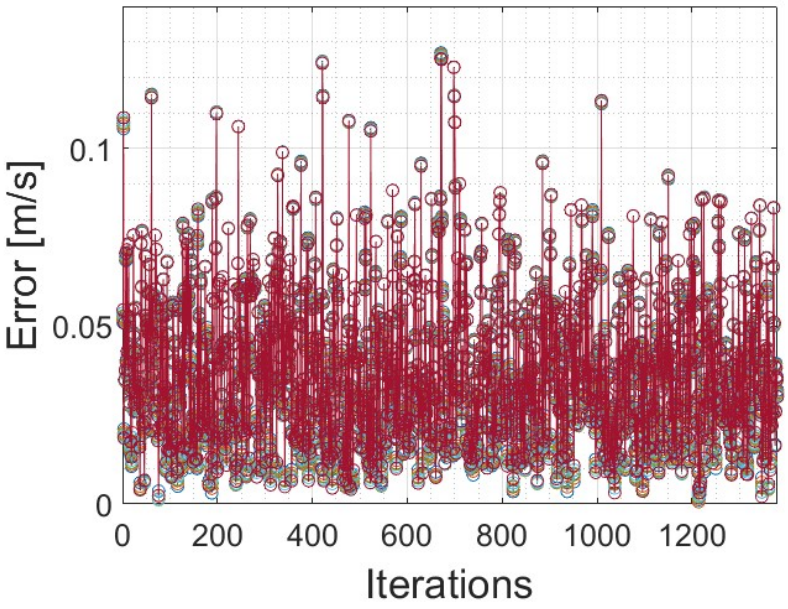

Figure 7.2: Velocity Error Norm for $\pm 100\%$ Ballistic Coefficient Error

To analyze the error, the propagation results without any ballistic coefficient error was separated. This is what Figure 7.3 and 7.4 shows. As Figure 7.3 shows, the majority of the error is below 40 meters of error at the end of 10 minutes. These two figures show a correlation between the final position error and the final velocity error. The initial velocity and acceleration error is large which causes the errors to be extrapolated over time thereby effecting the position solution.

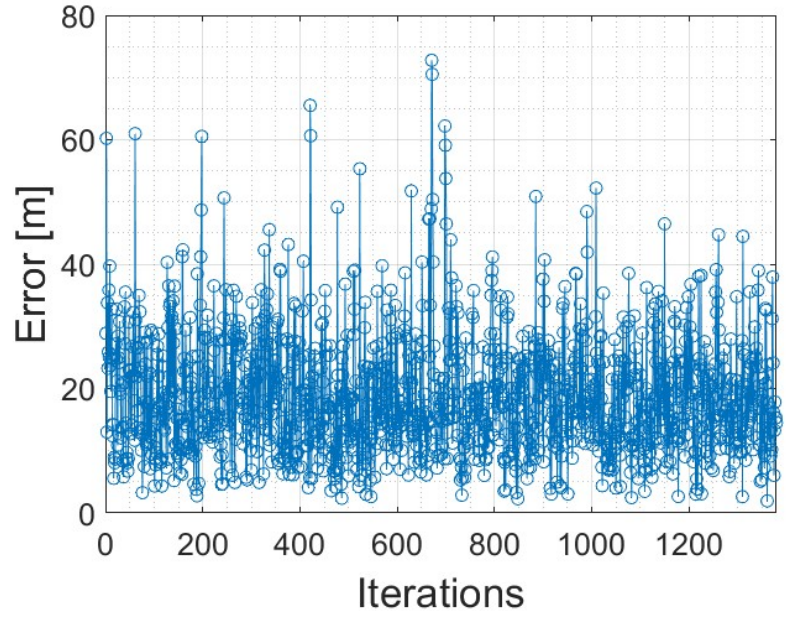

Figure 7.3: Monte Carlo Simulation With No Error

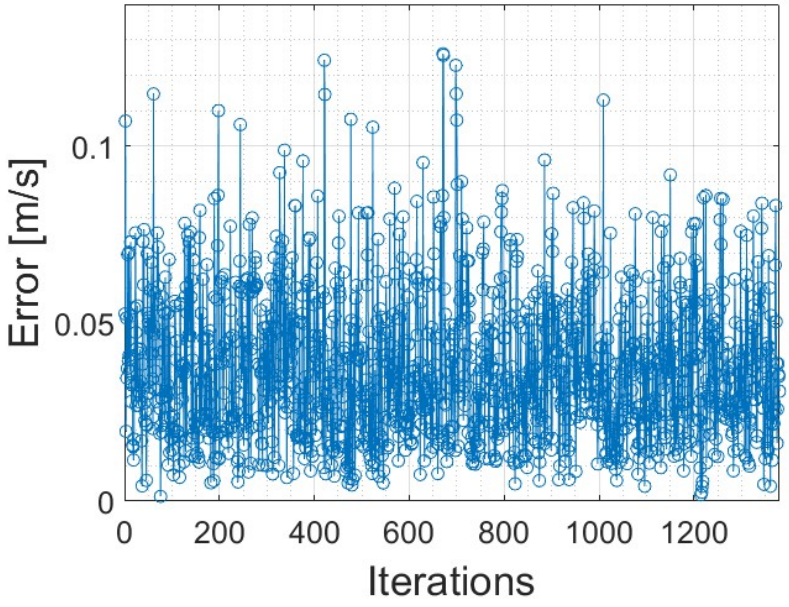

Figure 7.4: Monte Carlo Simulation With No Error

The next figures will show the initial position and velocity error. Acceleration error was not an output of the Runge-Kutta scheme. Unlike Figure 7.3, Figure 7.5 has a sinusoidal pattern which can be attributed to the error output from the EKF. There is likely an error in the Novatel measurements that is causing this error. Figure 7.6 shows that the initial velocity error under 0.1 meters per second.

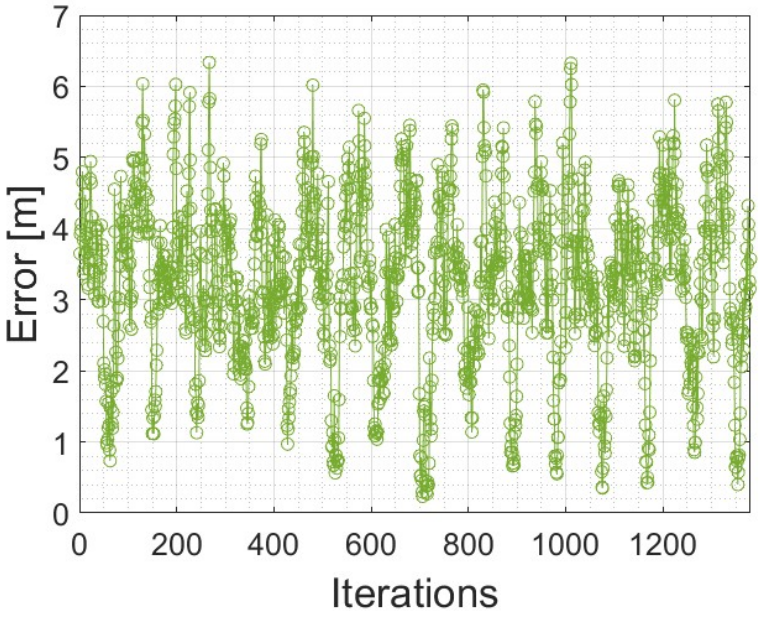

Figure 7.5: Initial Position Error

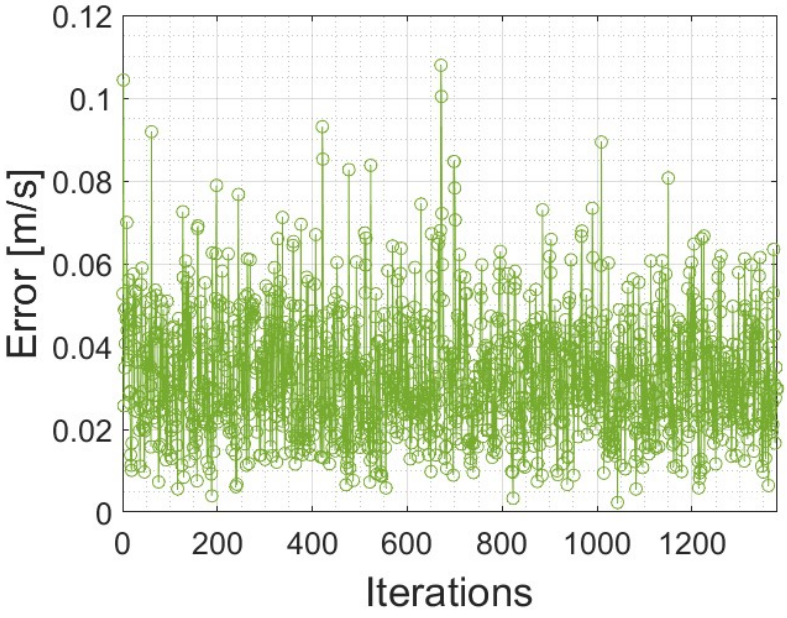

Figure 7.6: Initial Velocity Error

Looking at Figure 7.7 shows the mean propagation error for $\pm$ 100% of error added to the ballistic coefficient. The true ballistic coefficient for this data set is 0.0496 m^2/kg and has 19 meters of error. Between -100% and 100%, the error only changes by 0.3851 meters. Figure 7.8 includes values up to 1200 % error on the ballistic coefficient. These results show that the error in propagation, at this altitude and 10 minute duration, is not

largely influenced by atmospheric drag. Once the error in the atmospheric drag estimate outweighs the noise of the GPS measurements, the propagation error becomes significantly larger which can be seen in Figure 7.8.

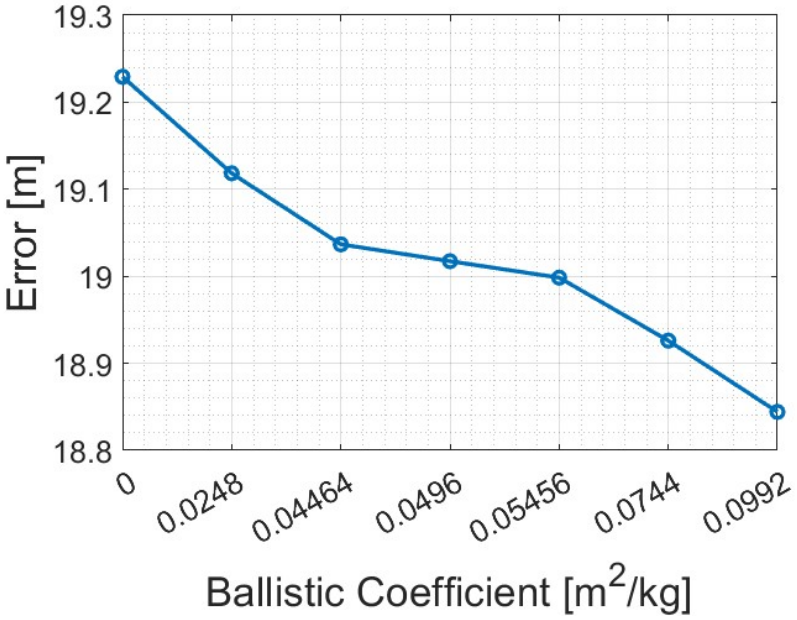

Figure 7.7: Mean Position Error of Propagation

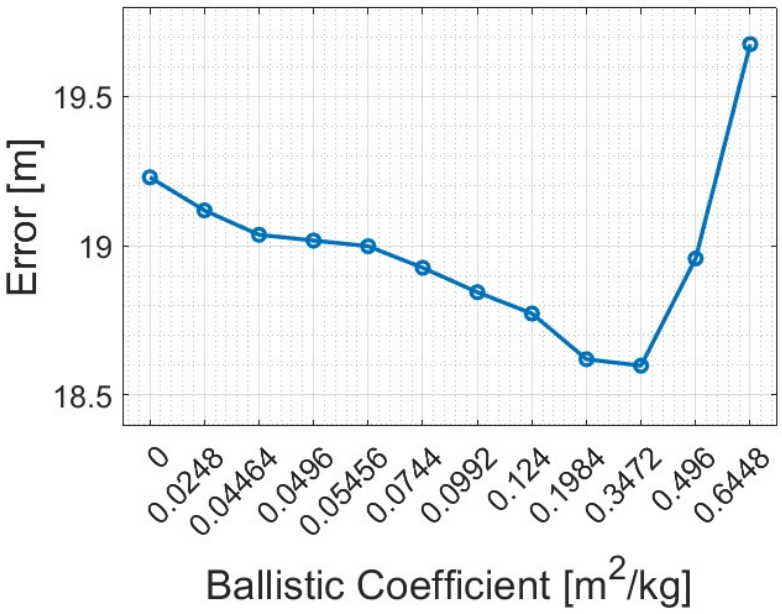

Figure 7.8: Mean Position Error of Propagation (All Values)

Now to view the error in velocity without the error bars to better show the velocity error between each different ballistic coefficient. The velocity error between the largest error and the smallest error is only 3.633e-4 meters per second.

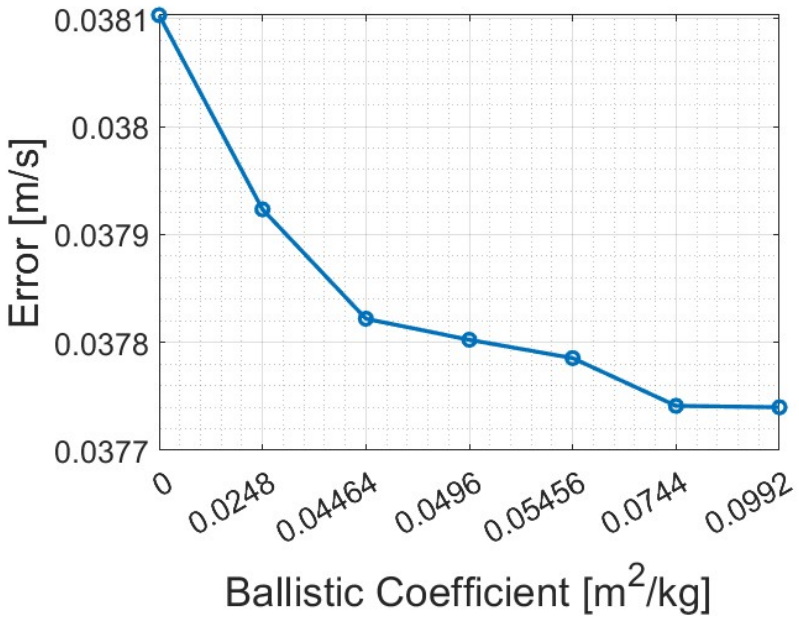

Figure 7.9: Mean Velocity Error of Propagation (100%)

These results show that the error in propagation, at this altitude, is not largely influenced by atmospheric drag. Once the error in the atmospheric drag error outweighs the noise of the GPS measurements, the propagation error becomes significantly larger.

7.3 Statistical Distribution of Propagation Error

Below are the two histograms approximating the probability density functions (PDF) for position and velocity. Figure 7.10 shows the position error PDF curve and Figure 7.11 shows the velocity PDF. The PDF of random variables shows the chance that the value will fall within a certain value range. For a Gaussian normal distribution, the graph would be a bell curve with the mean and median being at the same point. The figures below are right skewed graphs meaning that the median of the data set is located towards the smaller values. This means that this data set has a higher probability of lower error occurring after 10 minutes of propagation.

For example, the position data in Figure 7.10 has a larger chance of the error being around 15 meters at the end of the propagation than if the data had no skew. If the data was symmetric on the range zero to 30 meters, the highest probability of error would be twice what it is now at 35 meters. The same can be seen in Figure 7.11 with the highest probability of the data occurring towards the lower ranges of error.

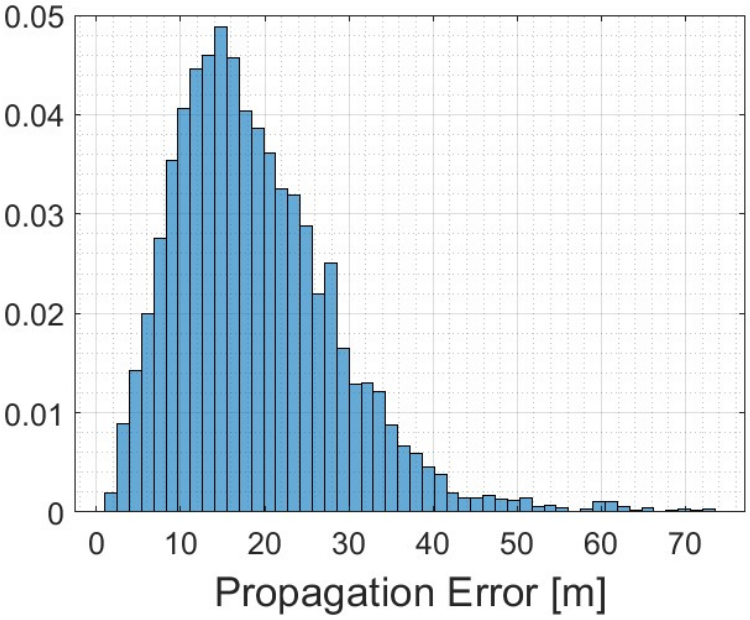

Figure 7.10: PDF Distribution of Position Propagation Error After 10 minutes

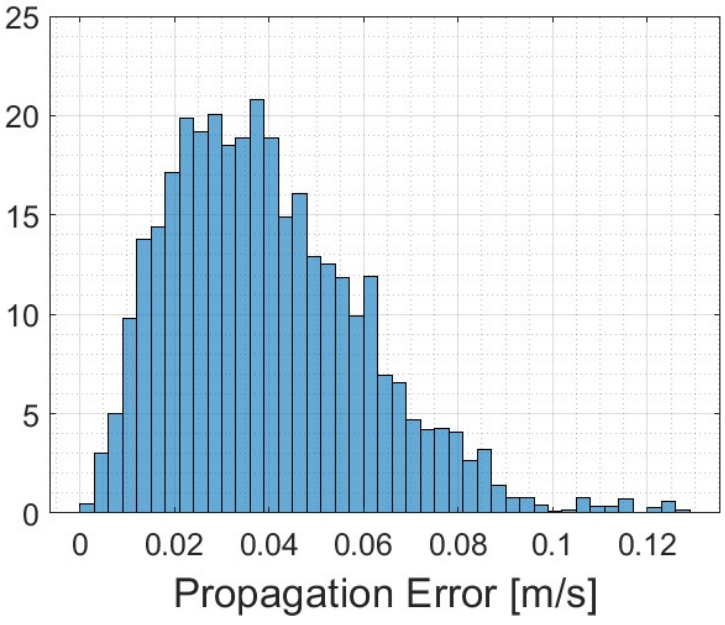

Figure 7.11: PDF Distribution of Velocity Propagation Error After 10 minutes

The following figures will show the CDF of the data. This shows the likelihood of the data being at or below a value a certain percentage of the time. Figure 7.12 shows that for 90% of the time, the error stay below 35 meters of error. The same can be applied to Figure 7.13 as the velocity error stays below 0.09 meters per second for 90% of the time. These graphs are useful for visualizing the error impact of the data sets.

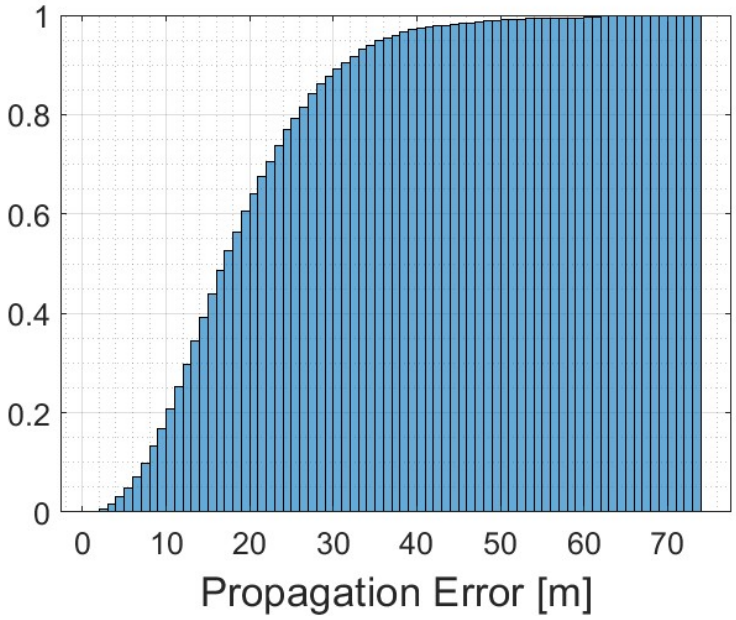

Figure 7.12: CDF Distribution of Position Propagation Error After 10 minutes

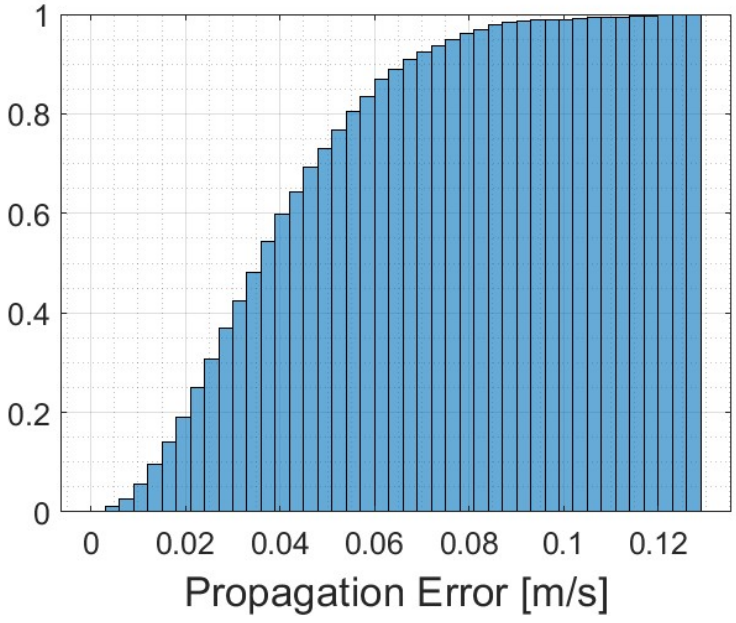

Figure 7.13: CDF Distribution of Velocity Propagation Error After 10 minutes

Chapter 8

Simulation Study

8.1 Introduction

A satellite orbit was simulated to study the effects different ballistic coefficients had under known conditions. As with the Spirent satellite orbit, the same acceleration model was used to develop the position and velocity vectors. Unlike the Spirent satellite, these were the only accelerations that were included in the model. It is not known entirely how the Spirent simulator produced their acceleration model so the best fit model was found. This allowed un-modeled forces to be included when trying to estimate the ballistic coefficient.

For the simulation, a satellite orbit was simulated in Matlab by using ode45 and the acceleration model that was developed for this thesis. The outputs from the simulation was position and velocity vectors over a 24 hour time span. GPS measurements were created by taking the taking the simulation output and adding normally distributed random noise. The standard deviation for this noise is seen in Table 8.1.

	Position [m]	Velocity [m/s]
Test 1	5e-1	1e-2
Test 2	5e-2	1e-3
Test 3	5e-3	1e-4
Test 4	5e-4	1e-5
Test 5	5e-5	1e-6
Test 6	5e-6	1e-7
Test 7	5e-7	1e-8
Test 8	5e-8	1e-9
Test 9	5e-9	1e-10
Test 10	5e-10	1e-11
Test 11	5e-11	1e-12

Table 8.1: Standard Deviation of Measurements

These standard deviations were chosen arbitrarily but tried to mimic the same standard deviations as actual GPS measurements. The simulated satellite position and velocity vectors and the simulated GPS measurements were then used as the input to the process described in Section 6.2. The results will show in this section the amount of standard deviation that needs to be allowed in the measurements before a considerable affect of the ballistic coefficient estimation is shown.

8.2 Test Results

The results shown will comprise the test results from each of the standard deviations in Table 8.1. First, the position in the X-direction will be shown from each of the tests and then all directions will be compared for the smallest standard deviations and the largest. The same will also be done for velocity showing only the X-direction and then a comparison of all three. A graph on a logarithmic scale will be shown for each of the positions that shows the impact that the measurement noise has on the ballistic coefficient when compared.

From Figures 8.4a - 8.5e, the progression of how the ballistic coefficient influences the satellite's final position error is shown. Between the first three values of standard deviation, the graphs change largely in value and more of an effect of the error is seen. Once the standard deviation of the measurements passes 5e-4 m, the impact of the error on the ballistic coefficient can be seen more. The more error that is added to the ballistic coefficient when the measurements have a standard deviation of 5e-4 or lower impacts the height and shape of the histogram.

As the standard deviation lowers, the graphs become more non-Gaussian, especially as the ballistic coefficient error increases. This type of curve represented in the data is called a bimodal distribution. When this occurs, the maximum value no longer is zero, but instead is at either of the peaks. The data is now being classified more into two groups, one negative and one positive error.

This change in Gaussian curves can really be seen in Figures 8.2 and Figures 8.3. The Z-direction graph changes drastically between a standard deviation of 5e-1 meters and 5e-11 meters. The graph has become significantly nonlinear and has separated into a multimodal distribution. This is likely due to the Z direction not having a Coriolis acceleration term included in the equation.

Comparing all the X position standard deviations on one graph as in Figure 8.1 shows the effect a smaller standard deviation on the measurements has on the end propagation error. Figure 8.1 displays only the truth values with not error on the ballistic coefficient. As the measurement standard deviations approach 5e-4, they decrease in error range. After 5e-4 sigma, the standard deviations do not change drastically as they did with the first four standard deviations. The difference from one deviation to the next is so miniscule that it cannot be observed.

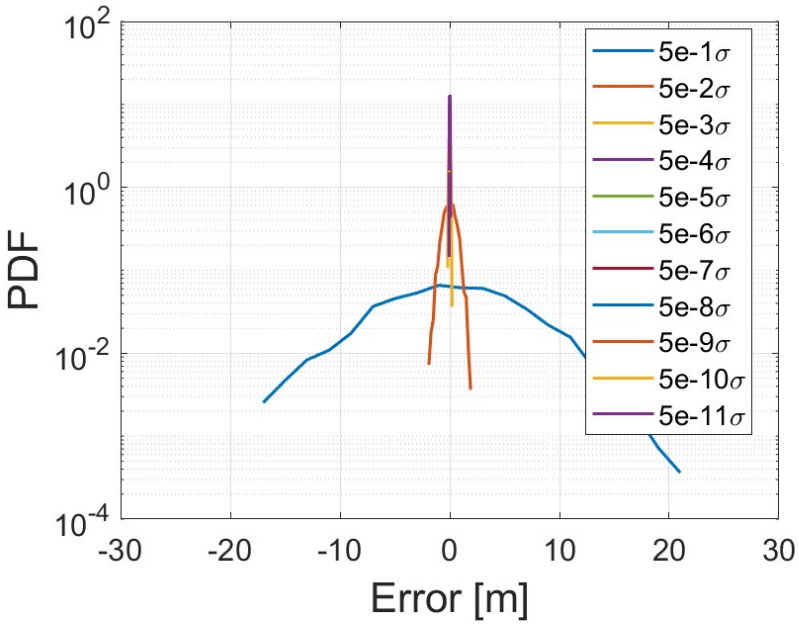

Figure 8.1

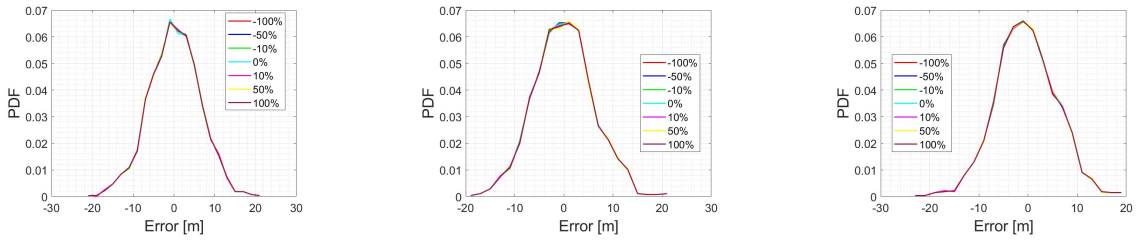

(a) X direction (b) Y direction (c) Z direction

Figure 8.2: Iridium Standard Deviation of 5e-1 [m] for Position

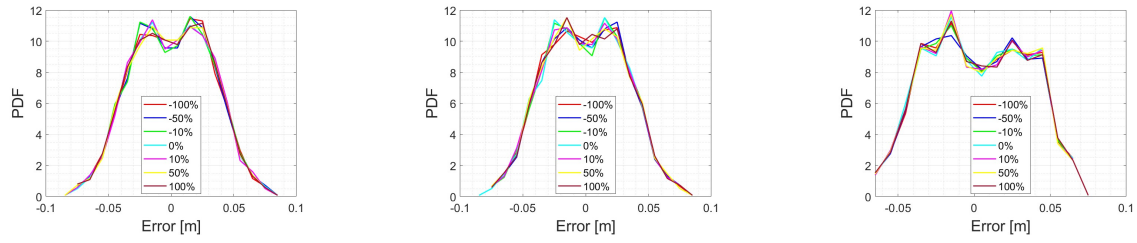

(a) X direction (b) Y direction (c) Z direction

Figure 8.3: Iridium Standard Deviation of 5e-11 [m] for Position

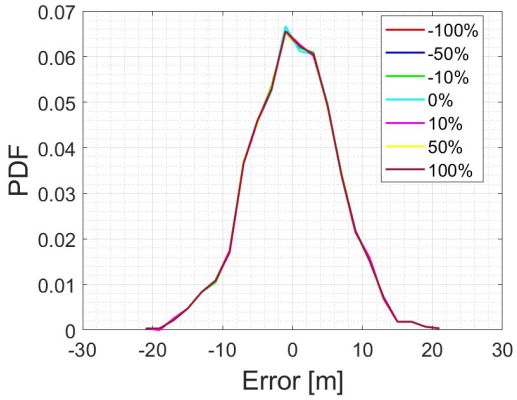

(a) Standard Deviation: 5e-1 [m]

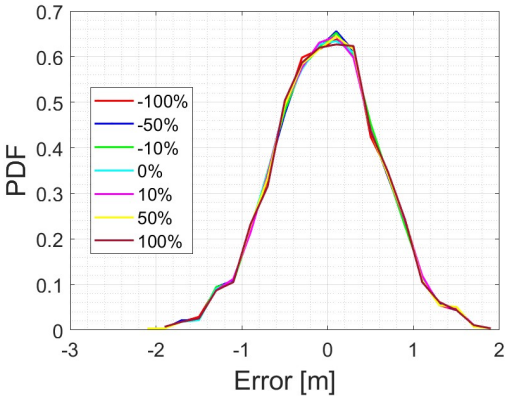

(b) Standard Deviation: 5e-2 [m]

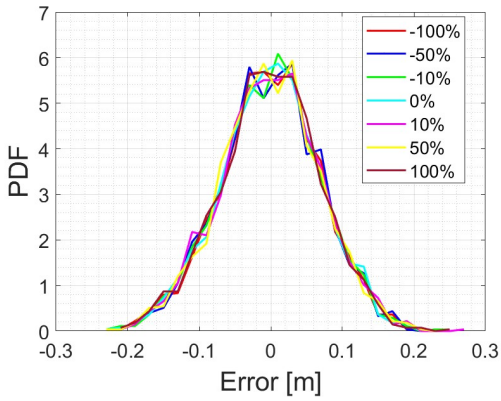

(c) Standard Deviation: 5e-3 [m]

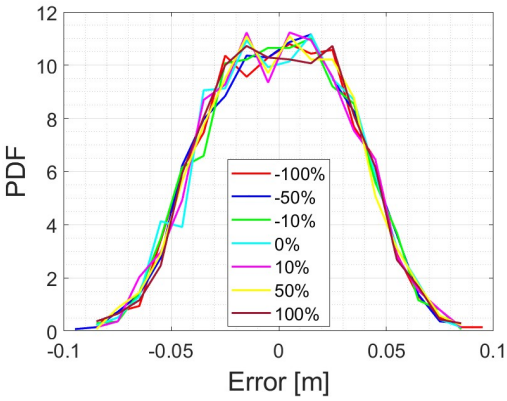

(d) Standard Deviation: 5e-4 [m]

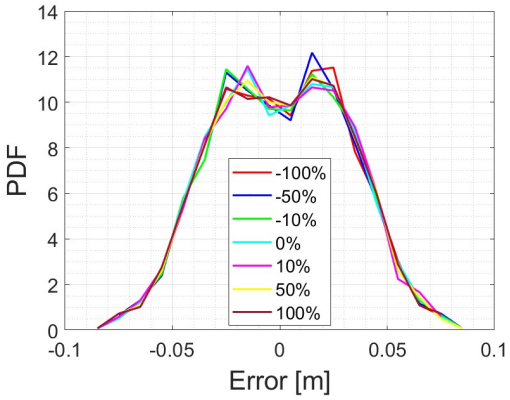

(e) Standard Deviation: 5e-5 [m]

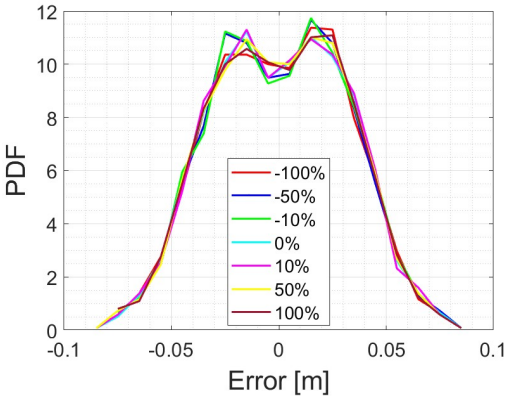

(f) Standard Deviation: 5e-6 [m]

Figure 8.4: Iridium X Position Error With Different Measurement Noise Values (Part 1)

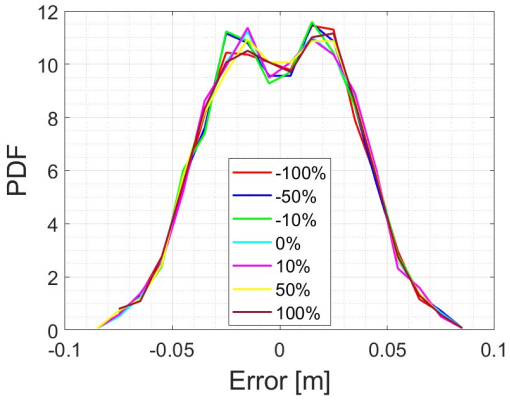

(a) Standard Deviation: 5e-7 [m]

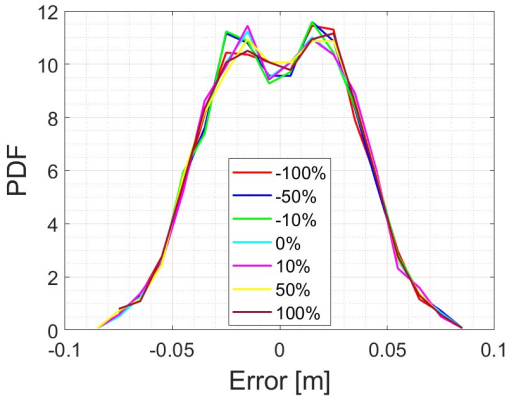

(b) Standard Deviation: 5e-8 [m]

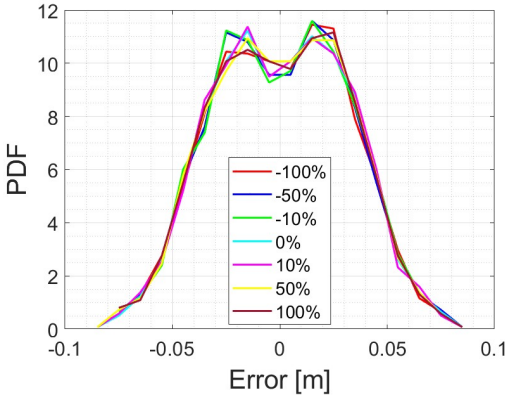

(c) Standard Deviation: 5e-9 [m]

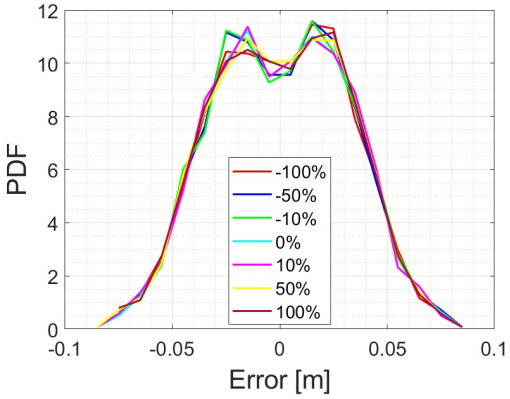

(d) Standard Deviation: 5e-10 [m]

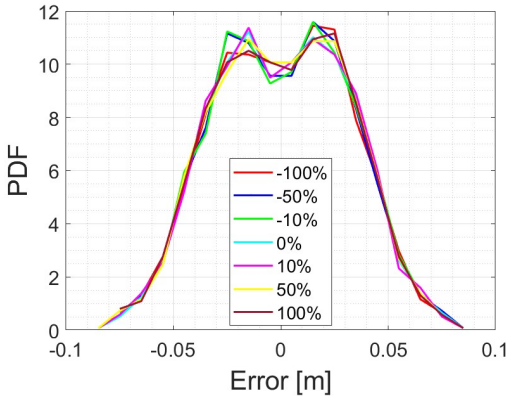

(e) Standard Deviation: 5e-11 [m]

Figure 8.5: Iridium X Position Error With Different Measurement Noise Values (Part 2)

Much like the position, the velocity error also becomes bimodal. This happens much quicker at a standard deviation of 5e-2 as seen in Figure 8.9a. As with position error, the change becomes non-existent between the standard deviation values of 5e-5 to 5e-11. At these measurement standard deviations, the values are so close to truth that there is not much error during estimation to correct.

Comparing the standard deviations of 5e-1 meters to 5e-11 meters between the three directions in Figures 8.7 and 8.8. Not much of an effect due to ballistic coefficient error can be seen in Figure 8.7. This is not the case in Figure 8.8 as a visible change in error distribution can be seen between each of the different ballistic coefficients.

Finally, all the ballistic coefficient values for the X direction velocity were compared on a logarithmic scale in Figure 8.6. Same as with position, error difference cannot be seen after the standard deviation of 5e-4 sigma. This leads to two conclusions: (1) That beyond 5e-4 standard deviation, the difference between truth and measurements is so miniscule that any error between them becomes unobservable to the filter, (2) For the ballistic coefficient error effect to be seen, the error on the measurements must be at a standard deviation of 5e-3 or lower, preferably smaller than 5e-4.

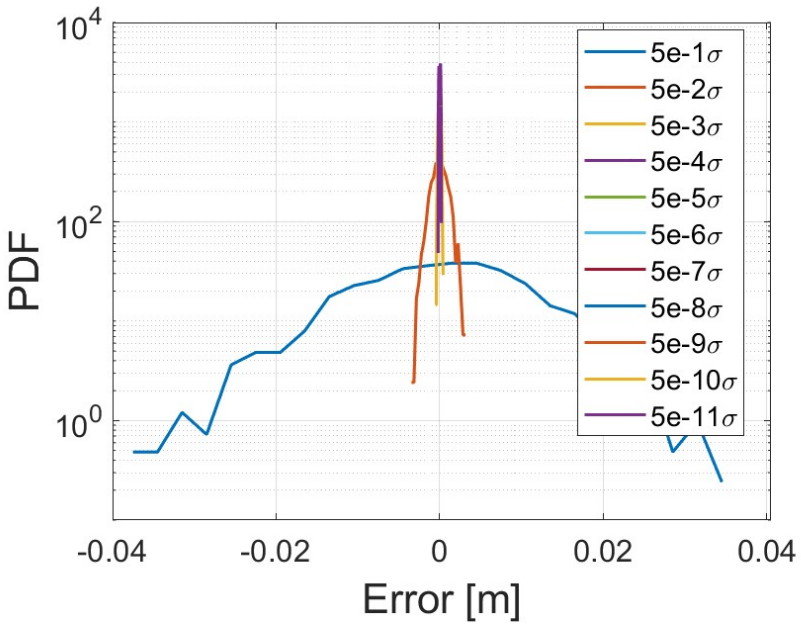

Figure 8.6: All Standard Deviations For Truth Velocity Data

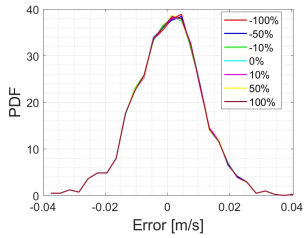

(a) X direction

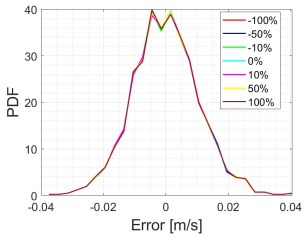

(b) Y direction

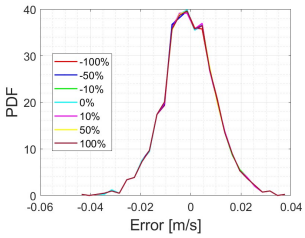

(c) Z direction

Figure 8.7: Iridium Standard Deviation of 5e-1 [m/s] for Velocity

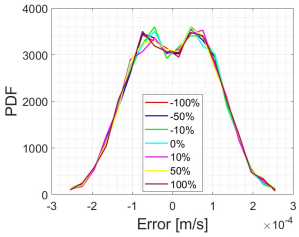

(a) X direction

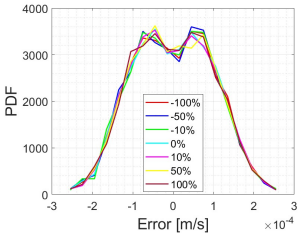

(b) Y direction

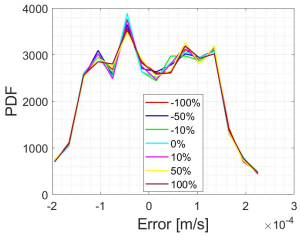

(c) Z direction

Figure 8.8: Iridium Standard Deviation of 5e-11 [m/s] for Velocity

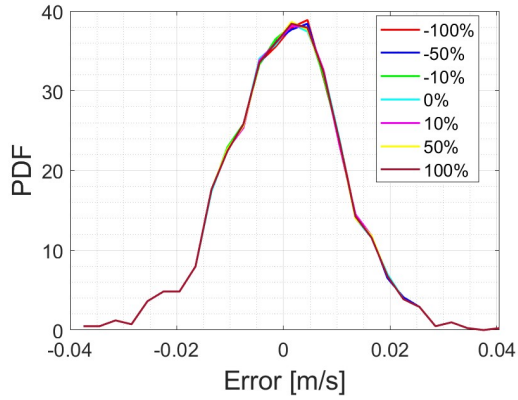

(a) Standard Deviation: 5e-1 [m/s]

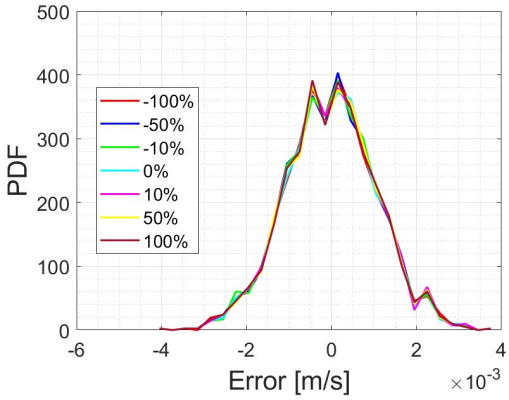

(b) Standard Deviation: 5e-2 [m/s]

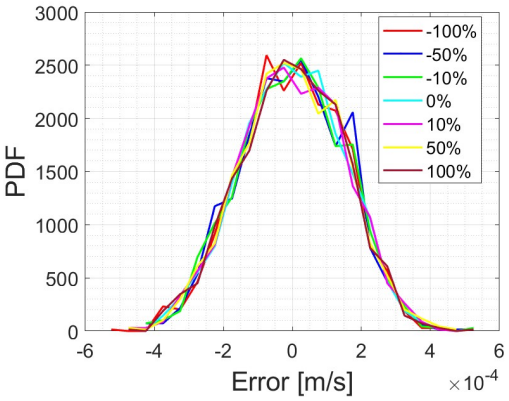

(c) Standard Deviation: 5e-3 [m/s]

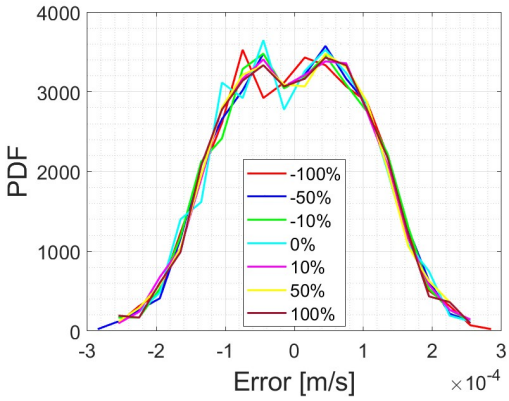

(d) Standard Deviation: 5e-4 [m/s]

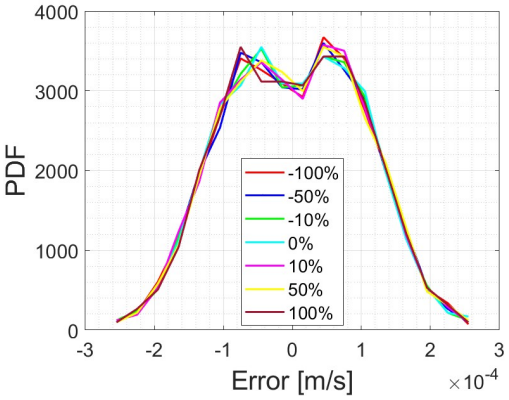

(e) Standard Deviation: 5e-5 [m/s]

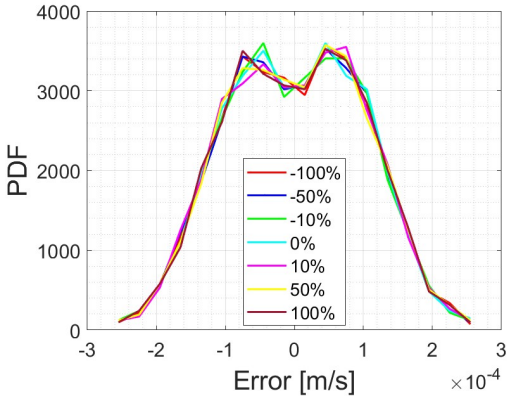

(f) Standard Deviation: 5e-6 [m/s]

Figure 8.9: Iridium X Velocity Error With Different Measurement Noise Values (Part 1)

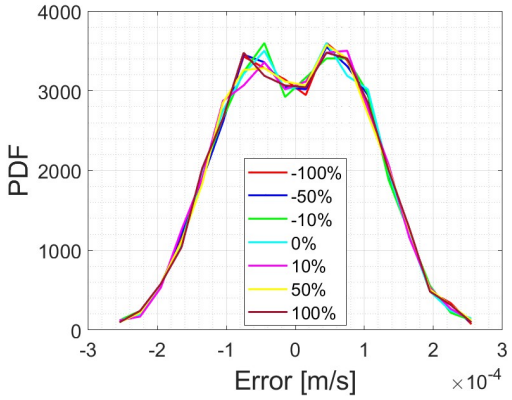

(a) Standard Deviation: 5e-7 [m/s]

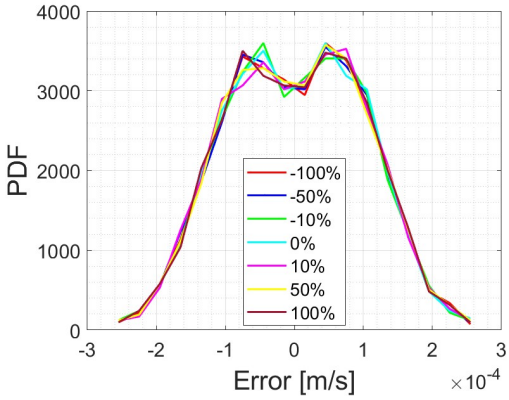

(b) Standard Deviation: 5e-8 [m/s]

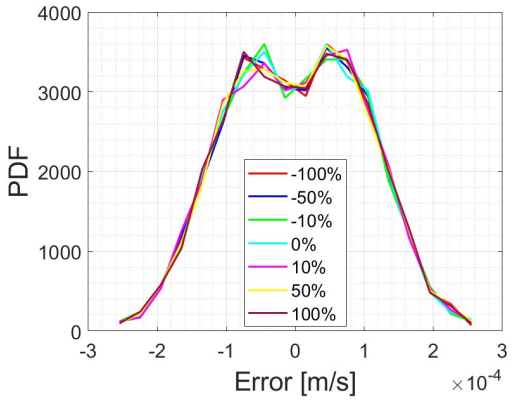

(c) Standard Deviation: 5e-9 [m/s]

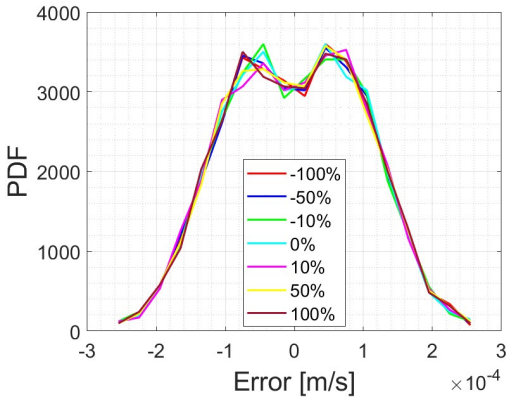

(d) Standard Deviation: 5e-10 [m/s]

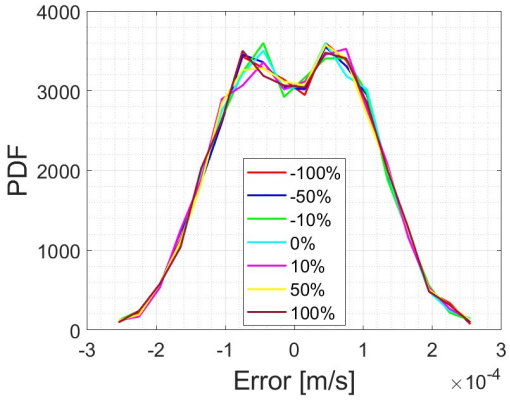

(e) Standard Deviation: 5e-11 [m/s]

Figure 8.10: Iridium X Velocity Error With Different Measurement Noise Values (Part 2)

Chapter 9

Receiver Position Error Due to Satellite Error

9.1 Introduction

To determine how the error in the satellite position calculation affects the receiver positioning solution, a receiver positioning algorithm was created. This algorithm can be seen in Figure 9.1 showing the process used to determine the final estimated receiver position. The tolerance was set arbitrarily to 0.01 and no increase in accuracy was observed when the tolerance was increased.

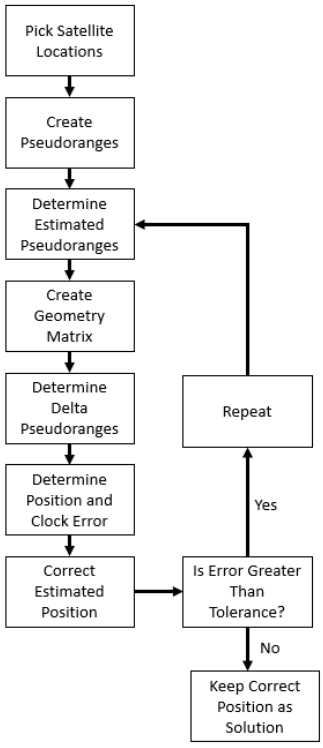

Figure 9.1: Receiver Positioning Algorithm

First, 4 satellite positions and a receiver position was picked somewhere on Earth. To stay consistent with the research done in this thesis, the satellite's altitude was picked for the range to be around 400 kilometers. The longitude, latitude, and altitude (LLA) positions of each satellite and the GPS receiver can be seen in Table 9.1. A skyplot of the satellites in view of the receiver is depicted in Figure 9.2. The receiver position here was assumed a perfectly known clock as well to help simplify the solution and because there was no access to clock data during research.

Name	Latitude [deg]	Longitude [deg]	Altitude [km]
Satellite 1	26.9751	37.9535	300
Satellite 2	29.5414	44.7771	300
Satellite 3	30.8865	39.4907	300
GPS Receiver	28.1029	43.3941	0.6

Table 9.1: Satellite and Receiver Position

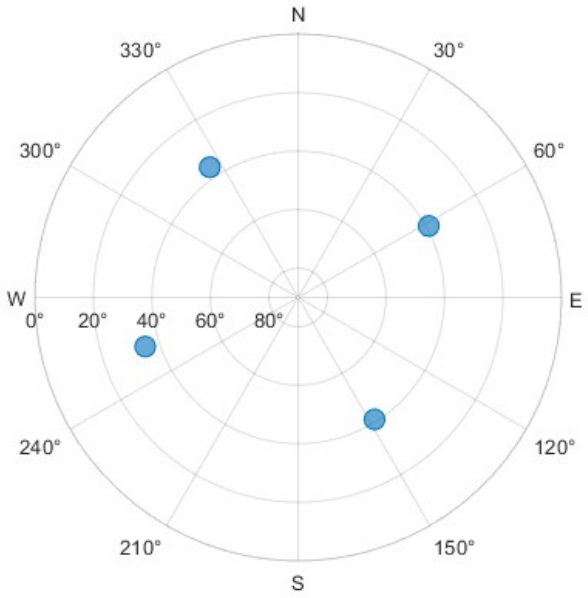

Figure 9.2: Sky Plot

To determine how the ballistic coefficient error effects the satellite error, error between -70 meters and 70 meters was added to each of the satellites during an iteration to create

new positions (r' = [x', y', z']). After this, pseudoranges were created by taking the new positions and adding error with standard deviation of 0.5 to it which can be seen in Equation 9.1.

$$\rho_k = |r'| + 0.5\nu \tag{9.1}$$

After the pseudoranges were created, the estimated pseudorange ($\delta\rho$) and the geometry matrix (G) were created. The estimated pseudorange can be found in Equation 9.2 where x, y, and z are the previously estimated receiver values. The geometry matrix can only be found after the estimated pseudorange is calculated and this can be seen in Equation 9.3. To find the estimated error between the receiver and the estimate, the equation $\delta r = (G^T G)^{-1} G^T \delta\rho$. These errors were used to then correct the receiver position estimate by $r = r_k + \delta r$. This process was then run through a 1000 run Monte Carlo for each satellite error between -70 and 70 meters.

$$\hat{\rho}_k = \sqrt{(sat'_x - x_k)^2 + (sat'_y - y_k)^2 + (sat'_z - z_k)^2} \tag{9.2}$$

$$G = \begin{bmatrix} -(sat'_x - x)/r & -(sat'_y - y)/r & -(sat'_z - z)/r \end{bmatrix} \tag{9.3}$$

9.2 Results

The Position Dilution of Precision (PDOP) is a measurement of the quality of the receiver-satellite geometry. The smaller the PDOP value, the better the satellite geometry used for positioning. Ideally, the PDOP would be below 1 but anywhere from 1 to 5 is considered a reliable PDOP value. Figure 9.3 shows how the PDOP changes with the satellite error. At -70 meters, the satellites are -70 meters further from the receiver value while adding a positive 70 meters of error brings the satellites more overhead allowing for a larger PDOP. For all satellite errors, the PDOP stayed below 1.41 and only fluctuated 0.0004 meters. The

PDOP increases because as all the satellites move to a more overhead value, it allows for less diversity in satellite positions.

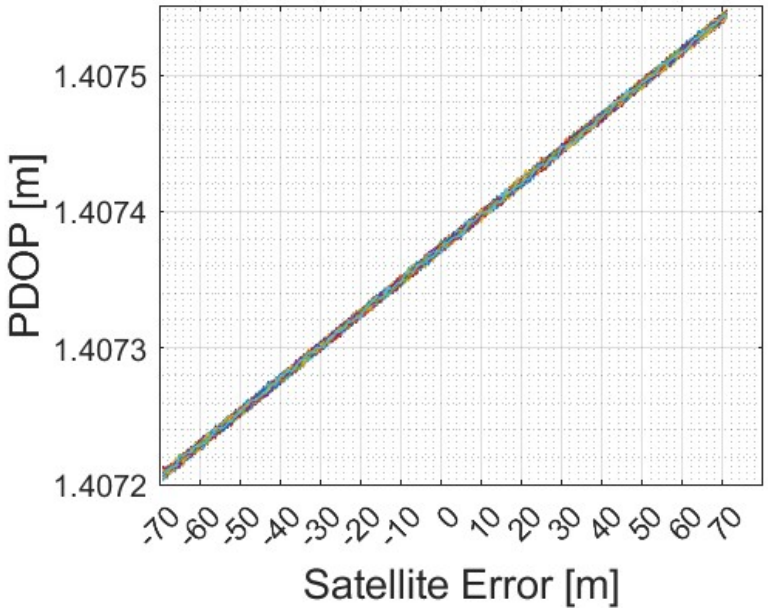

Figure 9.3: PDOP Error [m]

Total variance in the solution error is σ_{meas}PDOP where σ_{meas} is the measured variance. Therefore the solution variance can remain the same as the PDOP increases as long as the σ_{meas} decreases. This can be seen in Figures 9.4 - 9.6. The ideal satellite geometry for the best position results is one satellite directly overhead with three satellites on the horizon. While 70 meters will give a worse satellite geometry, the satellites are now more directly overhead leading to a better positioning solution.

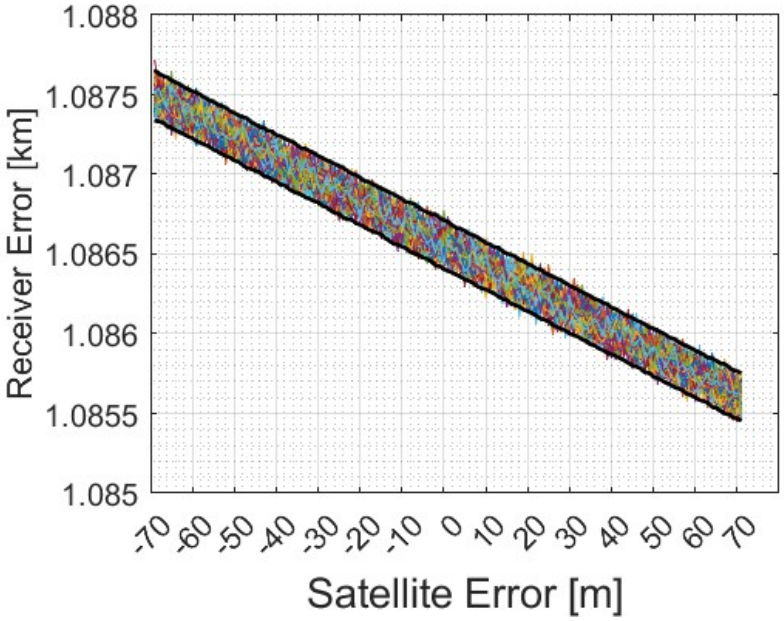

Figure 9.4: X ECEF Error [m]

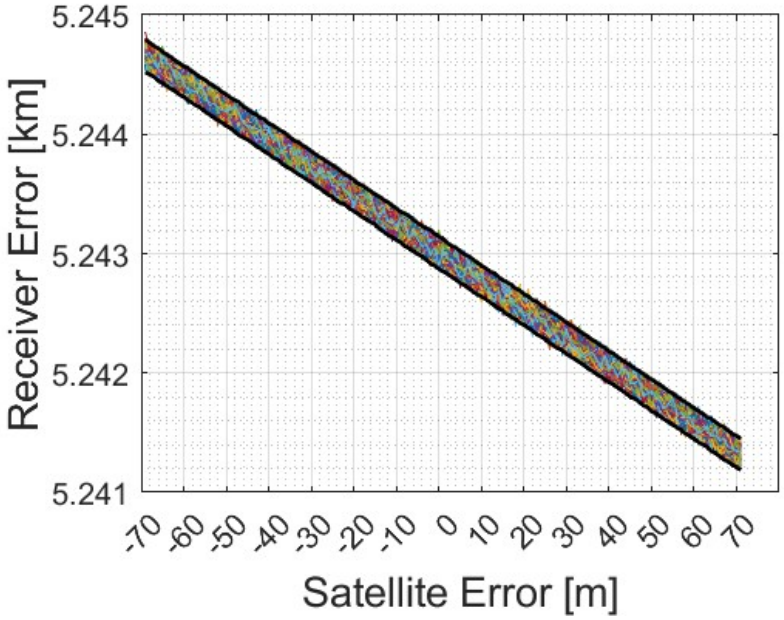

Figure 9.5: Y ECEF Error [m]

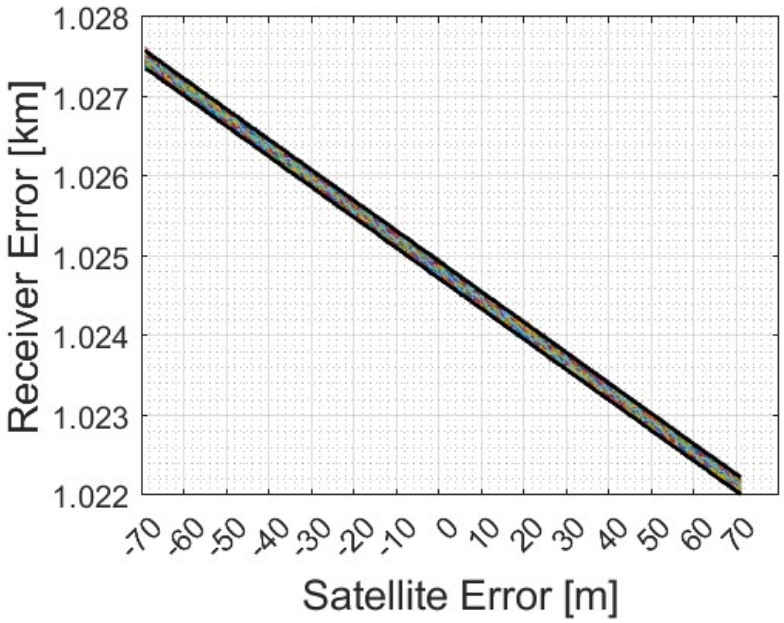

Figure 9.6: Z ECEF Error [m]

The values given in Figures 9.4 - 9.6 are in ECEF which is hard to conceptionalize. The ECEF values were therefore converted into LLA coordinates and compared to the true receiver position to see how much the error effects the solution. Figure 9.7 shows the satellite geoplot of each of the Monte Carlo means for each satellite error. The change between each satellite is so miniscule that it is not visible on the map and therefore only displays as one point. The difference between these two points is a latitude error of 0.1016 degrees and a longitude error of -0.3272 degrees. This corresponds to 11.2776 kilometers of displacement in the latitude direction and 36.3192 kilometers of displacement in the longitude direction. Between each satellite position error there was displacement of 30 meters of latitude and 14 meters of longitude.

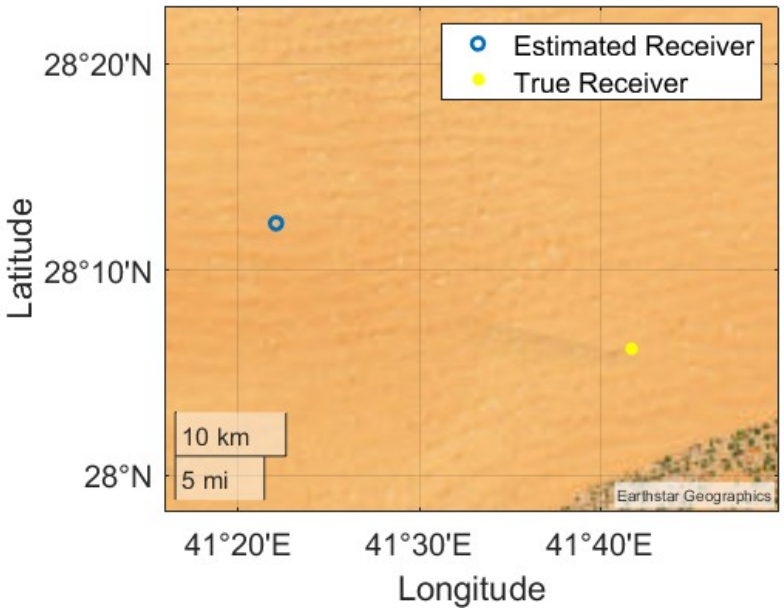

Figure 9.7: Satellite Plot of Receiver Error

Two major conclusions can be drawn from this. One, the satellite's at this altitude must have very precise measurements to be used for estimation as even smaller error during estimation can cause a large displacement to occur. Two, there was meter level displacement between the satellite position error leading to the conclusion that the error in the satellite position did not affect the positioning solution that much. Therefore, adding under 100 meters of error, whether through the ballistic coefficent or atmospheric drag, will cause only meter level displacement from the receiver depending on how well the estimation is performed.

Chapter 10

Conclusions and Future Work

10.1 Conclusions

With the increase of LEO satellites over the decade, the need for precise orbit determination is crucial. One large error of orbit determination at LEO altitude is atmospheric drag. Gravity models, while continuously improving, are fairly accurate at this time for most cases. Drag is difficult to model because of the effect of deterministic quantities that have not been modeled explicitly. One of these terms is the ballistic coefficient. Due to the variables that make up the ballistic coefficient, many may not be known by third-party operators or can change over the lifetime of the orbit. This makes it a vital component in drag estimation. While previous work has been done on estimating the ballistic coefficient, these have all involved estimating the ballistic coefficient from TLE data which already includes a drag term. Estimating the ballistic coefficient from on-board GPS receiver has not been studied at the time of the publication of this thesis to the knowledge of this author.

In conclusion, the satellite orbiting at this altitude is only in view for around 10 minutes at an optimal mask angle. If the on-board GPS receiver fails during this time, the satellite would be able to propagate its position and transmit it to a ground receiver with less than 70 meters of error after determining its orbit for 10 minutes. If the GPS receiver loses connection while not in view, the satellite would be able to propagate with less than 5000 meters of error over 300 minutes.

During the orbit determination process, the theory is that the satellite would be able to calculate its ballistic coefficient to then use during the orbit propagation segment allowing

for a more accurate drag estimation. The estimation accuracy was found to be dependent on the amount of noise in the GPS measurements, something that is not seen in TLE data as the received drag term is a singular value and not changed over time. Estimating the ballistic coefficient over time using truth data resulted in an accuracy of 10% of the true ballistic coefficient, but with noise the error in the ballistic coefficient was above 100% and therefore not useful at all.

Overall, adding error to the ballistic coefficient did not increase the effectivity of the propagation model. This is due to the insignificant amount that the ballistic coefficient effects the atmospheric drag. The drag in turn is much smaller than the gravitational acceleration and therefore a large error needs to be applied to it before any effect is seen. Therefore, in conclusion, the ballistic coefficient is important to model correctly, but a significant amount of error can be applied to it before becoming ineffective to model at all.

Until measurements drop below a standard deviation of 5e-4, the ballistic coefficient will stay below the noise floor. If this happens, the ballistic coefficient will not be able to be estimated. This requirement for measurements would require receivers to be very precise potentially costing a large amount of money or engineering time and would be out of reach for most situations.

Depending on the accuracy need of the estimation, it is feasible for the satellite position to be estimated within 70 meters of error and still maintain accuracy under 30 meters depending on the estimation algorithm. This shows that the error from wrongly estimating the ballistic coefficient would not affect the final position results.

10.2 Future Work

Future work includes seeing the effect of the ballistic coefficient over several days. This would allow a larger view of how the atmospheric drag effects the LEO's orbit. Using the above method over several days would possibly allow for a more accurate estimation of the ballistic coefficient. Possibly adding a different measurement device to more accurate estimate the satellite's total acceleration could be used to estimate the atmospheric drag better leading to a better ballistic coefficient estimation result. It can also be studied how

the atmospheric density estimation effects the ballistic coefficient estimation as well over time.

One of the issues with inaccurately predicting the ballistic coefficient is when estimating the total acceleration of the satellite. With the GPS receiver used for this research only position and velocity measurements were available for use of estimation. To improve the acceleration, it would be ideal to have an IMU on-board the satellite. In theory, this would improve the estimation of the ballistic coefficient, and it would be possible to estimate it within a shorter time frame.

Bibliography

[1] K. Dredge and I. Timmins, "LEO constellations and tracking challenges," en, *Satellite Evolution EMEA*, p. 4, Sep. 2017.

[2] J. P. Thayer, W. K. Tobiska, M. D. Pilinski, and E. K. Sutton, "Remaining Issues in Upper Atmosphere Satellite Drag," en, in *Space Weather Effects and Applications*, American Geophysical Union (AGU), 2021, pp. 111–140, ISBN: 978-1-119-81557-0. DOI: 10.1002/9781119815570.ch5. [Online]. Available: https://onlinelibrary.wiley.com/doi/abs/10.1002/9781119815570.ch5 (visited on 10/07/2022).

[3] T. R. Mortlock and Z. M. Kassas, "Performance Analysis of Simultaneous Tracking and Navigation with LEO Satellites," en, Oct. 2020, pp. 2416–2429. DOI: 10.33012/2020.17658. [Online]. Available: https://www.ion.org/publications/abstract.cfm?articleID=17658 (visited on 12/07/2022).

[4] Z. M. Kassas, "Navigation from Low Earth Orbit: Part 2: Models, Implementation, and Performance," en, in *Position, Navigation, and Timing Technologies in the 21st Century*, Y. T. J. Morton, F. Diggelen, J. J. Spilker, B. W. Parkinson, S. Lo, and G. Gao, Eds., 1st ed., Wiley, Dec. 2020, pp. 1381–1412, ISBN: 978-1-119-45849-4 978-1-119-45855-5. DOI: 10.1002/9781119458555.ch43b. [Online]. Available: https://onlinelibrary.wiley.com/doi/10.1002/9781119458555.ch43b (visited on 01/02/2023).

[5] J. Walsh, L. Berthoud, and C. Allen, "Drag reduction through shape optimisation for satellites in Very Low Earth Orbit," en, *Acta Astronautica*, vol. 179, pp. 105–121,

Feb. 2021, ISSN: 00945765. DOI: 10.1016/j.actaastro.2020.09.018. [Online]. Available: https://linkinghub.elsevier.com/retrieve/pii/S0094576520305579 (visited on 10/13/2022).

[6] J. J. Morales, J. Khalife, U. S. Cruz, and Z. M. Kassas, "Orbit Modeling for Simultaneous Tracking and Navigation using LEO Satellite Signals," en, Miami, Florida, Oct. 2019, pp. 2090–2099. DOI: 10.33012/2019.17029. [Online]. Available: https://www.ion.org/publications/abstract.cfm?articleID=17029 (visited on 08/30/2022).

[7] A. Hauschild and O. Montenbruck, "Precise real-time navigation of LEO satellites using GNSS broadcast ephemerides," en, *NAVIGATION*, vol. 68, no. 2, pp. 419–432, 2021, ISSN: 2161-4296. DOI: 10.1002/navi.416. [Online]. Available: https://onlinelibrary.wiley.com/doi/abs/10.1002/navi.416 (visited on 10/11/2022).

[8] E. B. P. Iv, "Stochastic Satellite Air Drag with the Ballistic Coefficient as a Random Variable," en, Ph.D. dissertation, Air Force Institute of Technology, Wright-Patterson Air Force Base, Aug. 2021.

[9] A. Jennings, R. Anderson, and R. Wells, "SIGNALS OF OPPORTUNITY FOR POSITIONING DETERMINATION,"

[10] J. T. Emmert, H. P. Warren, A. M. Segerman, J. M. Byers, and J. M. Picone, "Propagation of atmospheric density errors to satellite orbits," en, *Advances in Space Research*, vol. 59, no. 1, pp. 147–165, Jan. 2017, ISSN: 0273-1177. DOI: 10.1016/j.asr.2016.07.036. [Online]. Available: https://www.sciencedirect.com/science/article/pii/S0273117716304355 (visited on 01/30/2023).

[11] O. Montenbruck and E. Gill, "REAL-TIME ESTIMATION OF SGP4 ORBITAL ELEMENTS FROM GPS NAVIGATION DATA," en, p. 10, 2000.

[12] O. Montenbruck and P. Ramos-Bosch, "Precision real-time navigation of LEO satellites using global positioning system measurements," *GPS Solutions*, vol. 12, no. 3, pp. 187–198, Jul. 1, 2008, ISSN: 1521-1886. DOI: 10.1007/s10291-007-

0080-x. [Online]. Available: https://doi.org/10.1007/s10291-007-0080-x (visited on 04/27/2023).

[13] C. D. Bussy-Virat, A. J. Ridley, and J. W. Getchius, "Effects of Uncertainties in the Atmospheric Density on the Probability of Collision Between Space Objects," en, *Space Weather*, vol. 16, no. 5, pp. 519–537, 2018, ISSN: 1542-7390. DOI: 10.1029/2017SW001705. [Online]. Available: https://onlinelibrary.wiley.com/doi/abs/10.1029/2017SW001705 (visited on 01/30/2023).

[14] M. Wilkins and K. Alfriend, "Characterizing orbit uncertainty due to atmospheric uncertainty," en, in *Astrodynamics Specialist Conference*, Denver,CO,U.S.A.: American Institute of Aeronautics and Astronautics, Aug. 2000. DOI: 10.2514/6.2000-3931. [Online]. Available: https://arc.aiaa.org/doi/10.2514/6.2000-3931 (visited on 01/30/2023).

[15] T. Yi, Y. Yan, S. Wen, and Y. Zhou, "Analytical Solution of a Super Low Satellite Orbit Disturbed by Atmospheric Drag Considering J2 Perturbation," in *2013 5th International Conference on Intelligent Human-Machine Systems and Cybernetics*, vol. 2, Aug. 2013, pp. 320–325. DOI: 10.1109/IHMSC.2013.224.

[16] J. O. Murcia Piñeros, W. A. dos Santos, and A. F.B.A. Prado, "Analysis of the orbit lifetime of CubeSats in low Earth orbits including periodic variation in drag due to attitude motion," en, *Advances in Space Research*, vol. 67, no. 2, pp. 902–918, Jan. 2021, ISSN: 02731177. DOI: 10.1016/j.asr.2020.10.024. [Online]. Available: https://linkinghub.elsevier.com/retrieve/pii/S0273117720307523 (visited on 10/05/2022).

[17] A. Rich, K. Stuart, and W. Wiesel, "Stochastic Dynamics of and Collision Prediction for Low Altitude Earth Satellites," en, *Journal of the Astronautical Sciences*, pp. 307–320, 2018. DOI: 10.1007/s40295-018-0129-9.

[18] D. A. Vallado and D. Finkleman, "A critical assessment of satellite drag and atmospheric density modeling," en, *Acta Astronautica*, vol. 95, pp. 141–165, Feb. 2014, ISSN: 00945765. DOI: 10.1016/j.actaastro.2013.10.005. [Online].

Available: https://linkinghub.elsevier.com/retrieve/pii/S0094576513003755 (visited on 10/07/2022).

[19] F. A. Marcos, M. J. Rendra, J. M. Griffin, J. N. Bass, D. R. Larson, and J. J. Liu, "Precision Low Earth Orbit Determination Using Atmospheric Density Calibration," en, *The Journal of the Astronautical Sciences*, vol. 46, no. 4, pp. 395–409, Dec. 1998, ISSN: 0021-9142, 2195-0571. DOI: 10.1007/BF03546389. [Online]. Available: https://link.springer.com/10.1007/BF03546389 (visited on 01/02/2023).

[20] B. Bowman, "True satellite ballistic coefficient determination for HASDM," in *AIAA/AAS Astrodynamics Specialist Conference and Exhibit*, Monterey, California: American Institute of Aeronautics and Astronautics, Aug. 5, 2002, ISBN: 978-1-62410-124-3. DOI: 10.2514/6.2002-4887. [Online]. Available: https://arc.aiaa.org/doi/10.2514/6.2002-4887 (visited on 03/03/2023).

[21] J. Haidar-Ahmad, N. Khairallah, and Z. M. Kassas, "A Hybrid Analytical-Machine Learning Approach for LEO Satellite Orbit Prediction," en, in *2022 25th International Conference on Information Fusion (FUSION)*, Linköping, Sweden: IEEE, Jul. 2022, pp. 1–7, ISBN: 978-1-73774-972-1. DOI: 10.23919/FUSION49751.2022.9841298. [Online]. Available: https://ieeexplore.ieee.org/document/9841298/ (visited on 12/07/2022).

[22] J. Yang, C. Han, P. Li, and K. Ding, "Reliability analysis of sgp4 using goce satellite," in *AIAA/AAS Astrodynamics Specialist Conference*, San Diego, CA, Aug. 2014. DOI: 10.2514/6.2014-4281. eprint: https://arc.aiaa.org/doi/pdf/10.2514/6.2014-4281. [Online]. Available: https://arc.aiaa.org/doi/abs/10.2514/6.2014-4281.

[23] P. Kovář, P. Puričer, and K. Kovářová, "Study of the Two-Line Element Accuracy by 1U CubeSat with a GPS Receiver," en, *Sensors*, vol. 22, no. 8, p. 2902, Jan. 2022, ISSN: 1424-8220. DOI: 10.3390/s22082902. [Online]. Available: https://www.mdpi.com/1424-8220/22/8/2902 (visited on 10/07/2022).

[24] K. Riesing, "Orbit Determination from Two Line Element Sets of ISS-Deployed CubeSats," en, p. 9,

[25] J. Vetter, "Fifty Years of Orbit Determination: Development of Modern Astrodynamics Methods," *Johns Hopkins APL Technical Digest*, vol. 27, no. 3, pp. 239–252, Nov. 2007.

[26] SAIC, *Help documentation*. [Online]. Available: https://www.space-track.org/documentation.

[27] *Norad GP Element Sets*. [Online]. Available: https://celestrak.org/NORAD/elements/.

[28] A. Saunders, G. G. Swinerd, and H. G. Lewis, "Deriving Accurate Satellite Ballistic Coefficients from Two-Line Element Data," en, *Journal of Spacecraft and Rockets*, vol. 49, no. 1, pp. 175–184, Jan. 2012, ISSN: 0022-4650, 1533-6794. DOI: 10.2514/1.A32023. [Online]. Available: https://arc.aiaa.org/doi/10.2514/1.A32023 (visited on 08/30/2022).

[29] K. Puttasuwan, P. Saingyen, S. Channumsin, S. Sreesawet, S. Jaturat, and T. Limna, "Investigations of the Ballistic Coefficient Estimation Methods to Improve Accuracy of Reentry Analysis," in *2022 International Electrical Engineering Congress (iEECON)*, Mar. 2022, pp. 1–4. DOI: 10.1109/iEECON53204.2022.9741585.

[30] Z. Lu and W. Hu, "Estimation of ballistic coefficients of space debris using the ratios between different objects," en, *Chinese Journal of Aeronautics*, vol. 30, no. 3, pp. 1204–1216, Jun. 2017, ISSN: 1000-9361. DOI: 10.1016/j.cja.2017.03.009. [Online]. Available: https://www.sciencedirect.com/science/article/pii/S100093611730081X (visited on 08/30/2022).

[31] J. Sang, J. C. Bennett, and C. H. Smith, "Estimation of ballistic coefficients of low altitude debris objects from historical two line elements," en, *Advances in Space Research*, vol. 52, no. 1, pp. 117–124, Jul. 2013, ISSN: 02731177. DOI: 10.1016/j.asr.2013.03.010. [Online]. Available: https://linkinghub.elsevier.com/retrieve/pii/S0273117713001464 (visited on 08/30/2022).

[32] S. Bisnath and R. Langley, "Assessment of the gps/met turbostar gps receiver for orbit determination of a future csa micro/small-satellite mission," *Final report by the Department of Geodesy and Geomatics Engineering, University of New Brunswick, Fredericton, NB for the Directorate of Space Mechanics, Space Technology Branch of the Canadian Space Agency, St-Hubert, Qué., Canada under Public Works and Government Services Canada Contract*, no. 9F011-5, p. 0651, 1996.

[33] E. Jochim, E. Gill, O. Montenbruck, and M. Kirschner, "Gps based onboard and onground orbit operations for small satellites," *Acta Astronautica*, vol. 39, no. 9, pp. 917–922, 1996, ISSN: 0094-5765. DOI: https://doi.org/10.1016/S0094-5765(97)00077-5. [Online]. Available: https://www.sciencedirect.com/science/article/pii/S0094576597000775.

[34] J. W. Gangestad, B. S. Hardy, and D. A. Hinkley, "Operations, Orbit Determination, and Formation Control of the AeroCube-4 CubeSats," en, p. 8,

[35] S. Biswas, L. Qiao, and A. Dempster, "Space-borne GNSS Based Orbit Determination using a SPIRENT GNSS Simulator," Jan. 2015.

[36] C. Xiong, C. Stolle, and H. Lühr, "The Swarm satellite loss of GPS signal and its relation to ionospheric plasma irregularities," en, *Space Weather*, vol. 14, no. 8, pp. 563–577, 2016, ISSN: 1542-7390. DOI: 10.1002/2016SW001439. [Online]. Available: https://onlinelibrary.wiley.com/doi/abs/10.1002/2016SW001439 (visited on 10/06/2022).

[37] S. Biswas, L. Qiao, and A. Dempster, "Space-borne GNSS Based Orbit Determination using a SPIRENT GNSS Simulator," en,

[38] A. Hauschild, M. Markgraf, and O. Montenbruck, "GPS Receiver Performance On Board a LEO Satellite," en, p. 10, 2014.

[39] E.-J. Choi, J.-C. Yoon, B.-S. Lee, S.-Y. Park, and K.-H. Choi, "Onboard orbit determination using GPS observations based on the unscented Kalman filter," en, *Advances in Space Research*, vol. 46, no. 11, pp. 1440–1450, Dec. 2010, ISSN: 02731177. DOI: 10.1016/j.asr.2010.07.022. [Online]. Available: https://

linkinghub.elsevier.com/retrieve/pii/S0273117710005053 (visited on 04/20/2023).

[40] C. Mellow, *The rise and fall and rise of iridium*, en, Aug. 2004. [Online]. Available: https://www.smithsonianmag.com/air-space-magazine/the-rise-and-fall-and-rise-of-iridium-5615034/.

[41] [Online]. Available: https://iridiumwhere.com/about/.

[42] D. A. Vallado, *Fundamentals Of Astrodynamics And Applications*, eng, fourth. Microcosm Press, 2013. [Online]. Available: http://archive.org/details/FundamentalsOfAstrodynamicsAndApplications (visited on 11/22/2022).

[43] J. Wright and J. Woodburn, "Simultaneous real-time estimation of atmospheric density and ballistic coefficient," en, *Advance in the Astronautical Sciences*, vol. 119, pp. 1155–1183, 2005.

[44] G. Beutler, T. Schildknecht, U. Hugentobler, and W. Gurtner, "Orbit determination in satellite geodesy," en, *Advances in Space Research*, vol. 31, no. 8, pp. 1853–1868, Apr. 2003, ISSN: 02731177. DOI: 10.1016/S0273-1177(03)00171-6. [Online]. Available: https://linkinghub.elsevier.com/retrieve/pii/S0273117703001716 (visited on 04/20/2023).

[45] J. R. Vetter, "Fifty Years of Orbit Determination: Development of Modern Astrodynamics Methods," en, *Johns Hopkins APL Technical Digest*, vol. 27, no. 3, 2007.

[46] R. Guo, X. Hu, B. Tang, *et al.*, "Precise orbit determination for geostationary satellites with multiple tracking techniques," *Chinese Science Bulletin*, vol. 55, pp. 687–692, Mar. 2010. DOI: 10.1007/s11434-010-0074-x.

[47] Z. Kang, B. Tapley, S. Bettadpur, J. Ries, P. Nagel, and R. Pastor, "Precise orbit determination for the grace mission using only gps data," en, *Journal of geodesy*, vol. 80, no. 6, pp. 322–331, 2006, ISSN: 0949-7714. DOI: 10.1007/s00190-006-0073-5. [Online]. Available: http://dx.doi.org/10.1007/s00190-006-0073-5.

[48] M. Halsall and P. L. Palmer, "Modelling natural formations of LEO satellites," en, *Celestial Mechanics and Dynamical Astronomy*, vol. 99, no. 2, pp. 105–127, Oct. 2007, ISSN: 1572-9478. DOI: 10.1007/s10569-007-9084-7. [Online]. Available: https://doi.org/10.1007/s10569-007-9084-7 (visited on 08/30/2022).

[49] D. Hobbs and P. Bohm, "Precise orbit determination for low earth orbit satellites," *Annals of the Marie Curie Fellowship Association*, vol. 4, pp. 1–7, 2006. [Online]. Available: https://lucris.lub.lu.se/ws/files/5639688/748400.pdf.

[50] P. Singla, M. Jah, and K. Vishwajeet, "Nonlinear Uncertainty Propagation for Perturbed Two-Body Orbits," en, *Journal of Guidance, Control, and Dynamics*, vol. 37, no. 5, pp. 1415–1425, Sep. 2014, ISSN: 0731-5090, 1533-3884. DOI: 10.2514/1.G000472. [Online]. Available: https://arc.aiaa.org/doi/10.2514/1.G000472 (visited on 05/12/2022).

[51] S. Caldwell, *13.0 Deorbit Systems*, und, Text, Oct. 2021. [Online]. Available: http://www.nasa.gov/smallsat-institute/sst-soa/deorbit-systems (visited on 10/11/2022).

[52] S. Zhou, X. Hu, and B. Wu, "Orbit determination and prediction accuracy analysis for a regional tracking network," en, *Science China Physics, Mechanics and Astronomy*, vol. 53, no. 6, pp. 1130–1138, 2010, ISSN: 1674-7348. DOI: 10.1007/s11433-010-4020-3. [Online]. Available: http://dx.doi.org/10.1007/s11433-010-4020-3.

[53] A. Becker, *Summary*. [Online]. Available: https://www.kalmanfilter.net/.

[54] M. Wang, T. Shan, M. Li, L. Liu, and R. Tao, "GNSS-based orbit determination method and flight performance for geostationary satellites," en, *Journal of Geodesy*, vol. 95, no. 8, p. 89, Jul. 2021, ISSN: 1432-1394. DOI: 10.1007/s00190-021-

01545-1. [Online]. Available: https://doi.org/10.1007/s00190-021-01545-1 (visited on 04/14/2023).

[55] Y. Huang, X. Hu, X. Zhang, *et al.*, "Improvement of orbit determination for geostationary satellites with vlbi tracking," *Kexue tongbao [Chinese science bulletin]*, vol. 56, no. 26, pp. 2765–2772, 2011, ISSN: 1001-6538. DOI: 10.1007/s11434-011-4647-0. [Online]. Available: http://dx.doi.org/10.1007/s11434-011-4647-0.

[56] J. F. M. Lorga, P. F. Silva, F. Dovis, *et al.*, "Autonomous orbit determination for future geo and heo missions," in *2010 5th ESA Workshop on Satellite Navigation Technologies and European Workshop on GNSS Signals and Signal Processing (NAVITEC)*, IEEE, 2010, pp. 1–14, ISBN: 9781424487400.

[57] J. D. Kronman, "Experience using gps for orbit determination of a geosynchronous satellite," in *ION GNSS+*, Sep. 2000.

[58] J. F. M. Lorga, P. F. Silva, F. Dovis, *et al.*, "Autonomous orbit determination for future geo and heo missions," in *2010 5th ESA Workshop on Satellite Navigation Technologies and European Workshop on GNSS Signals and Signal Processing (NAVITEC)*, 2010, pp. 1–14. DOI: 10.1109/NAVITEC.2010.5708028.

[59] W. E. Wiesel, "A Theory of Low Eccentricity Earth Satellite Motion," en, *The Journal of the Astronautical Sciences*, vol. 59, no. 4, pp. 629–649, Dec. 2012, ISSN: 2195-0571. DOI: 10.1007/s40295-014-0007-z. [Online]. Available: https://doi.org/10.1007/s40295-014-0007-z (visited on 01/30/2023).

[60] B. N. S. System. "Beidou navigation satellite system: System." (), [Online]. Available: http://en.beidou.gov.cn/SYSTEMS/System/.

[61] [Online]. Available: https://cddis.nasa.gov/Techniques/GNSS/IGS_Summary.html.

[62] Q. Zhao, J. Guo, C. Wang, *et al.*, "Precise orbit determination for BDS satellites," en, *Satellite Navigation*, vol. 3, no. 1, p. 2, Feb. 2022, ISSN: 2662-1363. DOI: 10.

1186/s43020-021-00062-y. [Online]. Available: https://doi.org/10.1186/s43020-021-00062-y (visited on 04/13/2023).

[63] N. Khairallah and Z. M. Kassas, "Ephemeris Closed-Loop Tracking of LEO Satellites with Pseudorange and Doppler Measurements," en, St. Louis, Missouri, Oct. 2021, pp. 2544–2555. DOI: 10.33012/2021.18114. [Online]. Available: https://www.ion.org/publications/abstract.cfm?articleID=18114 (visited on 04/20/2023).

[64] D. Vallado and P. Cefola, "Two-line element sets - Practice and use," *Proceedings of the International Astronautical Congress, IAC*, vol. 7, pp. 5812–5825, Jan. 2012.

[65] H. Bock, A. Jäggi, R. Dach, S. Schaer, and G. Beutler, "GPS single-frequency orbit determination for low Earth orbiting satellites," *Advances in Space Research*, vol. 43, no. 5, pp. 783–791, 2009, ISSN: 0273-1177. DOI: https://doi.org/10.1016/j.asr.2008.12.003. [Online]. Available: https://www.sciencedirect.com/science/article/pii/S0273117708006340.

[66] P. Dong-Ju and W. Bin, "Kinematic Precise Orbit Determination for LEO Satellites Using Space-borne Dual-frequency GPS Measurements," en, *Chinese Astronomy and Astrophysics*, vol. 36, no. 3, pp. 291–306, Jul. 2012, ISSN: 0275-1062. DOI: 10.1016/j.chinastron.2012.07.006. [Online]. Available: http://www.sciencedirect.com/science/article/pii/S0275106212000549 (visited on 04/20/2023).

[67] D. Kuang, S. Desai, A. Sibthorpe, and X. Pi, "Measuring atmospheric density using GPS–LEO tracking data," en, *Advances in Space Research*, vol. 53, no. 2, pp. 243–256, Jan. 2014, ISSN: 02731177. DOI: 10.1016/j.asr.2013.11.022. [Online]. Available: https://linkinghub.elsevier.com/retrieve/pii/S0273117713007060 (visited on 04/20/2023).

[68] T. Van Helleputte and P. Visser, "GPS based orbit determination using accelerometer data," en, *Aerospace Science and Technology*, vol. 12, no. 6, pp. 478–484, Sep. 2008, ISSN: 12709638. DOI: 10.1016/j.ast.2007.11.002. [Online].

Available: https://linkinghub.elsevier.com/retrieve/pii/S1270963807001423 (visited on 04/20/2023).

[69] D. Koks, "Using Rotations to Build Aerospace Coordinate," en, p. 42,

[70] M. W. Holmes, "School of Aerospace, Mechanical and Mechatronic Engineering," en, *Reference frames*,

[71] *Spherical Harmonic Representation of the Gravity Field Potential*, English. [Online]. Available: https://spsweb.fltops.jpl.nasa.gov/portaldataops/mpg/MPG_Docs/Source%20Docs/gravity-SphericalHarmonics.pdf (visited on 11/15/2022).

[72] Y. Zhuang and L. Wang, "ANALYSIS OF THE GRAVITY MODELS IMPACT ON LEO SATELLITE ORBIT PREDICTION," en, *The International Archives of the Photogrammetry, Remote Sensing and Spatial Information Sciences*, vol. XLVI-3/W1-2022, pp. 307–313, Apr. 2022, ISSN: 2194-9034. DOI: 10.5194/isprs-archives-XLVI-3-W1-2022-307-2022. [Online]. Available: https://www.int-arch-photogramm-remote-sens-spatial-inf-sci.net/XLVI-3-W1-2022/307/2022/ (visited on 10/19/2022).

[73] M. A. Wieczorek and M. Meschede, "SHTools: Tools for Working with Spherical Harmonics," en, *Geochemistry, Geophysics, Geosystems*, vol. 19, no. 8, pp. 2574–2592, 2018, ISSN: 1525-2027. DOI: 10.1029/2018GC007529. [Online]. Available: https://onlinelibrary.wiley.com/doi/abs/10.1029/2018GC007529 (visited on 10/28/2022).

[74] B. D. Tapley, B. E. Schutz, and G. H. Born, "Chapter 2 - The Orbit Problem," en, in *Statistical Orbit Determination*, B. D. Tapley, B. E. Schutz, and G. H. Born, Eds., Burlington: Academic Press, Jan. 2004, pp. 17–91, ISBN: 978-0-12-683630-1. DOI: 10.1016/B978-012683630-1/50021-7. (visited on 11/22/2022).